UNIVERSITY OF CALIFORNIA,
IRVINE

Degradation Mechanisms in Ceramic Abradable Coatings for Hot Section Turbine Components

DISSERTATION

submitted in partial satisfaction of the requirements
for the degree of

DOCTOR OF PHILOSOPHY

in Materials Science and Engineering

by

Kara Jeanne-Phillips Bridges

Dissertation Committee:
Professor Daniel Mumm, Chair
Professor Timothy Rupert
Professor Lorenzo Valdevit

2018

DEDICATION

To

my husband, family, lab mates, and friends

in recognition of the fact that I could not have done this without them!

TABLE OF CONTENTS

LIST OF FIGURES

Page

LIST OF TABLES

LIST OF EQUATIONS

ACKNOWLEDGMENTS

I would like to acknowledge my committee chair, Professor Daniel Mumm, who has supported me and given me ample opportunities to grow and develop my research and presentation skills during my time here at UCI. I would also like to thank my committee members, Professor Timothy Rupert, Professor Lorenzo Valdevit, Professor AJ Shaka, and Professor Carlos Levi, for donating their time and providing me feedback during my degree examinations.

A special thanks to my friends and lab mates Kliah Soto Leytan and Kenta Ohtaki for the countless hours of help and time spent talking through issues. I want to thank my undergraduate student researchers, Andy Lam and Gabriel Pillitiere, and the whole Mumm lab: Madhura Basu Majumder, Amir Saeidi, Maryam Zahiri Azar, Tim Montalbano, Kyle McDevitt, Kunthea Deng, and Joberto Lee. Thanks to Tro Babikian for always having the friendliest face in the hall. Thank you also to the Mecartney lab where my graduate studies began, specifically Jesse Angle and Chris Hoo for all their help at the beginning. And thank the Lord that I was able to finish writing this cause writing is hard and takes a very long time!

I want to acknowledge the assistance from various others at UCI: all the staff at the Irvine Materials Research Institute for characterization help and trainings, the Department of Chemical Engineering and Materials Science staff, ChAMP program, Jason and Jennifer in the Rupert lab for their help with the nanoindenter experiments, and to Alex in the Scheonung lab for his help and guidance with the SPS experiments.

In addition, thank you to Plasma Technology, Incorporated and Solar Turbines, Incorporated for providing abradable coating samples. Thank you to the Southwest Research Institute and the DOE UTSR fellowship program for their support during my internship at Solar Turbines, as well as my mentors for all their help during my internship. Financial support was provided by the University of California, Irvine Dept. of Chemical Engineering and Materials Science, US Dept. of Energy, and US Office of Naval Research.

CURRICULUM VITAE

EDUCATION

University of California, Irvine (UCI) Irvine, CA
Ph.D. Materials Science and Engineering 2018
Thesis: "Degradation Mechanisms in Ceramic Abradable Coatings for Hot Section Turbine Components"
Advisor: Prof. Daniel R. Mumm
M.S. Materials Science and Engineering 2014

Clemson University Clemson, SC
B.S. Materials Science and Engineering 2013

PROFFESIONAL EXPERIENCE

Solar Turbines Incorporated San Diego, CA
Intern/UTSR Fellow, Materials and Processes Group July-Sept. 2016

- Worked as a member of the surface engineering team on coating process and product support with tasks ranging from coating qualifications to design validation using optical and electron microscopy.

Los Alamos National Laboratory Los Alamos, NM
Graduate Research Intern, Fuels Research Lab July-Sept. 2015

- Characterized the thermophysical properties of candidate composite ceramics for advanced nuclear fuels using laser flash analysis, differential scanning calorimetry, and dilatometry.

FELLOWSHIPS & AWARDS

University Turbine Systems Research (UTSR) Gas Turbine Industrial Fellowship 2016
Southern California Society for Microscopy and Microanalysis Image Contest Winner 2015
Nuclear Regulatory Commission Graduate Student Fellowship 2014-15
Graduate Assistantship in Areas of National Need (GAANN) Fellowship 2013-14

PEER REVIEWED PUBLICATIONS

- Travis, A. W.; Bridges, K. J. P.; Nelson, A. T.; and Mecartney, M. L.; *Thermal Conductivity and Kapitza Resistance of an Al_2O_3-$MgAl_2O_4$-8YSZ Ceramic Composite*, J. Am. Cer. Society, *SUBMITTED FOR REVIEW*.
- Eskelsen, J. R.; Phillips, K. J.; Hipps, K. W.; and Mazur, U.; *Hyperbranched Crystalline Nanostructure Produced from Ionic pi-conjugated Molecules*, Chem. Communications, 51 (2015) pp. 2663-6.

OTHER PUBLICATIONS

- Phillips, K. *Ceramics Hold the Key to Future of Nuclear Energy*, Am. Cer. Soc. Bulletin, 94 (2015) pg. 41.

PRESENTATIONS

- *Factors Affecting Ceramic Abradable Coating Damage Accommodation* – poster, Engineering Conferences International Thermal Barrier Coatings V 2018.

- *The Influence of Microstructural Defects on Wear Mechanisms in Zirconia-Based Abradable Coatings* – talk, International Conference and Exposition on Advanced Ceramics and Composites 2018.
- *Correlating Thermal Barrier Coating Microstructure between Engine Run Combustion Hardware and Furnace Cycle Testing* - poster, 2016 University Turbine Systems Research Workshop.
- *Degradation of High Temperature Abradable Coating Systems in High Water Vapor Turbine Environments* – talk, Materials Science and Technology 2016.
- *Low Velocity Burner Rig Study on Hot Corrosion of Turbine Components* – talk, 2016 Indo-US Workshop on Ceramic Coatings and Multilayers.
- *The Effect of Interfaces on Mechanical and Thermal Properties of Fine-Grained Ceramic Composite Nuclear Fuel* – talk, Materials Science and Technology 2015.
- *Multiphase Ceramics for Enhanced Mechanical Properties of Inert Matrix Nuclear Fuel* – poster, Materials Science and Technology 2014.
- *Challenges in the Synthesis of Nanocrystalline, Multiphase Ceramics for Inert Matrix Nuclear Fuel* – poster, 2014 Gordon Research Conference: Solid State Studies in Ceramics.
- *Mechanical Properties of Natural vs. Manmade Fibers* – poster, 2011 International Symposium on New Frontiers in Fiber Materials Science.

LEADERSHIP & PROFESSIONAL INVOLVEMENT

UCI Mumm Laboratory Safety Representative 2015-2018

- Responsible for ensuring up to date standard operating procedures, chemical inventory and waste management, as well as the ongoing training of new students in the lab.

American Ceramic Society (ACerS) 2014-2017

- Appointed representative for ACerS President's Council of Student Advisors (PCSA); contributed as a programming committee member and past outreach committee chair leading a group of 10 students in efforts to promote ceramic engineering to the future generation of engineers.

President and Co-founder of American Nuclear Society (ANS) Student Chapter, UCI 2013-2015

- Worked with five other UCI students to obtain official recognition from ANS for the student section.
- Elected president for 2014-15 academic year; responsible for planning and executing all student chapter activities including seminars from invited speakers as well as industry tours.
- Appointed student co-chair for ANS conference in Nov. 2014; assigned task of organizing and running the conference student program.

TEACHING

X-ray Diffraction, Electron Microscopy, and Microanalysis Lab (CBEMS 164L) Jan.-March 2017

- Led all lab sessions introducing students to the principles of electron microscopy and the different analysis techniques (secondary and backscatter imaging, energy dispersive spectroscopy), and x-ray diffractometry.

Principles of Materials Science and Engineering (ENGR 54) March-June 2015

- Assisted professor in introductory course on materials science and engineering, mainly in grading assignments, teaching weekly discussion sessions, and holding weekly office hours.

Ceramic Materials (CBEMS 158) March-June 2014

- Assisted professor in course through grading assignments and holding weekly office hours.

ABSTRACT OF THE DISSERTATION

Degradation Mechanisms in Ceramic Abradable Coatings for Hot Section Turbine Components

By

Kara Jeanne-Phillips Bridges

Doctor of Philosophy in Materials Science and Engineering

University of California, Irvine, 2018

Professor Daniel R. Mumm, Chair

Hot section abradable coatings play an integral role in reaching optimal efficiency of gas turbine engines by preventing unnecessary gas leakage through clearance control. As turbine material technologies advance, there is a push for the development of abradable coatings that can withstand more severe operating conditions and retain the optimum balance of abradability and durability. However, current understanding of abradable coating properties that promote a controlled removal of these highly brittle materials is missing. In this work, a theoretical analysis is first presented for expected abradable mechanisms detailing key properties and microstructural features that enable each mechanism. Next, experimental studies are completed to evaluate coating evolution in representative turbine operating conditions and to determine key factors affecting abradable behavior. Two current technology abradable coatings processed by air plasma spraying, dysprosia-stabilized zirconia (DySZ) with hexagonal boron nitride (hBN) and yttria-stabilized zirconia (YSZ) with nanozone features, have been studied using scanning electron microscopy, x-ray diffraction, Raman spectroscopy, and optical vibrometry. A challenge in evaluating hot section abradable materials is that of testing in engine relevant conditions but in a significantly scaled-down, more controlled lab test. Appropriate testing

methodologies were first established. Both as-processed and aged coatings were then tested in a representative macroscratch test to investigate the influence of different defects, their evolution with aging, and observed damage behavior. Results for YSZ-based coatings show highly brittle fracture that penetrates deep within the coating and also changes with aging. The DySZ, hBN coating showed a change in phase of the weakening phase, hexagonal BN, after processing and a significant increase in hardness with aging. Yet, these coatings showed the ability to maintain a shallow damage zone even after aging with little damage propagation further into the remaining coating material. This suggests that the presence of a secondary phase plays a significant role in maintaining a more controlled and consistent damage mechanism. The results of this study, in combination with a study of deformation seen in engine hardware, can be used to build further predictive models of abradable damage accommodation behavior.

CHAPTER 1: Introduction

1.1 Motivation

With the push for lower emissions and increased energy demands on natural gas plants, generating 22% of the world's total electricity according to the International Energy Agency's 2018 Key World Energy Statistics report, there is a strong driver to increase the efficiency of gas turbines for both the power generation and aerospace industries[1]. As advanced combustion, aerodynamics, and heat transfer concepts are developed to facilitate enhanced turbine efficiencies, it is imperative to evaluate the performance of current materials systems to be used in conjunction with these concepts.

By optimizing the utilization of the energy produced in turbines through refinement of engineering design of combustion, aerodynamics, and heat transfer, the current materials systems are being pushed beyond their intended use. For example, the implementation of the integrated gasification combined cycle (IGCC) process, which provides efficiency increases over conventional natural gas fired turbines, results in significant changes to the combustion environment to which hot section materials are exposed. Natural gas fired turbines burn 9.5% H_2O vapor in the combustion environment, while the synthetic gas burned in the IGCC process can have up to 30% H_2O vapor present with the addition of advanced NO_x suppression technologies[2]. Increased water vapor environments have been shown to accelerate degradation mechanisms detrimental to these material systems, such as enhanced sintering and phase transformations[3,4].

The aim of this work is to evaluate specifically high temperature, ceramic abradable coatings, and their degradation mechanisms seen in relevant service conditions in order to facilitate the implementation of these advanced coatings for turbine efficiency improvements.

These abradable coating systems will be studied in the as-processed condition as well as in representative combustion environments. Microstructural evolution and thermo-mechanical degradation mechanisms will be evaluated, and experimental findings will be used as the basis for proposed material improvements to optimize these systems.

1.2 Turbine Engine Background

Turbine engines are, at their core, Carnot engines operating through the Brayton cycle[5]. The configuration of a power generation turbine is shown in Figure 1, and an aero engine is shown in Figure 2[6,7]. In both cases, as ambient air enters the turbine, it progresses first through the compressor, or the low temperature, high pressure section, where the air is moved through a series of progressively smaller diameter rotary disks containing vanes and turbine blades designed to direct and catch the moving air. It then enters the combustion chamber, where the compressed air is mixed with fuel and combusted. That energetic reaction then sends the high temperature, high pressure gas through a series of bladed rotary disks that are coupled to a rotary shaft. These disks progressively get larger in diameter and catch the combusted air to drive the rotary shaft, which in turn produces energy by driving a magnetic generator, thus producing energy[5]. A main difference for the aero engine is that part of the air is used to generate thrust. For both to reach optimal Carnot efficiency, the temperature difference between the hot and cold sections of the turbine must be maximized. Thus, increasing the hot section temperature in the combustor is directly related to engine efficiency increases and is a continuing goal of future turbine technology design.

Turbine engines are complex systems that use a wide range of engineering materials to meet the varying requirements of each component in the engine throughout its different sections. For instance, the large fan blades at the front of the turbine experience lower temperature loads

but see high centrifugal forces due to their large size. Thus, strong and lightweight materials, like polymer composites or titanium alloys, are used for these components[8]. Whereas, blades found closest to the combustion chamber, or first stage hot section blades, see extreme temperatures, up to 1400˚C currently, and are much smaller in size to facilitate faster rotational speeds. These first stage blades must be able to withstand high centrifugal forces with turbine disks rotating up to 40,000 rpm while also maintaining high temperature stability[9,10]. There is also added complexity to materials that can be selected for use past the combustor since the combustion gas stream can carry impurities that may degrade certain materials. Thus, hot section turbine materials are typically composites that can combine the advantageous properties of several different materials.

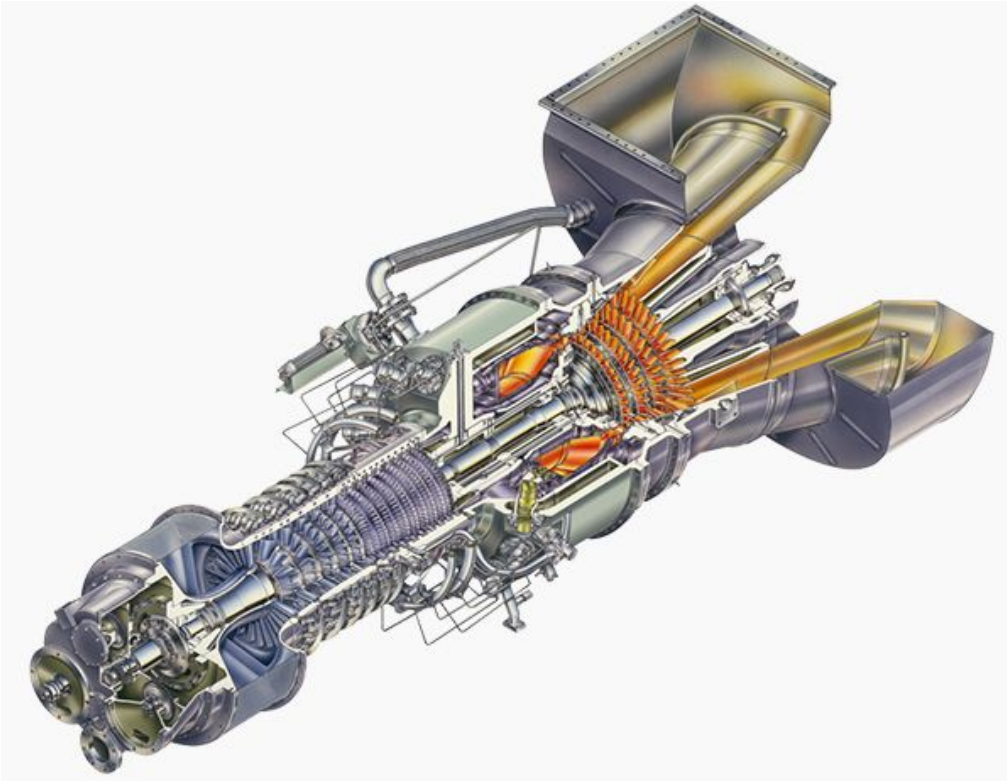

FIGURE 1. Cut out of a Solar Turbines, Inc. (© 2018, San Diego, CA, USA) Titan™ 130 power generation turbine[6].

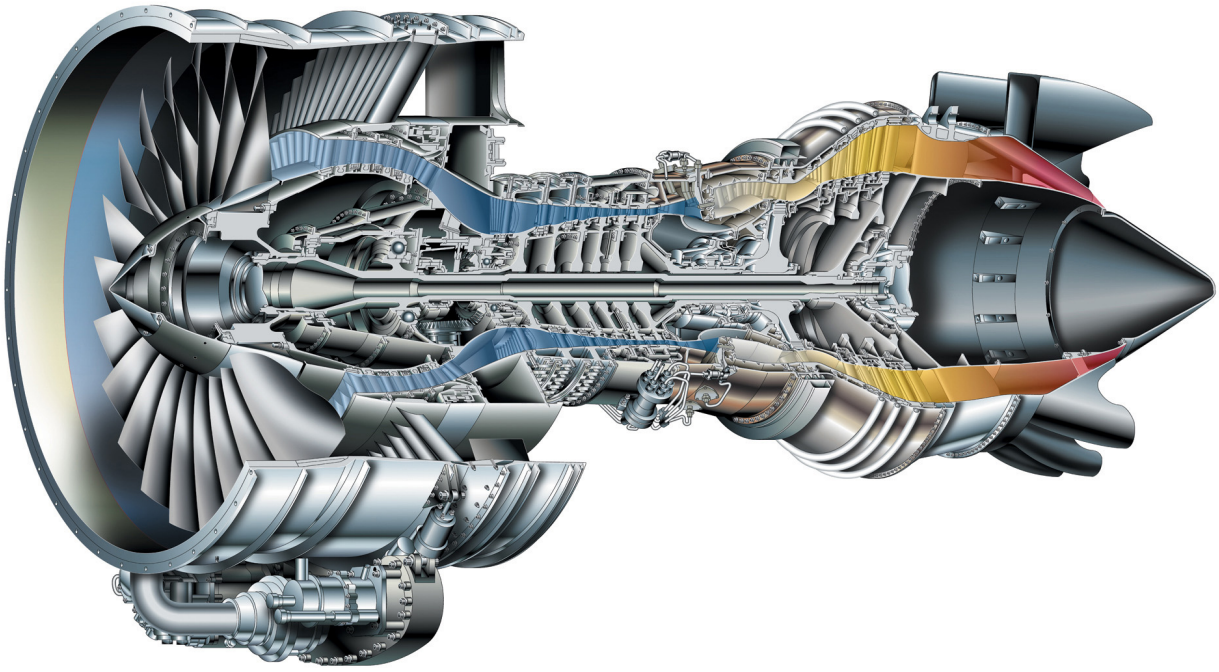

FIGURE 2. Cut out of a PW6000 aero turbine by Pratt and Whitney (Hartford, CT, USA), a division of United Technologies Corporation[7].

Hot section composite materials are often multilayer systems consisting of metallic superalloys for base parts with a metallic bond coat interlayer and a ceramic topcoat. Nickel based superalloys are easily made into complex geometries and provide superior mechanical strength but are subject to degradation at the high temperatures (>1000˚C) seen in turbine hot sections[9]. Therefore, additional coatings are required as barriers from chemical and mechanical attack as well as thermal degradation. These additional coatings are designed specifically for their intended working environment, and since increased efficiency demands higher turbine hot section temperatures, the coatings in the hot section of the turbine are subject to the most extreme and dynamic working environment. Therefore, this study will focus on understanding and improving hot section topcoat materials.

1.3 Design of Hot Section Topcoat Materials

Topcoat material systems are specialized based on their location in the hot section of the turbine, which dictates the requirements for temperature and mechanical tolerance. The proximity of the parts to the combustion chamber, presence of backside substrate cooling, and whether the part is stationary or dynamic dictate property requirements, which are dependent on the process used to make the coatings[5]. Thus, the design of topcoat materials encompasses materials selection as well as microstructure selection.

Over twenty years of hot section topcoat materials research has shown tetragonal yttria stabilized zirconia (YSZ) to be the best candidate coating material for metallic turbine hot section parts due to its rare combination of properties[9,11,12]. YSZ has an inherently low thermal conductivity that varies little with change in temperature, and is also phase stable at the working temperature of up to ~1400˚C. Furthermore, tetragonal prime (t') YSZ, zirconia partially stabilized with 6-8 weight percent yttria, shows an unprecedented ferroelastic toughening mechanism that prevents foreign object damage and spallation of the coating[13–15]. Although studies have been done on different materials that show improved thermal properties or chemical stability with airborne contaminants, they are rarely implemented due to their low toughness compared to YSZ[9,16–18]. Therefore, research efforts have been directed toward YSZ based coatings, or variants thereof.

For microstructure selection, there are two main types of coating processes, electron beam physical vapor deposition (EB-PVD) and air plasma spraying (APS), used, which will dictate coating microstructural features. EB-PVD has the ability to make smooth coatings with tight composition and thickness control, while APS is a significantly cheaper and less time intensive process used to make coatings for larger or stationary parts[9]. The microstructures of

EB-PVD versus APS coatings also vary greatly, as shown in Figure 3, A and B. The EB-PVD process is effective for the growth of columnar grains that afford a low in-plane modulus providing good strain tolerance. The APS process results in coatings with horizontal splats that help further reduce heat transfer to the substrate but have lower strain tolerance than EB-PVD coatings[9]. Coatings processed by APS will be focused on in this study because the intended application takes advantage of the high concentration of horizontally oriented interfaces and larger coating thickness.

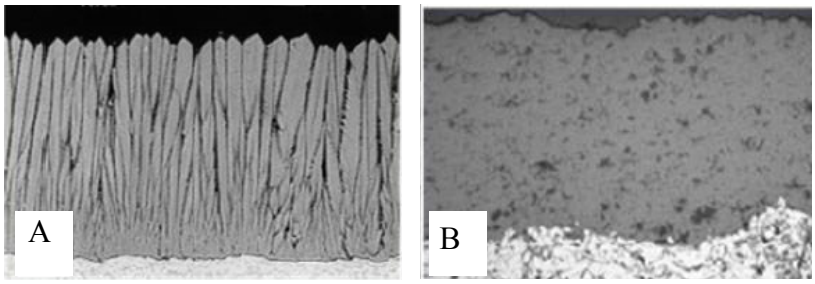

FIGURE 3. Columnar microstructure of EB-PVD YSZ coating (left image, A) versus more horizontally oriented splat microstructure of APS YSZ coating (right image, B)[9].

1.4 The Role of Abradable Coatings in Higher Efficiency Turbines

A specialized protective coating for hot sections of aerospace and power generation turbines is an abradable coating. These advanced topcoat materials are applied to the engine casing (as shown in Figure 4) and are designed to minimize the clearance between the stationary turbine casing and rotating blade tips, which increases compressor efficiency and reduces fuel consumption[19,20]. As the engine is turned on and brought to operating temperature, the turbine blades expand due to thermal expansion, which produces the first passage of the blades through the abradable coating. Without abradable coatings, thermal expansion must be accounted for when determining the tip clearance between the blades and casing to prevent contact that would damage the turbine blades. Rotor displacements due to vibration in the turbine further complicate the retention of proper clearance between the two parts[21]. Additionally, with higher

operating times, creep of the turbine blades results in further rub impact with the coatings. Without the application of abradable coatings, the clearance that must be maintained to prevent blade damage upon rub impact with the casing results in the allowance of a steady stream of gas to be lost to the environment during operation.

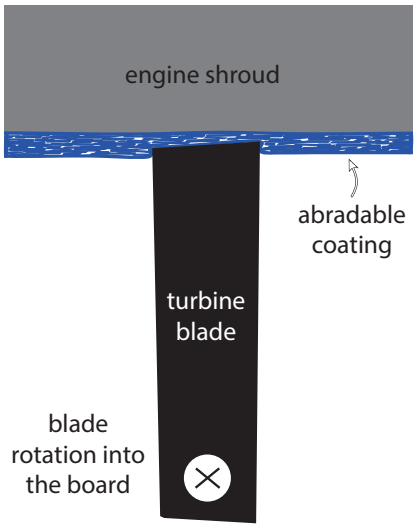

FIGURE 4. Schematic showing the placement of the abradable coating onto the shroud.

Implementing abradable coatings in the hot section (high temperature, high pressure stage of the turbine) has shown an increase in efficiency of that stage alone by 3% with overall engine efficiency improvements greater than 1% reported[20,22]. Abradable coatings maintain tight clearances by acting as sacrificial material that can be easily removed to accommodate the expansion of the blades with thermal expansion and further vibrational offsets of the rotor or blade creep[23]. Hot section abradable coatings must be stable at the intended working temperature, have sufficient hardness and toughness to withstand impact with particulates that may enter the turbine stream, and be easily abraded with a smooth wear track[24]. To ensure temperature stability and sufficient durability, current technology abradable coating materials are

zirconia based. However, zirconia is a naturally brittle material that does not have sufficient abradability, and thus must be modified for use in this application.

1.4.1 Current Hot Section Abradable Coating Designs

Current technology hot section abradable coating designs can be divided into two main categories based on the strategy used for enhancing the abradability of zirconia. Both use air plasma spray processing as the main coating application method and t' zirconia as the matrix phase. The different microstructure design strategies are shown in Figure 5. The first variant (Figure 5A) relies on a large fraction of oxide secondary phase that introduces weak interfaces between the matrix phase and secondary phase[25]. T. Steinke, et al [25] used magnesium aluminum spinel while M. H. Foroushani, et al [26] used lanthanum phosphate as the secondary phase in addition to the zirconia matrix. A second strategy, Figure 5B, relies on the addition of a fugitive polymer pore former for enhanced abradability. For the porous system, abradability can be further enhanced with the addition of small fractions of a solid dislocator phase, typically hexagonal boron nitride (hBN), which acts to reduce interfacial bonding between the APS splat boundaries, shown in Figure 5C[27,28]. Further work has been done on the porous APS system to deposit an additional layer of material using 3D-printing to make a patterned surface that improves aerodynamics[29].

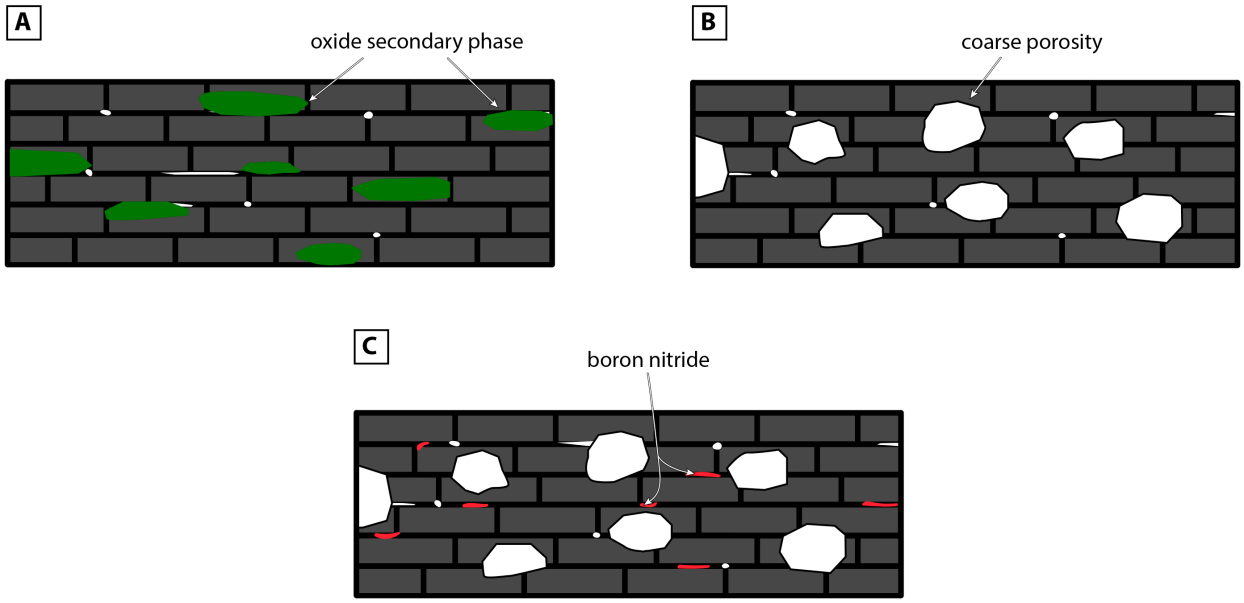

FIGURE 5. Schematic A shows one ceramic abradable coating design that includes a large fraction of secondary phase and little porosity. Schematic B shows a second design strategy that includes 25-40% porosity, and C shows further additions of a small fraction of dislocator phase in addition to the coarse porosity used to increase abradability.

To date, ceramic abradable coatings that do not rely on coarse porosity have required blades that are tipped with an additional abrasive material, typically cubic boron nitride or silicon carbide, in order to prevent excessive blade wear upon contact[24,27,30]. The abrasive particles, however, are expensive to implement and have low oxidation/volatilization resistance, which will only worsen in high water vapor environments[3,24]. Therefore, this work will focus on abradable coating compositions that do not require abrasive blade tipping.

1.4.2 Testing and Performance Evaluation

Testing of abradable coatings in the academic literature has been limited to lower temperature, metal matrix abradable coatings. Authors have used mainly scratch testing or other wear tests, like linear reciprocating wear, to evaluate these metal-based coatings[19,23,31–35]. However, ceramic abradable coatings will undergo very different failure mechanisms than highly plastic metal-based coatings. Thus, successful lab scale testing of ceramic abradable coatings

has not been reported. Testing of ceramic abradable coatings and performance evaluations have been limited to industrial-scale rig testing by coating or engine manufacturers[23,31,36,37]. These high temperature rub rigs simulate the engine operating conditions and operate at temperatures of up to 1200˚C using a combustion flame with rotational rub impact at speeds of up to 30,000-40,000 rpm[22]. These are extremely complex test rigs with high operating costs. In addition, the evaluation of ceramic abradable coatings post rub rig testing has been qualitative in nature with performance metrics reporting on the smoothness of the wear track or amount of blade material transferred to the coating. Thus, a quantitative assessment of high temperature, ceramic abradable coatings has not been reported, and is needed to advance the understanding of how to design and implement the controlled removal of these inherently brittle materials.

1.5 Problem Statement and Objectives

The understanding of design and evaluation in high temperature, ceramic abradable coatings has been limited to few peer reviewed literature articles, industry publications, conference proceedings, or patents due to the proprietary nature of these coatings. Bridging the current gap in knowledge between processing and performance is the aim of this dissertation work. If a link can be established between process dependent coating microstructural features and the mechanism behind damage accommodation that gives rise to desired performance, then future design strategies can be developed for coatings that can withstand higher temperatures and harsher operating conditions in more efficient turbines.

To establish this link, the first research question that will be explored is how current technology high temperature ceramic abradable coatings accommodate damage. Ceramic materials are inherently brittle and thus, fail without warning and in an uncontrolled manner. Since prior work has shown ceramic abradable coatings to sustain rub impacts in a controlled

manner under certain conditions, the question becomes how are these brittle materials accommodating damage? These coatings are either sustaining controlled brittle fracture or have pseudo-plastic deformation mechanisms occurring. Chapter 3 will outline the current design strategies employed, their expected damage mechanism, and the theoretical framework for understanding the mechanics of these abradable systems.

Chapter 4 will focus on establishing a connection between microstructural features and their role in promoting different damage accommodation mechanisms. In Chapter 4, two current technology abradable coating systems will be studied and the evolution of their microstructures in representative service conditions will be presented. Both coating systems in the as-processed, as well as in the exposed state, will be tested for abradability. Strategies for effective lab scale abradability testing and results are presented. The background for experimental methods employed to answer the questions outlined previously is presented in Chapter 2. Chapter 5 will conclude this study and provide future directions for the work.

CHAPTER 2: Experimental Methods

2.1 Processing

2.1.1 Air Plasma Sprayed Abradable Coatings

Air plasma spraying, or APS, is one of the main processes utilized for depositing abradable coatings because it is able to achieve a thick coating with desirable microstructural features for promoting abradability. The coating is applied through the deposition of powder particles through a plasma torch that burns above 3000˚C in the presence of hydrogen, helium, argon, nitrogen, or mixtures of those gases[25,38]. The molten powder particles reach the substrate and cool as individual splats. The coating is built up as the plasma torch and powder particle stream raster across the substrate surface. This process results in coatings with horizontally oriented microstructural features termed APS splats. The morphology and properties of APS coatings can be tuned by adjusting the spray parameters used during the process, such as starting powder morphology, spray distance, plasma power, and others[39]. An illustration of the process is shown below in Figure 6.

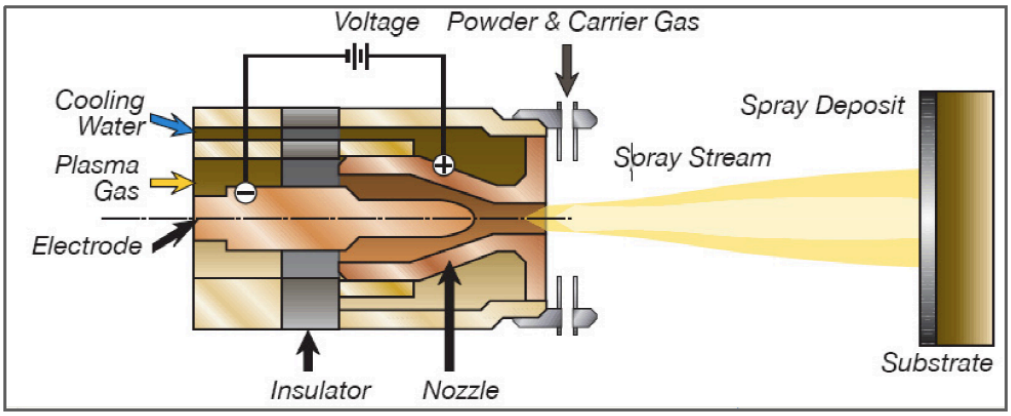

FIGURE 6. Illustration of air plasma spray process and parameters that can be varied, like powder inlet, substrate temperature or morphology, plasma gas, and many others[39].

Two APS ceramic abradable coatings will be studied in this work. The first is a dysprosia stabilized zirconia (DySZ), polymer, hBN system (further referred to as DySZPB),

which has shown improved thermal shock, sintering resistance, and erosion resistance[20,27,40]. The second is a YSZ, polymer abradable system (further referred to as YSZP). DySZPB coatings were processed by Plasma Technology Incorporated (Torrance, CA USA) using Durabrade 2192 spray dried powders purchased from Oerlikon Metco US Inc. (Brea, CA USA). The APS YSZP system was made by Solar Turbines Incorporated (San Diego, CA USA) using Metco 2460NS spray dried powders also purchased from Oerlikon Metco. Powder specifications are listed below in Table I as specified in the 2012 Sulzer Metco Material Product Datasheet. The processing parameters used to deposit the DySZPB and YSZP coatings are proprietary information, and are thus, not known by the authors. Both Plasma Technology Incorporated and Solar Turbines Incorporated used the recommended spray parameters provided by the powder manufacturers, Oerlikon Metco.

TABLE I. Starting material specifications for Durabrade 2192 and Metco 2460NS powders.

Material	**Constituent Weight Percent (wt. %)**					**Powder Morphology; Particle Size**	**Operating Temp.**
Durabrade 2192	ZrO_2 balance	Dy_2O_3 9.5	hBN 0.7	Polyester 4.5	Impurities 0.1	Agglomerated; 176 +/- 11µm	1200˚C
Metco 2460NS	ZrO_2 balance	Y_2O_3 7.5	Binder 4	Polyester 4	Impurities 0.9	Agglomerated, HOSP, blended; 176 +/- 11µm	1200˚C

2.1.2 Bulk Materials

Bulk ceramic samples were processed in order to study the matrix material behavior. Commercial starting powders of 4 mol % YSZ (4YSZ, 99.7% pure, Tosoh TZ-4Y, Tokyo, Japan) and hBN (99.5% pure by metals basis, Alfa Aesar, Massachusetts, USA) were used. Bulk samples were made of 4YSZ, processed two different ways to achieve the tetragonal (t) phase and the metastable tetragonal prime (t') phase, and a 4YSZ - 25 vol % hBN composite.

Processing the t' 4YSZ required special attention because a fast cooling rate from the cubic phase field (shown in phase diagram Figure 7, below) is essential to attaining the metastable t' phase[41–44]. Spark plasma sintering (SPS) was utilized to achieve the necessary high temperatures and cooling rates. 4YSZ powders were first weighed and loaded into a 18 mm diameter graphite die with 2 sheets of graphite foil used to separate the powder from graphite die. A Fuji SPS 825-S (Fuji Electronic Industrial Co. Ltd., Saitama, Japan) was used with parameters of 100˚C/minute heating rate, 65 MPa pressure, 1600˚C sintering temperature, 10 minute hold time, and 200-300˚C cooling rate. The temperature of the sample was monitored using an optical pyrometer, and the cooling rate was achieved by shutting off the instrument and letting the sample cool to ambient temperature. The graphite foils on the SPS sintered samples were then ground off, and the samples were annealed in air at 900˚C for 8 hours with a 2˚C/minute heating rate and 10˚C/minute cooling rate.

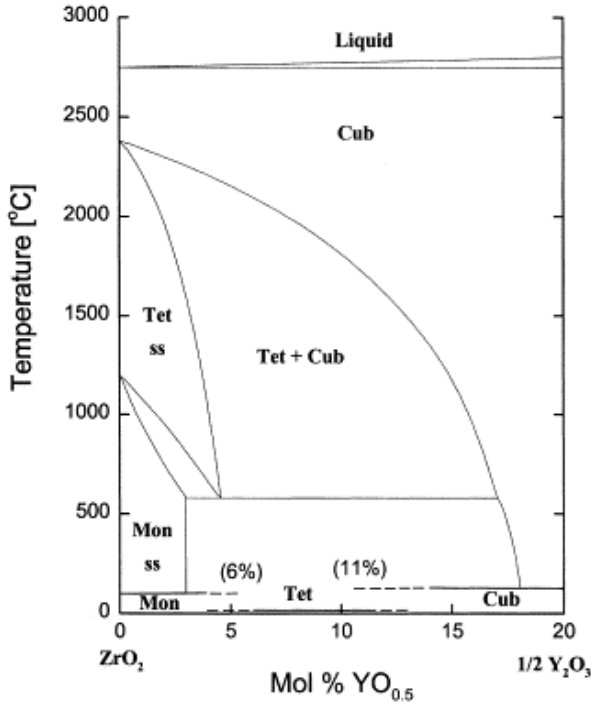

FIGURE 7. Phase diagram of yttria stabilized zirconia[41].

For tetragonal 4YSZ, powders were weighed to make powder compacts using a 13mm diameter Specac die with a Carver press. The powders were pressed at 7 tonnes for 5 minutes to reach a green body density ~50%. The green bodies of 4YSZ were then sintered in air using a CM Furnaces Inc. (Bloomfield, NJ, USA) 1700C tube furnace with a mullite tube at 1250˚C for 18 hours with a 10˚C/min. heating and cooling rate.

For the 4YSZ-hBN composite samples, powders were first weighed then ball milled in ethanol using 5mm diameter zirconia milling media. The ball mill was run at 40rpm for 12 hours. The milled powders were then dried in a rotary evaporator and were ground using a mortar and pestle. Polyvinyl alcohol (PVA) was added as a binder to the 4YSZ-hBN composite powders prior to pressing to assist homogeneous compaction of these powders into green bodies. 3 vol % PVA was added to the 4YSZ-hBN powders by first dissolving the PVA binder in distilled water at 80˚C. The 4YSZ-hBN powders were then added with continuous stirring. The PVA, 4YSZ, hBN powders were dried at 110˚C overnight then ground with a mortar and pestle. They were then weighed, and powder compacts were made in the same manner as mentioned above. The green bodies of the composite were heat treated at 450˚C for 8 hours with a 5˚C/minute ramp rate to remove the polymer. The 4YSZ-hBN composite was then sintered in nitrogen using a CM Furnaces 1700C tube furnace with a mullite tube at 1365˚C for 12.5 hours with a 10˚C/min. heating and cooling rate.

2.2 Sample Preparation Techniques

To study the degradation of the abradable coating, any underlying substrate and bond coat material was polished off using rough grit silicon carbide paper (80 or 120 grit) to make free-standing coatings. The as received coatings (roughly 760 μm thick) were then heat

treated to remove the polymer pore former at 450˚C for 8 hours with a 5˚C/minute ramp rate as suggested by the powder manufacturer. Cross sections for both the coatings as well as bulk material samples were then cut using a high-speed diamond bladed saw, mounted in epoxy, and polished with the procedure outlined in Table II.

TABLE II. Polishing steps outlined for abradable coating specimen preparation.

Polishing Step	Polishing Medium	Duration*
1	SiC grit P400	Until planarized
2	SiC grit P800	10 minutes
3	15 μm diamond solution	20 minutes
4	6 μm diamond solution	20 minutes
5	3 μm diamond solution	20 minutes
6	1 μm diamond solution	10 minutes
7	0.25 μm diamond solution	5 minutes
8	0.02-0.06 colloidal silica	5 minutes

*duration is adjusted to longer times if necessary based on optical microscopy investigation

2.3 Microstructural Investigation

After polishing, the samples were cleaned by sonication in 1) acetone, 2) ethanol, and 3) distilled water for ten minutes each. They were then coated with iridium or carbon in preparation for scanning electron microscopy (SEM) imaging to determine the microstructure of the coating using FEI Company (Hillsboro, Oregon, USA) Quanta or Magellan Field Emission Gun SEMs. Scanning electron microscopy uses an electron source and electromagnetic lenses to focus an electron beam onto the surface of the sample. As the beam is rastered across the sample surface, it interacts with the atoms in the sample. There are several types of signal given off from the electron beam interacting with the sample (shown in Figure 8, below), but secondary electron or backscattered electron signals were used in this work. Secondary electron signal

comes from the part of the electron beam interaction volume close to the surface and provides topographical information. Backscatter electron signal has higher energy and comes from deeper within the interaction volume. Backscatter electron signal gives you compositional information based on the difference in atomic number contrast seen in the image; higher atomic number elements show up brighter in backscatter electron images[45,46]. SEM images were taken, and ImageJ analysis software (US National Institute of Health, Bethesda, MD USA) was used to analyze the area fraction of the porosity and secondary phase using thresholding based on backscatter contrast seen in the SEM images.

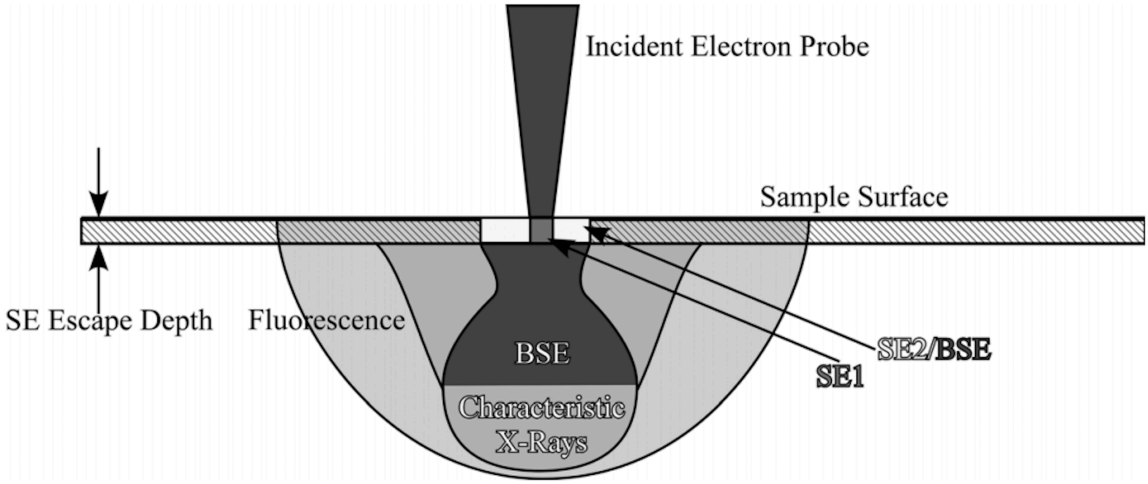

FIGURE 8. Schematic showing the electron interaction volume and types of signal generated[45].

2.4 Phase Analysis

Analysis was performed to determine the initial phases present in the coatings. The structure of the matrix phase, stabilized zirconia, was analyzed. It was also necessary to confirm the as-processed state of the boron nitride secondary phase in the DySZPB coatings since it was processed in air. Since light elements cannot accurately be assessed using SEM energy dispersive spectroscopy (EDS) without a windowless EDS detector system, other methods were

explored to identify the BN secondary phase. In addition, the secondary phase being at very low concentration (less than 1 wt.%) made it especially difficult to detect.

2.4.1 X-ray Diffraction

Powder x-ray diffraction (XRD) was performed on a Rigaku Corporation (The Woodlands, TX, USA) Ultima III X-ray Diffractometer with a Cu k-alpha source with 1.54Å wavelength. The diffracted x-rays from different plane (hkl) orientations in the crystalline sample were picked up by the x-ray detector that was scanned across a set range of diffraction angles, 2θ. These 2θ peak positions were plotted versus intensity. Bragg's law of constructive interference (shown in Equation 1) relating the diffraction angle (θ), incident x-ray wavelength (λ), and interplanar spacing (d) in the lattice was used to determine d, and subsequently the unit cell parameters of the crystal with the Equations 2a and 2b for cubic (lattice constant a) and tetragonal unit cells (with lattice constants a, a, and c), respectively[46–48]. Rigaku's integrated x-ray powder diffraction software (Integrated X-ray Powder Diffraction Software, PDXL) was used to match the measured diffraction patterns to those in the International Centre for Diffraction Data (ICDD) database.

$$n\lambda = 2d\sin\theta \qquad \text{Eq. 1}^{47}$$

$$\frac{1}{d^2} = \frac{h^2+k^2+l^2}{a^2} \qquad \text{Eq. 2a}^{47,48}$$

$$\frac{1}{d^2} = \frac{h^2+k^2}{a^2} + \frac{l^2}{c^2} \qquad \text{Eq. 2b}^{47,48}$$

2.4.2 Raman Spectroscopy

Raman spectroscopy was employed using a 532nm laser on a Renishaw (Wotton-under-Edge, UK) inVia Raman Microscope. This technique was specifically useful for the analysis of the BN phase in the DySZPB coatings, which is present at low quantity (<1 wt.%). The characteristic peak at 1366cm^{-1} for hexagonal BN was able to be tracked between the starting powders and the as sprayed coatings [49].

Raman spectroscopy utilizes monochromatic light, in this case, from a 532nm wavelength laser, as a photon source that excites specific bond vibration modes in the material. The intensity and shift in frequency of the incident laser interacting with the sample was plotted. The incident laser interacts with the sample through Rayleigh, Stokes, or Anti-Stokes scattering. Rayleigh scattering of the incident photon is an elastic process, while Stokes and Anti-Stokes scattering are inelastic[48]. These scattering processes are illustrated in Figure 9. The Stokes inelastic scattering events where there are decreases in frequency of the incident laser interacting with the sample are utilized in this work. To ensure accurate measurements, a standard Si wafer with a characteristic peak at 520.5cm^{-1} was run.

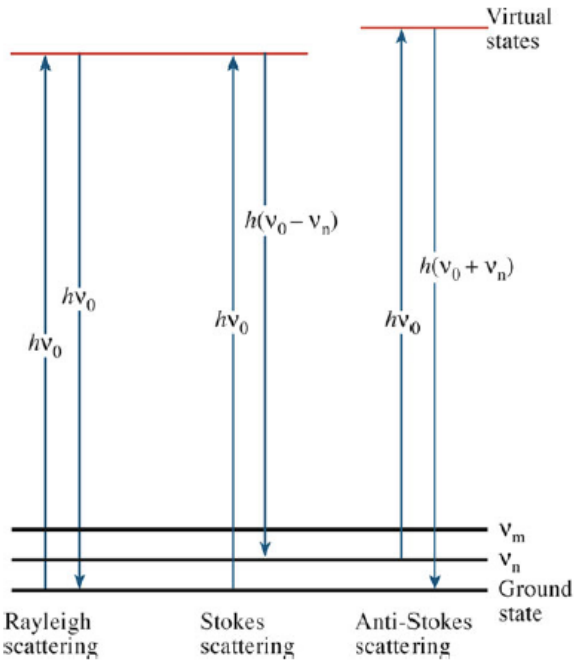

FIGURE 10.19. Transitions occurring in Raman spectroscopy.

FIGURE 9. Schematic showing the scattering processed utilized in Raman spectroscopy[48].

2.4.3 Additional Techniques

Additional analysis techniques were completed as supplemental evidence with assistance from the Irvine Materials Research Institute (IMRI) staff, specifically, Kenta Ohtaki. Transmission electron microscopy (TEM) using an FEI Philips CM20 TEM was used by IMRI staff to confirm the absence of hBN in the as-processed coatings. TEM uses the electron interactions detected in transmission mode, which allows higher resolution imaging than SEM, with a thinned sample (<200nm thick) that it is optically transparent[46,48]. The sample was thinned with assistance from IMRI staff using either a Tescan Gaia or FEI Quanta dual beam SEM with Focused Ion Beam (FIB) milling. Additionally, scanning transmission electron microscopy (STEM) was performed by IMRI staff on a Tescan Gaia SEM to confirm the presence of domain formation after indentation on bulk samples of YSZ and DySZ.

2.5 Aging Experiments

The performance of the abradable coatings in a representative working environment was examined using a high temperature, controlled atmosphere tube furnace (CM Furnaces Inc., Bloomfield, NJ USA). A mullite tube was used since it has higher resistance to thermal shock than alumina. A mixture of nitrogen and oxygen at a ratio of 80:20 and a flow rate of 80sccm was first fed through a heated water tank before entering the tube furnace. The temperature of the water tank controlled the amount of water vapor in the atmosphere that was flowed across the sample. For a water vapor percentage by partial pressure of 9.5% H_2O (v), which was representative of natural gas fired turbines, the tank was heated to 45˚C[2]. Additionally, the inlet tubes and flanges are wrapped in heating tapes and heated to >100˚C to ensure no water condensed in the tube. The furnace set up is shown in Figure 10. Additional drawings for the fixtures and supports designed specifically for this setup are included in Appendix A.

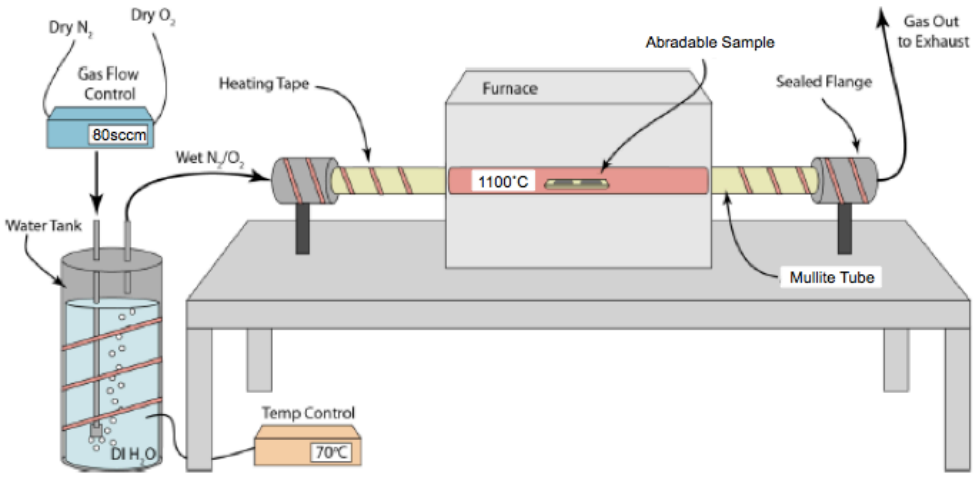

FIGURE 10. Schematic showing the set up of the high temperature, controlled atmosphere tube furnace used for aging experiments.

Prior to starting the furnace program and after the water tank had reached the set temperature, the gas flow was turned on and the system was purged in a wet environment for two residence cycles at a furnace and heating tape temperature of 150˚C. The furnace program was

then started, and the coatings were exposed to 9.5% or 30% H_2O (v) at 1100˚C with a 10˚C/minute ramp rate for 10-145 hours.

2.6 Investigation of Wear Behavior

Abradable coating samples were tested for wear behavior using representative lab scale tests to simulate the combination of normal and shear loading experienced during service. Indentation tests were first used to evaluate the hardness of the coatings. It is known that as hardness increases, abradability decreases so the change in hardness of the DySZPB and the YSZP coatings will correlate to how the abradability of these coatings will evolve in service. To evaluate the wear characteristics, indentation scratch testing was used. Ideally, an abradability test rig simulating the impact of turbine blades at working impact velocities and temperature would be used. However, these rigs are currently only being run in industry and investigation into the feasibility of designing and building such a rig put those experiments out of the scope of this PhD project. Scratch testing was used as a comparative evaluation tool of the wear behavior of the exposed coatings although it is not a representation of coating wear behavior at working temperature. The mode of material removal during scratch testing can give insight into how the material will behave in service.

2.6.1 Vicker's Indentation

One surface of the free-standing abradable coating samples was polished up to 0.25µm in an epoxy mount (following the steps outlined previously in Table II). The epoxy-mounted sample was then cleaned in acetone by sonication for 5 minutes and heat treated in a resistively heated furnace in air at 700˚C for 1 hour with a ramp rate of 3˚C/minute to burn off the epoxy. The unpolished side of the sample was then planarized to ensure the sample for indentation was

flat. The sample was then mounted using a minimal amount of crystal bond to a steel puck with planar faces in preparation for Vicker's indentation. At least five indents were made with a diamond Vicker's indenter tip at loads ranging from 1-10 kg-f. Indents were placed away from the coarse porosity present on the surface of the coatings. The diagonals (shown in Figure 11) of the indent were then measured using an optical microscope and recorded to calculate the Vicker's hardness according to Equation 3.

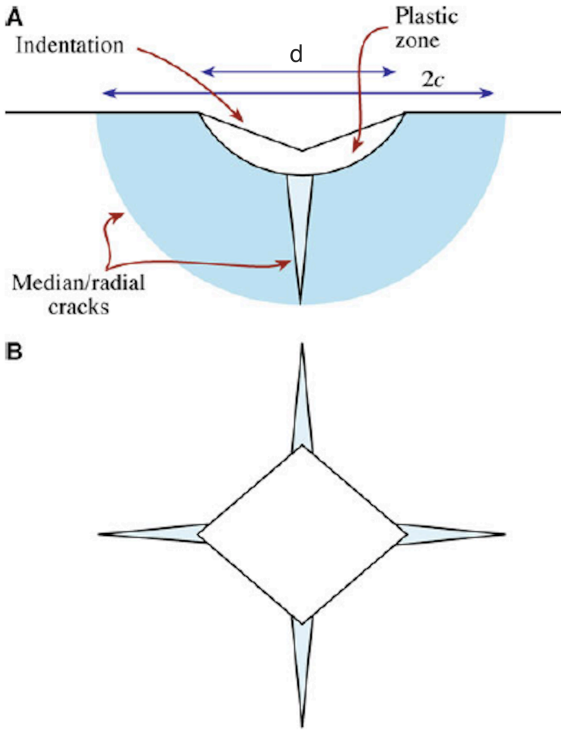

FIGURE 11. Vicker's indent showing measurement of diagonal, d[48].

$$HV=1.854*(P/d^2) \qquad \text{Eq. 3 [48]}$$

2.6.2 Nanoindenter Scratch Testing

Samples were polished and prepared for nanoindentation scratch testing in the same manner as described above in Section 2.6.1 for Vicker's indentation. An Agilent Technologies G200 Nano Indenter was used with a diamond conical tip made by MicroStar Technologies (Huntsville, TX USA) with a 5 +/- 1 μm radius and 120 +/- 5˚ angle, as illustrated in Figure 12. Single pass, ramp load scratch tests were performed using the procedure outlined in the G200 Manual supplied by the manufacturer with the XP indenter head designed for use with stiffer materials. First, a profile of the surface was measured at low load, 50μN in these experiments, to map the original morphology of the surface. Next, along the same track, the normal load was gradually increased from 0 mN to a maximum load of 400 mN with parameters outlined below in Table III. Lastly, the scratch profile was measured by another pass at low load, 50μN, to map the topography of the scratch profile[50].

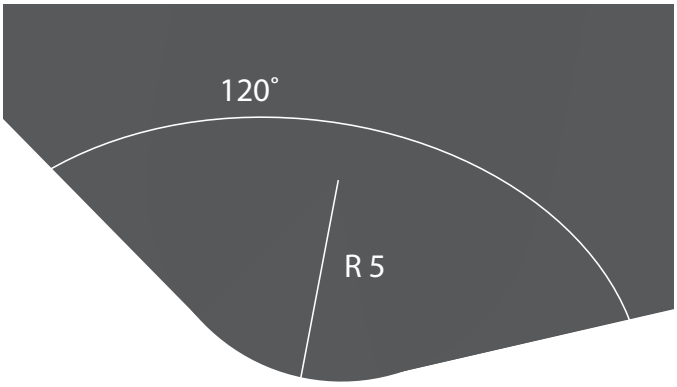

FIGURE 12. Schematic showing the geometry of the conical diamond tip indenter used for nanoindenter scratch testing experiments.

TABLE III. Single pass, ramp load scratch test parameters.

Scratch Test Parameter	Unit
Max. Scratch Load	500 mN
Profiling Load	50 μN
Profiling Velocity	50 μm/s
Scratch Length	500 μm
Scratch Velocity	5 μm/s

2.6.3 Macroscratch Testing and Damage Zone Analysis

To test the wear behavior of the abradable coatings with an indenter at a more representative scale to wear with a turbine blade, single pass scratch tests were performed at constant load with a standard Vicker's indenter. Samples for this macroscratch test were prepared in the same manner as samples for Vicker's indentation, as described above in Section 2.6.1. During the test, an indent was made with a 1 kg-f load and held constant at maximum indent depth for 60 s during which a scratch was made across the surface approximately 3-5 mm long. The horizontal motion was controlled manually by a micrometer with approximate speed around 50-100 μm/s. At least two scratches were performed on each material.

The damage zones beneath the scratches were of interest to understand how the microstructure beneath the scratch changed after damage. This damage zone was investigated by cross sectional analysis using SEM. Samples were prepared after scratch testing by first marking the scratch positions, which were visible by eye, with permanent marker. The samples were then mounted cross sectionally in epoxy in preparation for polishing. The polishing steps outlined in Table II were followed with extra time spent on the first roughest grit paper, P400. During this first polishing step, half the length of the scratch was removed so that the damage at the midpoint

could be analyzed (significant time was spent on this removal step). Samples were then cleaned and coated in preparation for SEM.

2.6.4 Vibrometer

A Polytec MSA-500 Micro System Analyzer (vibrometer) was used to map the surface topography of the sample after mechanical testing. The vibrometer uses the theory of white light interferometry to map the z position (height) of each pixel in an optical image of the specimen. Figure 13 shows the setup of the Polytec instrument with a similar configuration to a standard optical microscope. The main differences are the use of an interferometric Mirau objective lens and a piezoelectric stage to move the interference objective vertically[51,52]. A 20x Mirau objective lens was used for these experiments with measurement parameters chosen for a smooth surface with the smallest step size (89 nm).

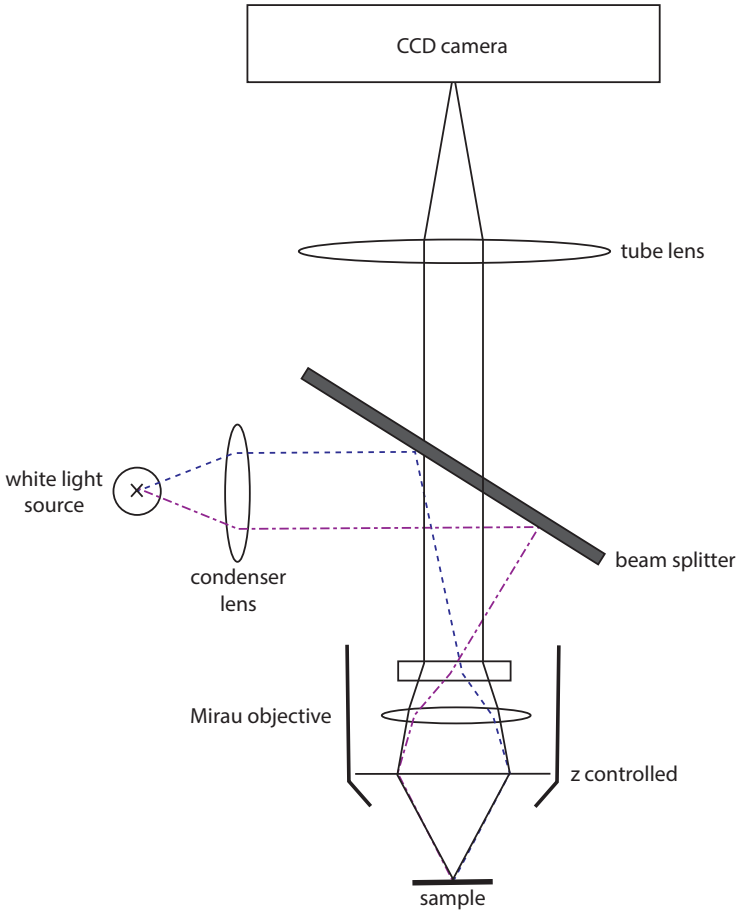

FIGURE 13. Setup of an interferometric optical microscope with a Mirau lens[51].

The principle of white light interferometry uses a beam splitter to divide the white light source into reference and objective beams. The two beams are then recombined to make an interference signal, which is analyzed by the Polytec TMS Software V3.6 to determine the difference in paths of the two beams[53]. The interference signal for each pixel is analyzed by scanning a range of z positions, and the z position of a pixel is determined when the interference of that pixel has maximum modulation. Maximum modulation occurs when the optical path length of impinging light is the same for the reference and objective beams[51].

CHAPTER 3: Towards A Mechanistic Understanding of Ceramic Abradable Coating Design and Damage Accommodation

3.1 Introduction

Hot section abradable coatings play an integral role in not only providing thermal protection for turbine shrouds, but also in maintaining blade tip clearances for increased turbine efficiencies by acting as sacrificial material that can be easily removed when rub impact occurs with turbine blade tips[24,32,54]. As technology advances, there is a push for the development of advanced abradable coatings that can withstand more severe operating conditions and retain the optimum balance of abradability and durability. However, as abradable coating technologies are pushed to higher temperatures and greater capabilities, such as compatibility with ceramic matrix composites, there are significant gaps in understanding the underlying mechanisms and applicable fracture mechanics analysis that aid the design of these inherently brittle materials enabling them to accommodate damage in a controlled manner.

A parallel ceramic material challenge is that of designing ductile or tough ceramics. Significant work has been done to establish pathways for material processing and microstructure design that impart toughness through not only intrinsic mechanisms, but also extrinsic ones[13,55–58]. There are established methods for analyzing and understanding the fracture mechanics of these mechanisms enabling predictive capabilities for failure of toughened ceramic systems both in bulk and as coatings[58–62]. The aim of this work is to use relevant theories for fracture mechanics and wear mechanisms in ceramics to establish pathways for developing a mechanics framework for understanding, analyzing, and predicting damage accommodation in ceramic abradable coatings.

3.2 Current APS Ceramic Abradable Coatings

Current understanding of abradable coating damage accommodation is limited to metal matrix based or low temperature abradable coatings for lower pressure and temperature sections in the turbine[21,31,63]. Since ceramics have limited dislocation motion and therefore, little plastic deformation, ceramic abradable coatings will exhibit different damage accommodation mechanisms. Ceramics inherently have low damage tolerance and are brittle with low ductility and poor fracture toughness[56]. Most fracture mechanisms in ceramics are approximated using linear elastic fracture mechanics (LEFM), which assumes only a sufficiently small plastic zone exists around a crack tip[64]. In LEFM, the majority of the mechanical energy is transferred to:

- internal energy, which is absorbed by bonds;
- surface energy, which is used to create crack surfaces;
- dissipated energy, which is lost to friction; or
- kinetic energy, which is used to move material[64].

Key issues seen in current technology ceramic abradable coatings are blade tip wear and material transfer from the coating to blade tip[54,65,66]. This occurs because the energy of the rub impact between the blade tip and coating is unable to be accommodated by the abradable coating and is thus transferred to the blade tip. However, coating compaction in some ceramic abradable coating systems has also been observed, which suggests the coating has undergone some plastic deformation[54,65,67]. Thus, damage accommodation in all ceramic abradable coatings cannot be fully explained by LEFM.

The design of current technology ceramic abradable coatings utilizes air plasma spray processing (APS) with tetragonal yttria stabilized zirconia (YSZ), or variants thereof, as the matrix material[24,40,67,68]. Additional APS processing modifications or material modifications

have been made to increase the abradability of YSZ; the strategies are discussed below and illustrated in Figure 14 as compared to that of typical APS microstructures (shown in Figure 14A).

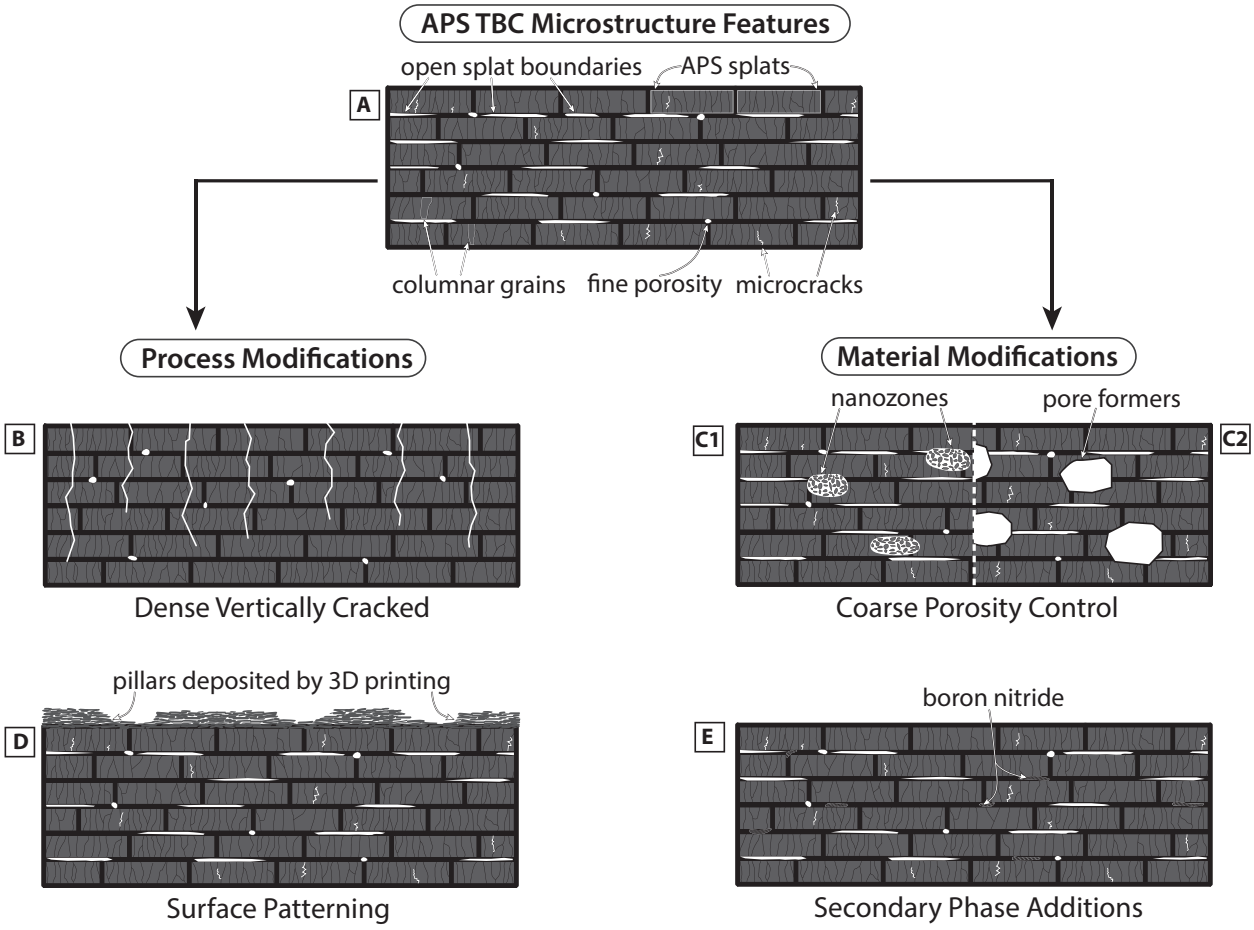

FIGURE 14. Schematic showing different design strategies for enabling abradability in ceramic APS coatings. Image A shows typical APS microstructural features, while images B and D show process modifications, such as dense vertical cracked microstructures (B) or pillars deposited on the coating surface (D). Images C1, C2, and E show material modifications. C1 and C2 show nanozone features and coarse porosity while E shows secondary phase additions.

3.2.1 Design

3.2.1.1 Pore Formers

A material modification that has been used is that of adding in a fugitive polymer pore former (Figure 14 C2). Careful tuning of coating porosity between 25-40%, achieved by

adding in pore formers, allowed the optimum balance of necessary solid particulate erosion resistance while maintaining abradability and low blade damage[20,27]. For example, dysprosia stabilized zirconia (DySZ) abradable coatings with less than 30% porosity require blades to be tipped with abrasive material, such as SiC or cubic BN, to prevent blade wear. While DySZ coatings with porosity above 30% can be used with untipped blades under certain rub impact conditions. Blade tipping is expensive and has limited longevity since SiC and cubic BN will undergo oxidation and volatilization in service, especially in the presence of water vapor [3].

An additional strategy that has been done to ensure reproducible levels of porosity is spraying with nano-agglomerated feedstock powders to retain partially unmolten agglomerates, referred to as nanozones, in the sprayed coatings. The nanoparticles are agglomerated via spray drying then partially sintered prior to spraying in APS. The resulting nanozone features are illustrated in Figure 14 C1. This not only helps maintain consistent levels of porosity, but the nanozones have been shown to increase coating toughness or abradability depending on whether the molten part of the semi-molten particle has infiltrated the unmolten agglomerated structure; toughness increases if the unmolten agglomerate has been infiltrated and abradability increases if not[34,67,69]. These nanozones, however, will sinter and densify in service with aging studies showing the diameters of the features in the nanozone increasing to more than twice the size with 50 hours of aging in air at 1100˚C[69].

3.2.1.2 Secondary Phases

Another material modification used to increase abradability is the use of an additional secondary phase; an example is illustrated in Figure 14 E. Secondary phases can be used as additions intended to reduce interfacial splat bonding in the tetragonal zirconia matrix. Small fractions of a solid dislocator phase, such as hexagonal boron nitride (hBN), or larger

fractions of a different structure oxide phase have been used[25,28,68,70]. Using hBN as a dislocator phase has been shown to decrease damage to the blades upon contact with the abradable coating [24,68,71]. Novinski, et al [72] used magnesia and M. H. Foroushani, et al [26] used lanthanum phosphate as the secondary phase in addition to the zirconia matrix. S. Ebert, et al [70] employed a larger fraction of oxide secondary phase using magnesium aluminum spinel as the top layer in a double layer abradable coating system.

3.2.1.3 APS Dense Vertically Cracked

There have also been processing modifications used to improve the performance of zirconia based abradable coatings. E. Scrinzi, et al [24] used dense vertically cracked (DVC) air plasma sprayed coatings, which showed improved erosion resistance, adhesion strength, and furnace cycling resistance as compared to porous coating systems. These DVC APS coatings are made using a variant of air plasma spray processing that aims to increase the strain tolerance of APS coatings by engineering vertical cracks through a portion of the thickness of the coating (shown in Figure 14 B). Vertical cracking is attained by controlling the temperature gradients, which develop during the process and are primarily achieved by heating the substrate, as the coating is deposited[73]. Substrate heating allows for re-melting of the powder splats as they are deposited on the hot surface creating good contact between splats. As the individual splats cool, they are constrained by the underlying substrate or splats and develop stresses that lead to crack initiation and propagation[73]. These vertical cracks mimic the columnar grains produced by the EB-PVD process and provide strain tolerance to accommodate for the thermal expansion mismatch between substrate and coating that develops during operation[9,73,74].

3.2.1.4 APS with Patterned Surface

An additional processing modification is the deposition of an additional layer of material to make a patterned surface on the APS abradable coating (illustrated in Figure 14 D). The use of a patterned surface is proposed to keep the full abradable coating bonded to the shroud, even after the blade-coating rub impact, preventing debris formation that can damage downstream components[29,75]. Patterning the shroud surface also improves aerodynamics. Bucci, et al [29] used a zirconia-based abradable coating first applied by DVC APS with an additional patterned layer then deposited using 3D printing. Patterned surfaces have also been used on abradable coatings for lower temperature sections in the turbine[76].

3.2.2 Analysis

The microstructural design resulting from different material or process selection in these ceramic abradable systems is hypothesized to affect the existing damage accommodation mechanisms. Current work has focused on fully understanding and characterizing the processing methods to produce certain microstructural features, which have been shown to perform well in simulated abradability tests, but the underlying mechanisms that enable abradability have not been identified. The testing methods for evaluating abradable coatings thus far have relied on low temperature wear and furnace cycling tests on the lab scale, or high temperature rub rig testing and erosion tests, on an industry scale[20,24,70]. An illustration showing the complexity of an industrial scale test rig is shown in Figure 15[37]. Evaluation has relied on qualitative assessment post testing, and currently, there exist no predictive models that are able to incorporate the rub impact conditions, such as blade speed, depth of incursion, etc., and microstructural characteristics, such as percentage of porosity, concentration of pre-existing

flaws, or interface toughness. This study aims to present expected damage accommodation mechanics dependent on the existing microstructural characteristics of different designs in hopes to establish a better understanding of the synergistic effect of ceramic deformation mechanisms operating in high temperature, ceramic abradable coatings.

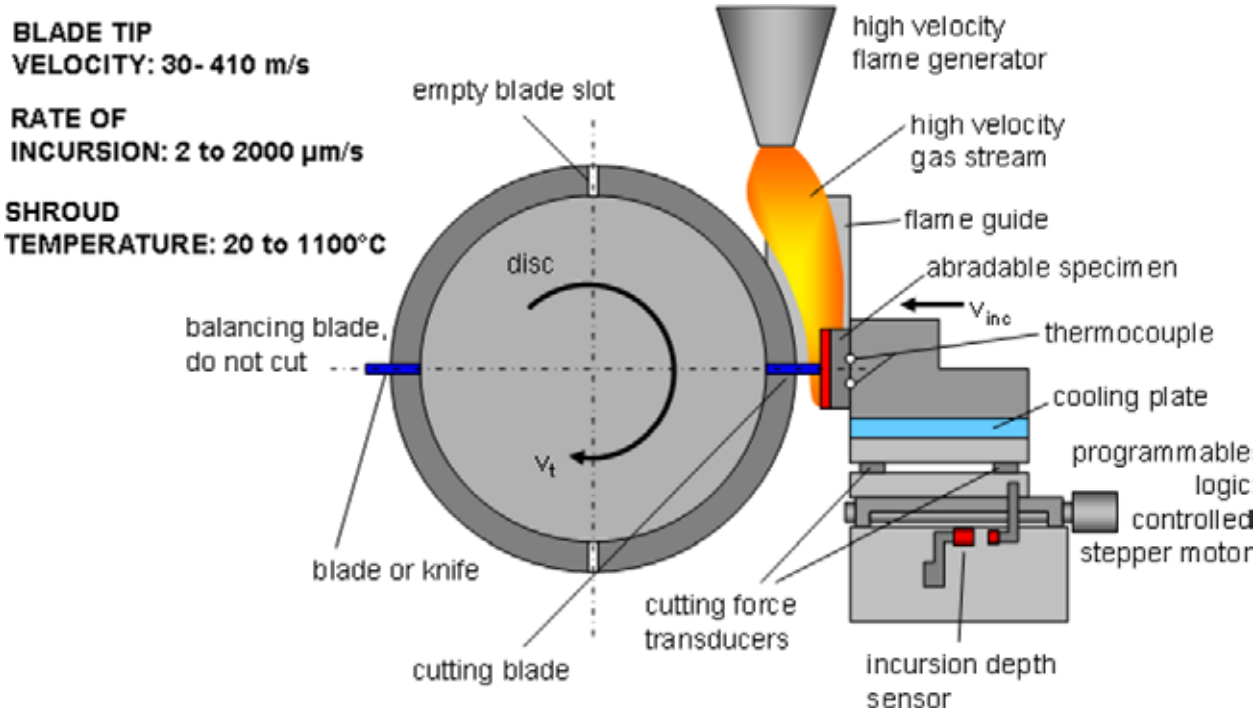

FIGURE 15. Illustration of industry-scale, abradable test rig facility from Oerlikon in Switzerland[37].

3.3 Proposed Damage Accommodation Mechanisms and Associated Analysis

The potential damage mechanisms occurring upon interaction with the blade for the aforementioned ceramic abradable coating design strategies are illustrated in Figure 16. This study will focus primarily on the first interaction and mechanism of energy transfer from the blade tip to the abradable coating. It is hypothesized that the first interaction will define the nature and pathway of the subsequent material deformation. These subsequent interactions in each design strategy will be dominated by transfer of energy through dissipation and kinetics to

move the blade through the coating and redistribute the material; these interactions will not be addressed in this work.

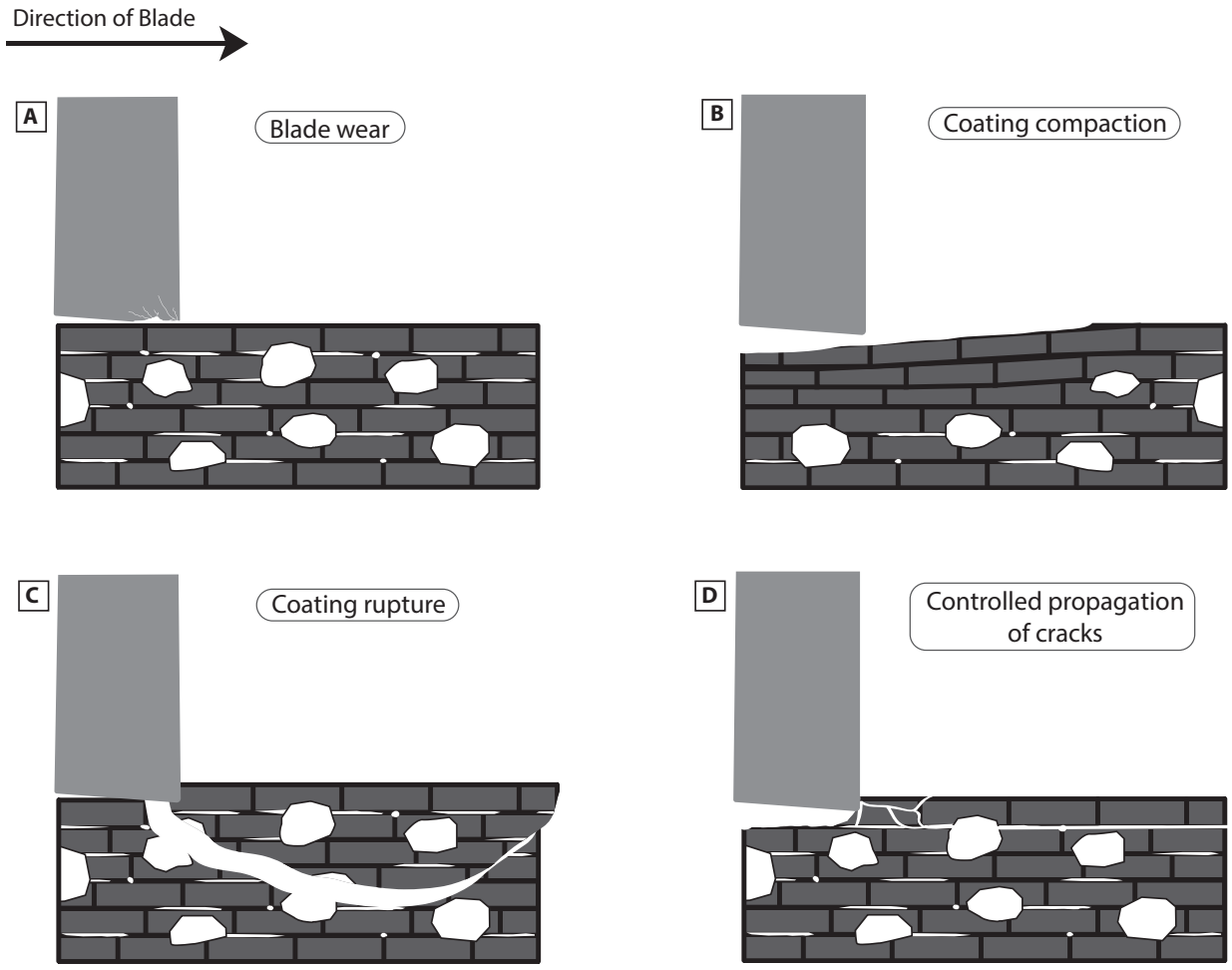

FIGURE 16. Illustrations showing the expected blade-coating interactions. Images A and C show unfavorable interactions that result in blade wear (A) or coating rupture (C). Images B and D show favored interactions with B illustrating coating compaction and D showing controlled propagation of cracks.

Figure 16 A and C show unfavorable blade-coating interactions, which both result in the formation of a large gap between casing and blade tip providing a poor seal. Blade wear (Figure 16 A) results when the abradable coating is unable to absorb the energy of the rub impact because of its high hardness or toughness. Coating rupture (Figure 16 C) occurs when the coating undergoes uncontrolled brittle fracture. Coating rupture can occur with external drivers, such as foreign object damage eroding the coating due to low toughness, or internal drivers, such

as thermal cycling failure or blade rub impact causing crack propagation to penetrate deep within the coating.

With existing designs, the favorable damage accommodation mechanisms, shown in Figure 16 B and D, can be separated into two main categories based on the dominant fracture mode, and energy dissipation mechanism. The first relies on pseudo-plastic deformation, which is assisted by coating porosity allowing compaction or high temperature plasticity enabling material redistribution. The second is elastic fracture controlled by additional secondary weakening phases or assisted by the existence of pre-existing flaws. The associated mechanics for both favorable damage accommodation mechanisms, pseudo-plastic deformation and controlled propagation of cracks, will be discussed below.

3.3.1 Deformation Mechanisms Allowing Coating Compaction and Material Redistribution

Figure 17 illustrates potential deformation mechanisms for pseudo-plastic fracture of an abradable coating in a porous APS coating or APS coating with a patterned surface, which can be represented as surface porosity. The material above the pore may undergo microcracking, which is arrested by the pore, followed by the redistribution of the microfractured material into the pore cavity (Figure 17 A). On the other hand, the material may redistribute to the pore cavity through interface sliding (Figure 17 B). In order to understand which mechanism is occurring in these inherently brittle ceramic materials enabling them to undergo compaction and material redistribution, the concentration of open space pre-existing in the material, magnitude of the plastic deformation zone, and concentration and distribution of median, radial, and lateral cracking must be taken into account. Since these coatings operate at high temperatures, the role

of high temperature exposure and the effect of plastic deformation occurring in the coating also play a role.

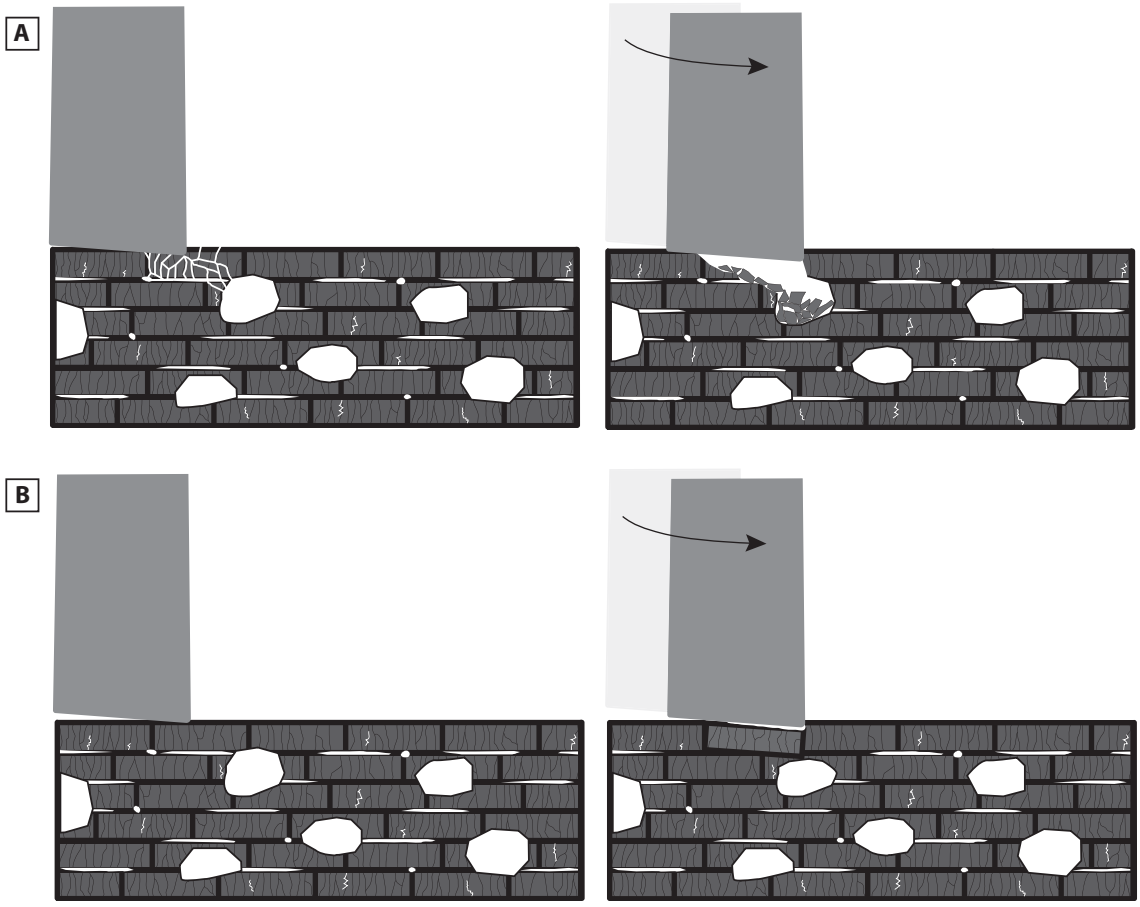

FIGURE 17. Schematic illustrating two methods by which pseudo-plastic fracture can enable coating compaction with A showing microcracking and redistribution of the cracked material and B showing splat boundary sliding.

3.3.1.1 Role of Indentation Fracture Behavior

Theories for abrasive wear in ceramics can be applied to describe the material behavior illustrated in Figure 17 A. The system can first be described by the response seen with only an applied normal force. With this indentation load, the material responds elastically first and produces Hertzian cone cracking once a critical load has been reached, which is proportional to the elastic properties of the indenter and coating material as well as indenter geometry and contact area[77,78]. There is then plastic deformation, which results in a plastic deformation zone

with further median, radial, and lateral cracking into the material (shown in Figure 18). The tangential force component can then be introduced and investigated using abrasive wear in ceramics. The extent of lateral and radial crack propagation is controlled by the coating hardness and fracture toughness with low hardness and low fracture toughness materials undergoing more radial and lateral cracking[77,79,80]. For coating compaction through material transfer of the microfractured material into a pore cavity, high hardness to reduce the plastic deformation zone, high concentration of porosity, and minimal median crack propagation into the material are essential.

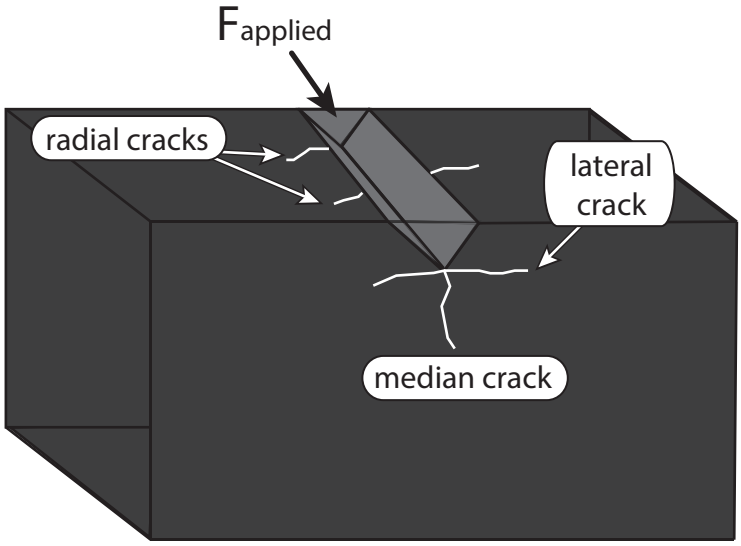

FIGURE 18. Illustration shows median, radial, and lateral cracking under a scratch track.

With a sufficiently small plastic deformation zone, crack propagation can be understood using linear elastic fracture mechanics[81]. The depth of median crack propagation can be reduced by maintaining a high concentration of weak interfaces, produced from the presence of coarse or fine intersplat porosity, parallel to the applied tangential force. The median cracks should reach the weakened splat interfaces and kink into them, propagating horizontally along the direction parallel to the applied tangential force. The propagating crack should follow this path as long as

the fracture energy ratio of the interface ($R_{i/f}$) to bulk material (R_{splat}), $R_{i/f}/R_{splat}$, is less than 0.57, which is the condition for an interface crack to remain in a homogeneous interface across which there is no elastic mismatch[82]. These weakened splat interfaces can be treated here as a layer containing porosity and the bonded splat material as YSZ ligament connections. There is assumed no elastic mismatch because the material fracturing is YSZ at the interface and bulk. A study done by Davis, et al [83] on crack deflection in an alumina ceramic with porous interlayers has shown that the existence of pores or microcracks near the propagating crack tip can increase the stress intensity factor at the crack tip, thus reducing the fracture energy of the material in the interface (or ligament). Using that framework, the fracture energy condition relating the decrease in fracture energy of the interface due to porosity (using the volume of porosity, Vol_{pores}) then becomes Equation 4 [83].

$$R_{i/f} / R_{splat} < 0.57\,(1\text{-}Vol_{pores}) \qquad \text{Eq. 4 [83]}$$

The percentage of porosity in the interface must reduce the interfacial fracture energy according to Equation 4 to keep the propagating crack in the horizontal interface. If this condition is not met, there would be extensive median cracking deep into the coating material, and coating rupture will occur.

3.3.1.2 Role of High Temperature Induced Plasticity

High temperature induced plasticity in ceramics can be applied to describe the material behavior illustrated in Figure 17 B. Softening at the splat interfaces in the abradable coating must occur to allow the material to deform under the first rub impact then sliding along the interfaces would enable redistribution of the deformed material to deposit into the pore cavities. Plasticity mechanisms would allow this behavior, and superplastic deformation has been reported for bulk, fine grained tetragonal YSZ for strain rates on the order of 10^{-2} - 10^{-4}/s

[84,85]. The main mechanism for superplasticity at high temperatures is enhanced dislocation motion and grain boundary sliding, which is enabled by nanograin sized YSZ[86]. An additional study on nanograined YSZ by He, et al [87] showed that hardness and elastic modulus of YSZ decrease with high temperature indentation experiments at 1200˚C due to enhanced plasticity. The key to enabling plasticity in ceramics through grain boundary sliding is the maintenance of a high concentration of interfaces, and thus the maintenance of small grains even at elevated temperatures. Thus an abradable coating with a high concentration of splat interfaces, and thus, a small splat feature size is advantageous.

Further studies performed on deformation of YSZ thermal barrier coatings at high temperatures describe the plasticity mechanisms using viscoplasticity models[88]. The Willam-Warnke model and Walker models have been used and are able to encompass the strain rate dependency and tension/compression asymmetry but are difficult to implement for experimental systems without accurate measurements of necessary parameters at relevant temperatures[88].

3.3.2 Elastic Deformation Mechanisms Allowing Controlled Propagation of Cracks

Abradability may be enabled through elastic deformation mechanisms with controlled propagation of cracks facilitated by interface weakening secondary phases or through introducing a high concentration of flaws, like in DVC coatings. The pre-existence of flaws could be utilized to decrease the fracture energy of those areas of the coating when in proximity to a propagating crack. In order to understand these mechanisms and their efficacy in dissipating energy, the interfacial fracture energy as well as the concentration of pre-existing cracks, their orientation, and geometry must be taken into account.

3.3.2.1 Role of Interface Design

Assuming a sufficiently small plastic deformation zone, crack propagation in a composite coating with an interfacial weakening phase can be understood using linear elastic fracture mechanics. While the effect of pre-existing cracks or pores is addressed using criteria with no elastic mismatch across the interface, with a secondary weakening phase, there is an elastic mismatch. In this case, the behavior of the crack and effectiveness of the weakening phase at redirecting the crack is highly dependent on the orientation of the crack and the shear modulus and poisson's ratio of the bulk material as compared to the secondary, weakening phase. He and Hutchinson [89] have done extensive development of models that predict crack deflection at an interface between two different materials. Those models predict the ratios of interface toughness between the secondary phase and bulk phase that result in the crack deflecting into the interface, depending on crack geometry. The importance of the predicted ratio associated with a certain geometry leading to deflection into the interface is realized when looking at the scenario depicted in Figure 16 D, above, that shows the favorable interaction occurring in the coating with controlled propagation of cracks. In this case, the median and lateral cracks that are first formed must deflect at the intercolumnar grain boundaries in an APS splat and reach the horizontally oriented splat boundaries to deflect along that interface in the x direction as shown in Figure 19. The optimal location and condition of secondary weakening phase will dictate where crack deflection occurs. The weakening phase being located along horizontal splat boundaries will prove most effective for cracks to deflect and follow along the direction of tangential force. If the secondary phase does not meet the condition for the impending crack to deflect into the interface, the crack can continue to propagate resulting in a large weakened, damage zone within the coating.

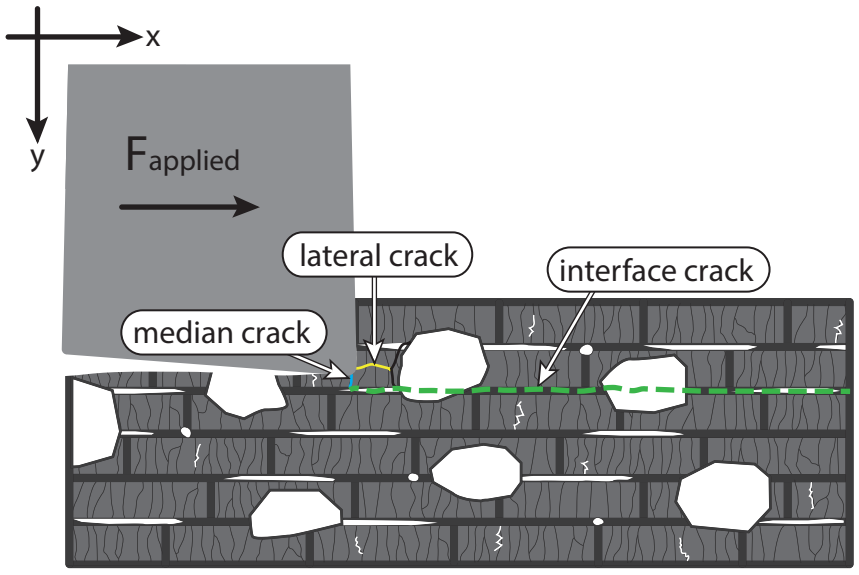

FIGURE 19. Illustration of crack deflection into the horizontal interfaces of an APS abradable coating.

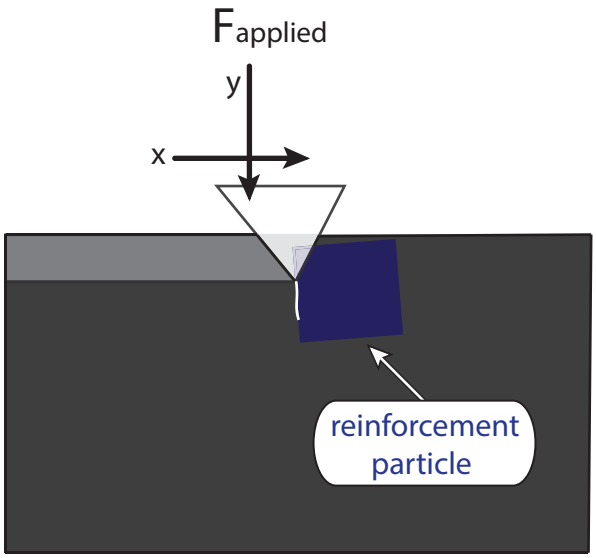

FIGURE 20. Illustration modified from Lee, et al [90] showing crack deflection at the interface of the reinforcement particle.

As an example, Lee, et al [90] showed the effectiveness of using hard reinforcement particles in a ductile matrix, with both phases being isotropic solids, to increase wear resistance by utilizing the deflection of the crack around the reinforcement particles. In their case, the

geometry outlined in Figure 20, the ratio of fracture toughness, $G_{i/f} / G_{reinforcement} < 0.25$ in order for the crack to deflect into the interface[90]. This scenario is analogous to the weakening phase being located along vertical splat interfaces as opposed to horizontal ones. These conditions would result in crack propagation into the coating.

3.4 Summary and Future Directions

This study presents proposed mechanisms by which ceramic hot section abradable coatings can accommodate damage after interaction with turbine blades. The main mechanisms are through coating compaction or controlled propagation of cracks, which have been analyzed using both wear mechanics and linear elastic fracture mechanics theories. In service, each potential deformation behavior discussed above can occur, resulting in synergistic effects not yet explored. Thus, it is imperative for future work to be done in conjunction with resultant deformation behavior observed from field hardware to build an understanding encompassing all relevant mechanisms. Important issues to address with future work are that of understanding the ability of interfacial weakening phases to deflect or absorb cracks with anisotropic secondary phases and incorporating strain rate dependent behavior as well as investigating the effect of different geometries and properties of the abrasive medium.

CHAPTER 4: Microstructural Features Affecting Ceramic Abradable Coating Damage

4.1 Introduction

The utilization of hot section abradable coatings has become increasingly more prevalent in both power generation and aerospace turbine engines because of the important role they play in attaining optimal efficiency through clearance control[24,76]. Implementing abradable coatings in the hot section of the turbine has shown an increase in overall engine efficiency improvements greater than 1% reported[20,22]. These efficiency gains are reached by minimizing blade tip clearances through preferential removal of the abradable coating with any interaction of the blade tip and casing, illustrated in Figure 21.

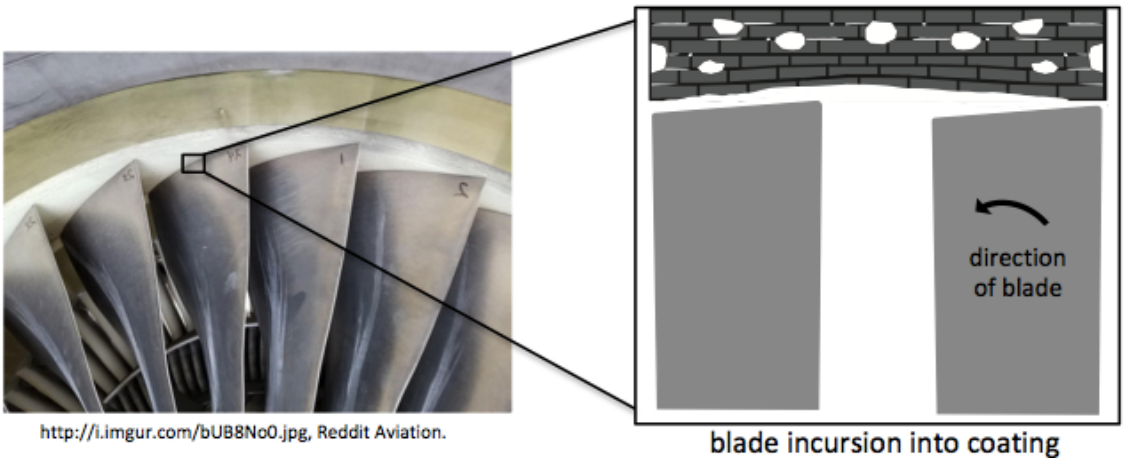

FIGURE 21. Illustration showing location of hot section abradable coating in the turbine.

As advanced combustion, aerodynamics, and heat transfer concepts are developed in combination with ever increasing turbine engine operating temperatures, it is imperative to evaluate and understand the performance of current hot section abradable coating systems in order to guide future design strategies. Currently, hot section abradable coatings are ceramics

based on thermal barrier coating compositions, typically yttria stabilized zirconia (YSZ) or variants thereof, that are processed by air plasma spray (APS) due to its ability to achieve larger coating thicknesses that are required for abradable coatings[9,91]. However, current processing of YSZ, which has been optimized for TBCs, requires modification or additional materials in order to enhance the abradability of those systems. There are also additional temperature limitations to operating temperatures above ~1400˚C for YSZ based coatings due to the unfavorable degradation of the tetragonal prime phase to the cubic and tetragonal phases in YSZ[14].

An additional example of efficiency improvements that require optimized material systems is the implementation of the integrated gasification combined cycle (IGCC) process, which provides efficiency increases over conventional natural gas fired turbines. The IGCC process results in significant changes to the combustion environment to which hot section materials are exposed. Natural gas fired turbines burn ~9.5% H_2O vapor in the combustion environment, while the synthetic gas burned in the IGCC process can have up to 30% H_2O vapor present with the addition of advanced NO_x suppression technologies[2]. Increased water vapor environments have been shown to accelerate degradation mechanisms detrimental to the current material systems, such as enhanced sintering and phase transformations[41,92,93].

Future design ceramic abradable coatings must be compatible with higher engine operating temperatures and more extreme environments as well as erosion resistant to prevent failure with any foreign object damage while still maintaining ease of removal to maintain a tight clearance and prevent damage to the blades. The combination of erosion resistance and abradability thus far has been achieved through careful processing of coating porosity in YSZ based coatings. For ceramic abradable coating systems that utilize both porous YSZ as well as systems of porous YSZ with an additional dislocator phase, such as hexagonal boron nitride

(hBN), it has been shown that low porosity results in high erosion resistance but low abradability and vice versa[20,37]. This connection has led to an established understanding of abradable process optimization for desired APS coating porosity levels, which has been validated by performance based testing[27,40,67]. Current performance testing relies on qualitative characterization of the rub track post rub rig testing and on more quantitative measures of the resistance of the coatings to erosion and temperature cycling[22].

However, current understanding is missing the link between different coating microstructural features and their role in promoting a certain damage accommodation mechanism, which can enable these inherently brittle ceramics to abrade away in a controlled manner and exhibit desirable performance. Wear mechanisms in ceramics are complex phenomena, and there currently exist multiple approaches to wear prediction and understanding, with indentation fracture mechanics and machining approaches being main strategies[80,81,94]. The applicability of these approaches is highly dependent on the conditions of loading, and it is not well understood which is applicable to a high temperature rub impact with the abrasive part moving at speeds up to 40,000 rpm.

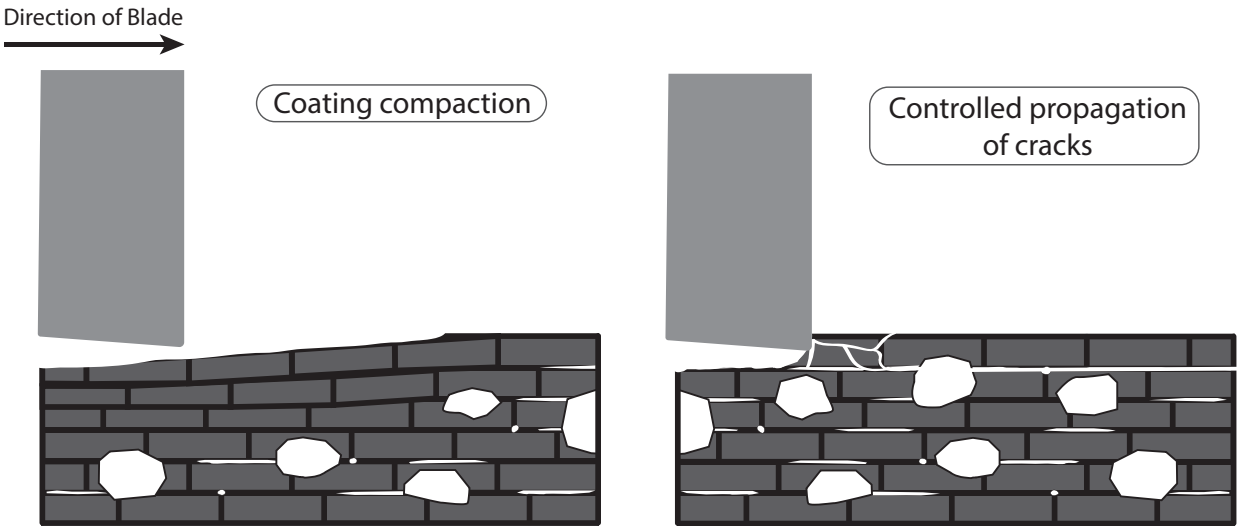

FIGURE 22. Potential favorable blade and coating interactions.

This work aims to provide insight by first connecting the damage accommodation mechanism to microstructural features existing in current technology abradable coatings. The expected favorable damage mechanisms are illustrated in Figure 22. This study will examine the role of different microstructural features, and their evolution with aging in low and high water vapor environments, in the damage accommodation mechanics of ceramic abradable coatings by looking at two commercially available ceramic abradable coating systems. The coating systems to be studied are dysprosia- or yttria- stabilized zirconia with varying fractions of pore former and secondary phases. Figure 23 shows a schematic representation of the two different microstructural features present in the YSZP vs. DySZPB APS coatings. These systems were chosen based on a holistic look at the abradable coating and abrasive material acting as a system. Most other ceramic abradable coatings, such as Ebert, et al's magnesium spinel and YSZ dual layer coating [70] or Bucci, et al's [29] YSZ DVC coating with a patterned surface, that have been proposed typically require blade tipping with abrasive materials, such as silicon carbide or cubic boron nitride. The application of these ultrahard materials to blade tips is expensive, and

they have limited longevity in the turbine due to the propensity of carbides and nitrides to undergo oxidation and volatilization reactions under turbine operating conditions[24]. The proposed material systems to be tested in this work have shown good abradable performance without abrasive blade tipping under certain rub impact conditions.

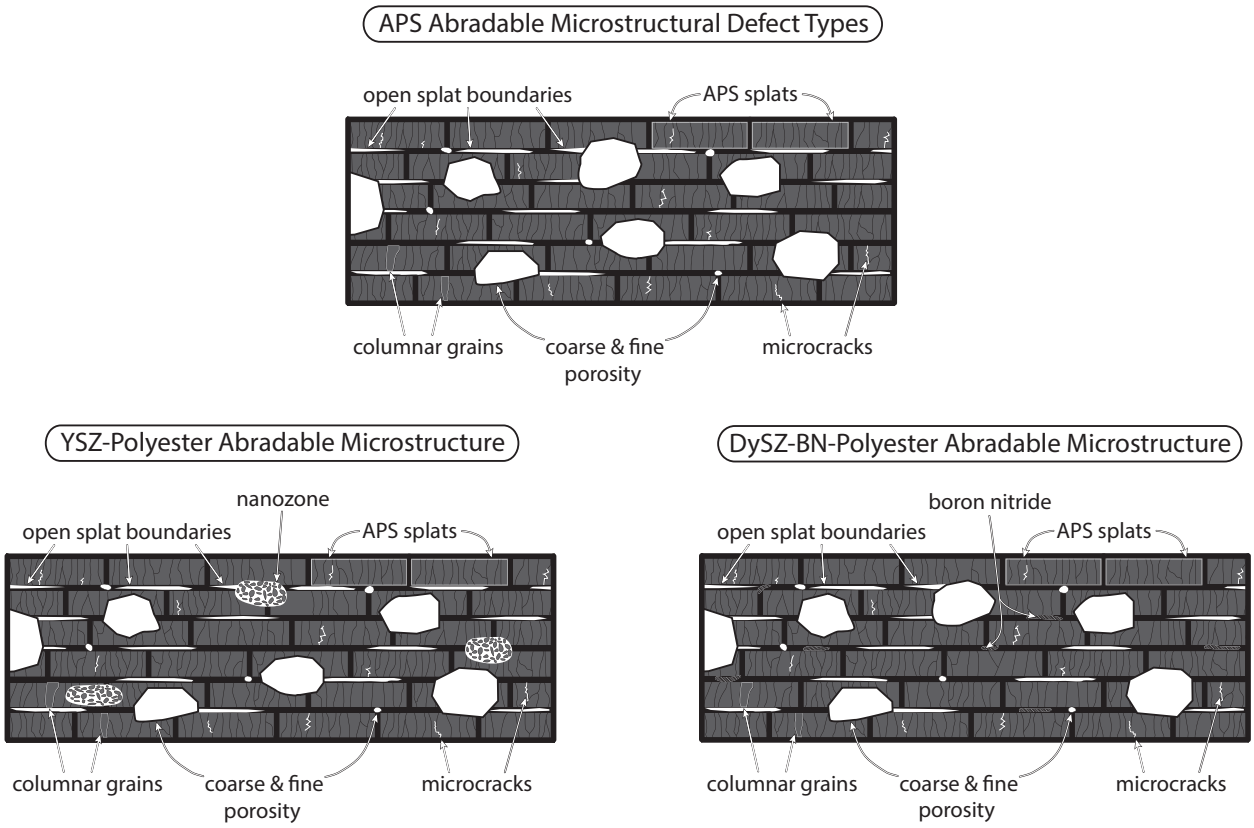

FIGURE 23. Schematic representation of microstructural features existing in the YSZ-polyester system and DySZ-BN-polyester system as compared to typical APS microstructural features.

To develop an understanding of microstructural and material affects on wear behavior, bulk materials will be studied as well as free-standing air plasma sprayed (APS) coatings. The damage mechanics of as received as well as aged materials will be tested using a macroscratch test with characterization of the damage zone post testing giving insight into how the microstructure affects the mechanisms by which these materials accommodate rub interactions. Simplifications have been made since the lab-scale macroscratch test is unable to

simulate the extreme rub impact speeds seen in a turbine, but instead, will probe the ability of the material to accommodate a highly tangential force at lower strain rates. The testing is also done at room temperature, and thus does not capture the effects of any high temperature plasticity or softening of the ceramic materials in service. The aim of this work is to determine the influence of different microstructural features present in current technology ceramic abradable coatings on the preferred wear behavior of these systems to guide future designs. It is expected that the presence of different microstructural features will change the damage accommodation mechanism seen in the abradable system. Links between different defects, their evolution with aging, and observed wear behavior will be compared.

4.2 Experimental Methods

4.2.1 Materials and Processing

Two commercially available APS ceramic abradable systems were studied. The first was a dysprosia stabilized zirconia (DySZ), polymer, hBN system (further referred to as DySZPB). The second was a YSZ, polymer abradable system. DySZPB coatings were processed by air plasma spray at two different suppliers, Plasma Technology Incorporated (Torrance, CA, USA) and Solar Turbines Incorporated (San Diego, CA, USA), using Durabrade 2192 spray dried powders purchased from Oerlikon Metco US Inc. (Brea, CA, USA). These coatings are further referred to as DySZPB (processed by PlasmaTech.) or DySZPB_ST (processed by Solar Turbines). The APS YSZ, polymer system was sprayed by both suppliers as well using Metco 2460NS spray dried powders also purchased from Oerlikon Metco. The 2460NS coatings are further referred to as YSZP (processed by PlasmaTech.) or YSZP_ST (processed by Solar Turbines). Powder specifications are listed previously in Table I of Chapter 2. Two important

differences to note in the starting powders are different starting powder morphologies and lower percentage of dysprosia stabilizer by mole percentage used in the DySZPB coatings.

Two bulk material compositions, YSZ and a YSZ-hBN composite, were also processed to study the matrix material behavior without the additional defects inherent to the APS process. Tetragonal 4 mol% YSZ (4YSZ) samples were made using Tosoh Corporation (Tokyo, Japan) TZ-4Y powders (>99.8% purity, 40nm particle size). Both tetragonal (t) and the metastable phase, tetragonal prime (t'), bulk YSZ materials were processed. The tetragonal, t 4YSZ, was made by first pressing the powders at 7 tonnes for 5 minutes. It was then sintered in air at 1250˚C for 18 hours with a 10˚C/min. heating and cooling rate using a CM Furnaces Inc. (Bloomfield, NJ, USA) 1700C tube furnace with a mullite tube.

The t' 4YSZ samples were processed using spark plasma sintering (SPS) with a Fuji SPS 825-S (Fuji Electronic Industrial Co. Ltd., Saitama, Japan). For SPS, the 4YSZ powders were first weighed and loaded into 18 mm diameter graphite dies with 2 sheets of graphite foil. SPS parameters of 100˚C/minute heating rate, 65 MPa pressure, 1600˚C sintering temperature, 10 minute hold time, and 200-300˚C cooling rate were used. The temperature of the sample was monitored using an optical pyrometer, and the cooling rate was reached by shutting off the instrument and letting the sample cool to ambient temperature. The graphite foils on the SPS sintered samples were then ground off, and the samples were annealed in air at 900˚C for 8 hours with a 2˚C/minute heating rate and 10˚C/minute cooling rate.

In addition, a composite of the same Tosoh 4YSZ powders and 25 vol. % hBN (99.5% pure by metals basis, product #11078, Alfa Aesar by Thermo Fisher Scientific, Tewksbury, MA, USA) was processed by first ball milling the powders in ethanol using 5 mm diameter zirconia

milling media. The ball mill was run at 40 rpm for 12 hours. The milled powders were then dried and ground using a mortar and pestle. Polyvinyl alcohol (PVA) was added as a binder to the 4YSZ-hBN composite powders prior to pressing to assist homogeneous compaction of these powders into green bodies. PVA at 3 vol. % was added to the 4YSZ-hBN powders by first dissolving the PVA binder in distilled water at 80˚C. The 4YSZ-hBN powders were then added with continuous stirring. The PVA, 4YSZ, hBN powders were dried at 110˚C overnight then ground with a mortar and pestle. Green bodies of each composition were then pressed and heat treated at 450˚C for 8 hours with a 5˚C/min. ramp rate to remove the polymer. The 4YSZ-hBN composite was then sintered in nitrogen at 1365˚C for 12.5 hours with a 10˚C/min. heating and cooling rate.

4.2.2 Sample Preparation and Characterization

Coating samples were prepared for characterization and testing by first polishing off any underlying substrate and bond coat material on the APS coatings to make free-standing coatings. The as received coatings, which were around 760 μm thick, were then heat treated to remove the polymer pore former at 450˚C for 8 hours with a 5˚C/minute ramp rate as suggested by the powder manufacturer. Both the coatings as well as bulk material samples were then cut using a high-speed diamond blade, mounted in epoxy, and polished to a 0.25 μm finish.

Polished samples were coated with iridium or carbon to prepare for scanning electron microscopy (SEM) imaging in a FEI Company (Hillsboro, Oregon, USA) Magellan Field Emission Gun SEM to determine the microstructure of the samples. ImageJ analysis software (US National Institute of Health, Bethesda, MD USA) was used to analyze the area fraction of the porosity and secondary phase. Rough polished samples were used for Raman spectroscopy

with a 532 nm laser on a Renishaw (Wotton-under-Edge, UK) inVia Raman Microscope to analyze the hBN phase (< 1 wt. %) in the coatings. Powder x-ray diffraction (XRD) was performed on a Rigaku Corporation (The Woodlands, TX, USA) Ultima III X-ray Diffractometer with a Cu k-alpha source, 1.54 Å wavelength to confirm the t' phase and to analyze the hBN phase in the bulk materials.

4.2.3 Testing

In addition to characterization and testing of as-processed materials, aging experiments were carried out on the free-standing APS coatings to replicate microstructural changes seen with increasing operational time in the turbine. Aging experiments were completed using a high temperature, controlled atmosphere tube furnace. To test in a representative natural gas fired turbine combustion stream, 9.5% H_2O (v) by partial pressure in a mixture of nitrogen and oxygen gas at a ratio of 80:20 and a flow rate of 80sccm were flowed across the sample surface for aging experiments. To test in a representative synthetic gas fired turbine combustion stream, 30% H_2O (v) by partial pressure in a mixture of nitrogen and oxygen gas at the same ratio and flow rate as above were used during aging experiments[2]. Aging was performed at 1100˚C with a 10˚C/min. ramp rate for hold times up to 145 hours. The tube furnace system was purged in the wet environment for two residence cycles at 150˚C prior to exposure.

After polishing epoxy mounted sample surfaces, both as-processed bulk and coating materials, as well as aged coatings, were heat treated in air at 700˚C for 1 hour with a ramp rate of 3˚C/min. to burn out the epoxy prior to Vicker's hardness testing. The unpolished side of the samples was planarized to ensure the samples for indentation were flat. Samples were then mounted using a minimal amount of crystal bond to a steel plate with planar faces in preparation

for Vicker's indentation. At least five indents were made with a diamond Vicker's indenter tip at 1 kg-f with a 60 second hold. Indents were placed away from any coarse porosity present on the surface. The diagonal lengths, d, of the indent were then measured using an optical microscope and recorded to calculate the Vicker's hardness according to Equation 3 (shown in Ch. 2) where P is load.

4.2.4 Preliminary Nanoindenter Scratch Testing

An Agilent Technologies G200 Nano Indenter was used with a diamond conical tip made by MicroStar Technologies (Huntsville, TX USA) with a 5 +/- 1 μm radius and 120 +/- 5˚ angle, as illustrated in Figure 12 (Ch. 2). Single pass, ramp load scratch tests were performed on polished samples using the procedure outlined in the G200 Manual supplied by the manufacturer with the XP indenter head designed for use with stiffer materials. First, a profile of the surface was measured at low load, 50μN in these experiments, to map the original morphology of the surface. Next, along the same track, the normal load was gradually increased from 0 mN to a maximum load of 400 mN with parameters outlined below in Table III (Ch. 2). Lastly, the scratch profile was measured by another pass at low load, 50μN, to map the topography of the scratch profile.

4.2.5 Macroscratch Testing and Analysis

Macro-scale single pass scratch tests were performed at a constant 1 kg-f load with a standard Vicker's indenter. The surfaces of samples for this macroscratch test were prepared in the same manner as samples for Vicker's indentation, and samples without epoxy were tested. During the test, an indent was made with a 1 kg-f load and held constant at maximum indent depth for 60 s during which a scratch was made across the surface approximately 3-5 mm long.

The horizontal motion was manually controlled by a micrometer with approximate speed around 50-100 μm/s. At least two scratches were performed on each material. A Polytec Inc. (Irvine, CA, USA) MSA-500 Micro System Analyzer (vibrometer) was used to map the surface topography of the sample after mechanical testing. Measurement for optical vibrometry was done using a 10x Nikon Mirau lens at the smallest step size of 89nm and preset parameters for either 'smooth with step' or 'rough' surfaces, depending on the surface characteristics of the polished samples. Post processing was used on the topographical images to reduce noise by taking the signal average of 5 pixels.

The damage zones beneath the scratches were of interest to understand how the microstructure beneath the scratch changed after damage. This damage zone was investigated by cross sectional analysis using SEM. Samples were prepared after scratch testing by first marking the scratch positions, which were visible by eye, with permanent marker. The sample cross sections were then mounted in epoxy in preparation for polishing. During the first rough polishing step, half the length of the scratch was removed so that the damage at the midpoint could be analyzed.

4.3 Results

4.3.1 As Received SEM and Characterization

Figure 24 shows the as received microstructures of the bulk t YSZ, t' YSZ (fracture surface), and YSZ-hBN samples. Bulk t and t' YSZ as well as YSZ-hBN are >98% dense with >1μm grain sizes, and the composite contains the expected 30 vol. % of hBN, confirmed by image analysis and x-ray diffraction, shown in Figure 25. It is evident that in addition to the tetragonal YSZ and hBN phases, there is also an additional oxidized zirconium boride phase,

shown in literature with high pressure synthesis[95,96]. The t' phase in the 4YSZ processed by SPS was confirmed using XRD, as shown in Figure 26.

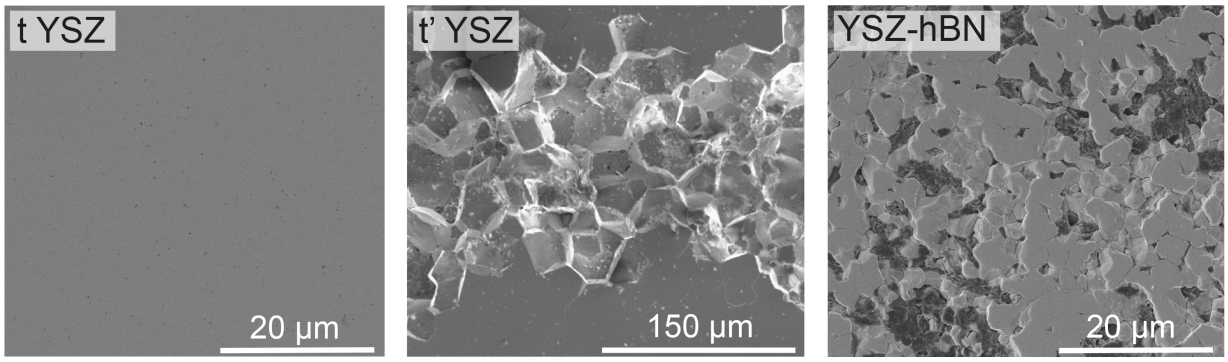

FIGURE 24. SEM images of bulk t YSZ, t' YSZ, and t YSZ-hBN materials.

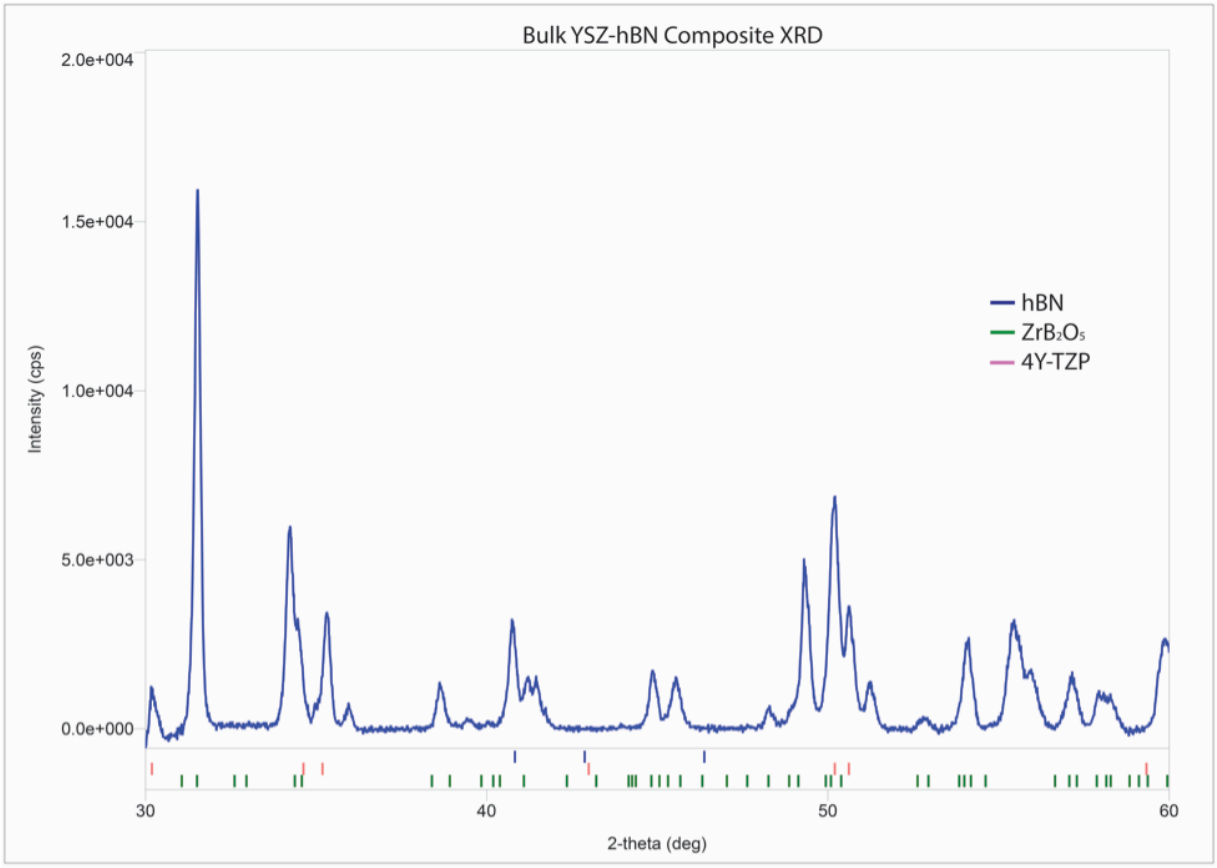

FIGURE 25. XRD of YSZ-hBN bulk material showing the presence of t 4YSZ, hBN, and an additional oxidized zirconium boride phase.

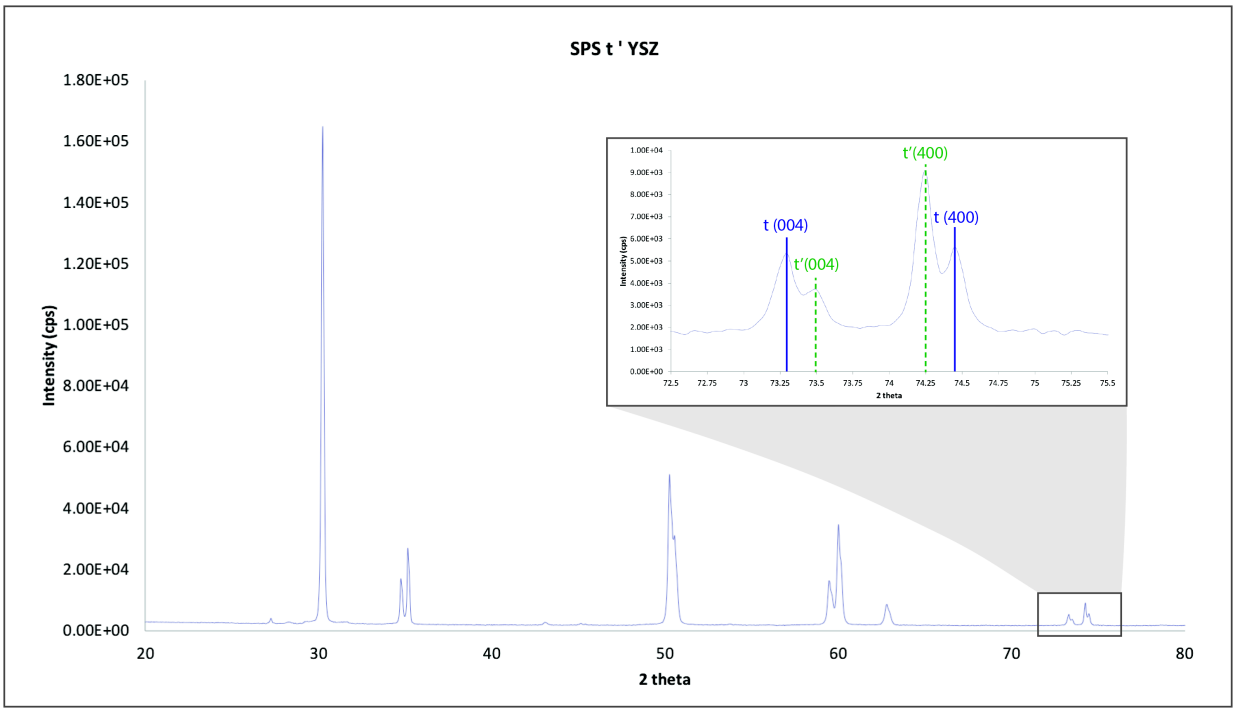

FIGURE 26. XRD showing an inset from two theta: 72-74 degrees confirming the presence of the metastable t' phase in the SPS processed bulk YSZ.

Figure 27 shows the YSZP and DySZPB APS coating materials processed by both suppliers. The APS coatings, YSZP_ST and DySZPB, have 34% and 27% porosity, respectively, which was analyzed by area fraction. The DySZPB_ST coating contained a much lower porosity percentage at 12%, and the YSZP coating showed inhomogeneous distribution of porosity through the thickness, evident in the denser surface of the coating shown in Figure 27, of YSZP. Because the porosity distribution and percentage was most similar in the YSZP_ST and DySZPB coatings, this study will focus on those systems.

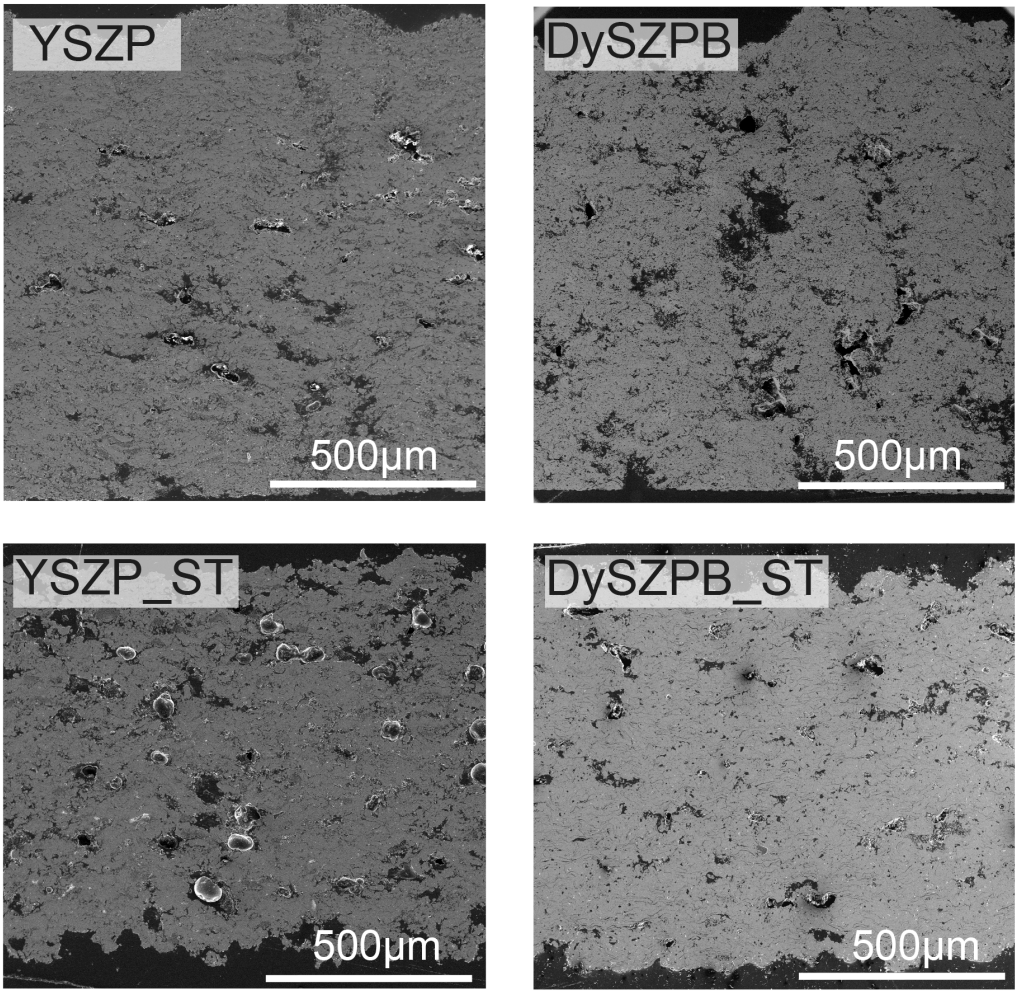

FIGURE 27. SEM images of the as-processed coating materials with coatings processed by PlasmaTech. shown on top and Solar Turbines on the bottom.

Upon closer SEM examination of the YSZP coatings, the presence of 'nanozone' features is evident in both YSZP coatings, as shown in Figure 28. These nanozones are created during the spray process as partially unmolten particles remain after being sprayed onto the surface. YSZ coatings with nanozones are well documented in the literature when using nano-agglomerated spray dried powders[67,69]. The YSZP_ST coatings contain around 8% nanozones by area.

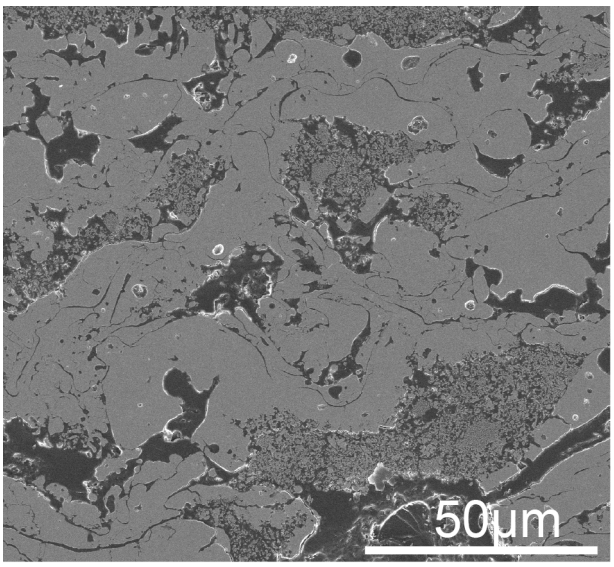

FIGURE 28. SEM image showing the presence of nanozone features in the YSZP_ST coating.

Raman spectroscopy was used on the DySZPB coatings in order to verify the structure of the BN phase in the as-processed state. Figure 29 shows the Raman spectra of the Durabrade 2192 powders and the processed coating with the absence of the characteristic E_{2g} peak for hBN in the APS coating[49]. Further examination was done by Raman spectroscopy on the DySZPB_ST coating processed by a different supplier than DySZPB, confirming the absence of the peak at 1367 cm^{-1}. The DySZPB coatings were also investigated by transmission electron microscopy, which showed the presence of an amorphous form of BN as seen in Figure 30. Raman spectroscopy of aged DySZPB coatings also showed an absence of the hBN peak. X-ray photoelectron spectroscopy was additionally performed, confirming the presence of the boron-containing phase (shown in Appendix B). However, the low percentage of the BN phase present as well as tight positions of the B_2O_3 and hBN peaks left the exact chemical state of the amorphous boron-containing phase yet to be determined.

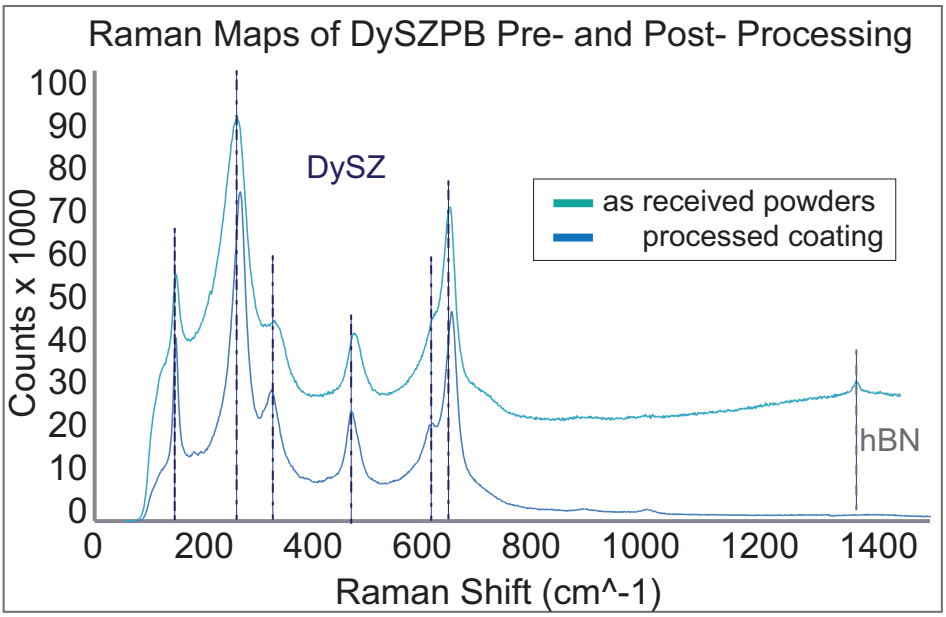

FIGURE 29. Raman spectrum representative of the as-processed DySZPB coating (aged for 50 hrs. shown for example) as compared to the as received DySZPB powders.

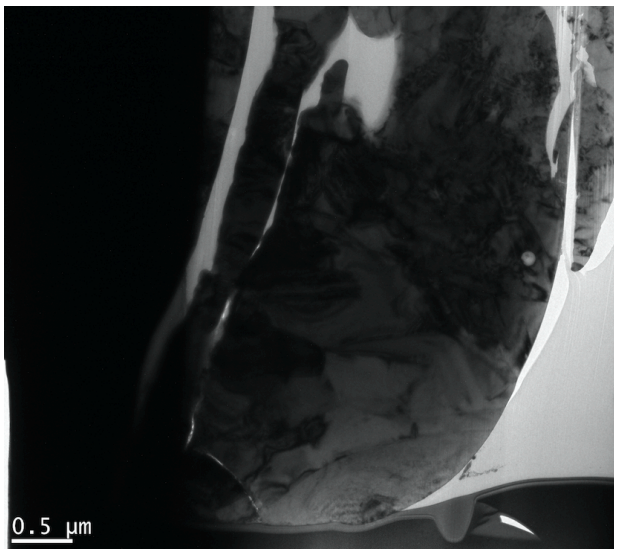

FIGURE 30. TEM image of the amorphous area of BN found in the DySZPB coatings.

4.3.2 Aging Studies

Figures 31 and 32 show SEM micrographs of the evolution of the APS coatings under simulated natural gas, 9.5% H_2O (v), and synthetic gas, 30% H_2O (v), turbine combustion atmospheres. With increasingly longer exposures at both low and high water vapor contents, the

YSZP_ST and DySZPB coatings both undergo densification leading to a decrease in concentration of open APS splat boundaries. It is particularly evident in the DySZPB coatings, shown in Figure 31, with extensive closing of the open splat boundaries seen in the SEM micrographs starting at the lowest exposure time of 10 hours. The YSZP_ST coatings, on the other hand, don't show the same extent of open splat boundary closing, but do show evidence of sintering. Figure 33 shows a comparison of the YSZP_ST and DySZPB coatings exposed for 145 hours in high water vapor at higher magnification to illustrate the difference in the extent of sintering between the two coatings.

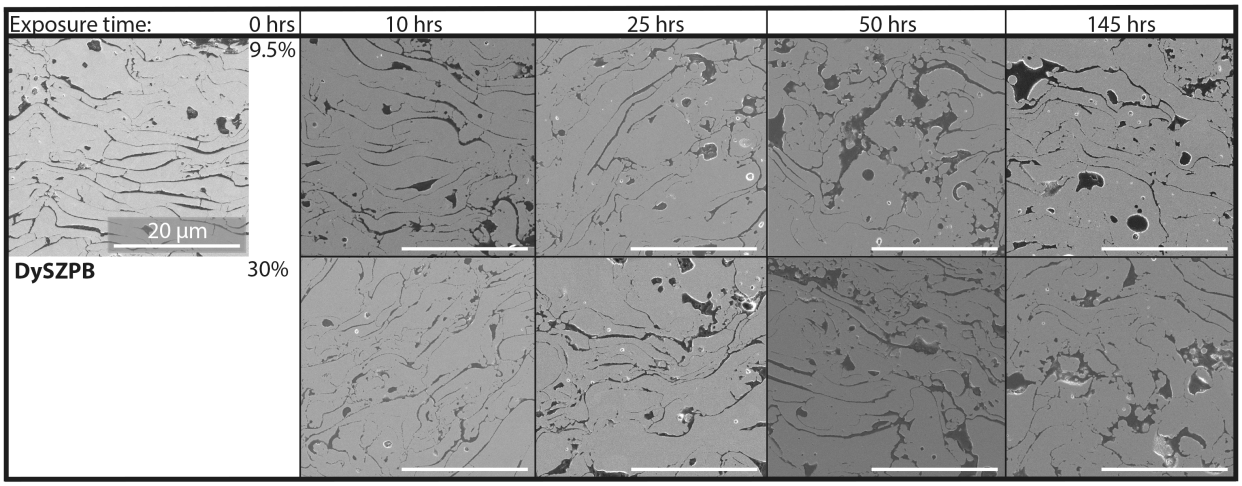

FIGURE 31. SEM images showing the progression of the microstructures of the DySZPB coatings with aging.

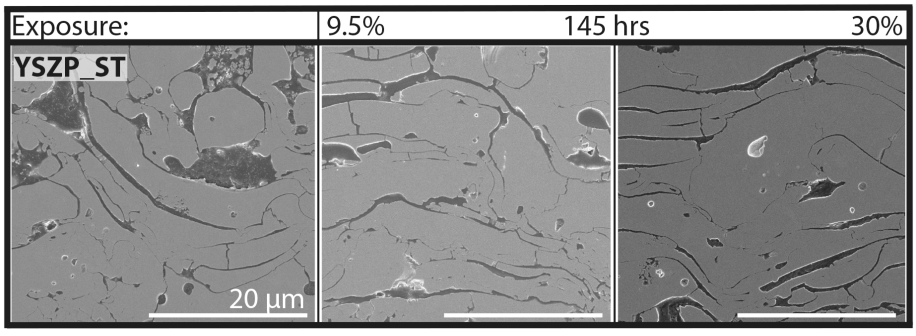

FIGURE 32. SEM images showing the progression of the microstructures of the YSZP_ST coatings with aging at 145 hours.

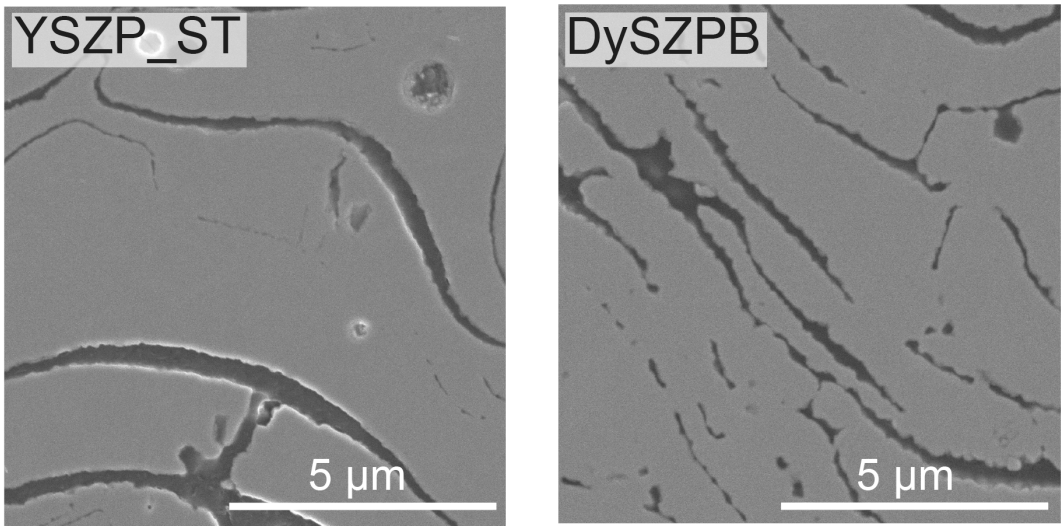

FIGURE 33. SEM of YSZP and DySZPB coatings exposed at 9.5% water vapor for 145 hrs. showing the further extent of sintering seen in the DySZPB coatings at higher magnification.

Image analysis with lower magnification images of the overall porosity percentage, including coarse, fine, and intrasplat porosity, in the YSZP_ST coatings at 9.5% H_2O (v) changes from 34.4 +/- 1.8% in the as received to 32.5 +/- 1.6% for the 145 hour exposure. The total porosity in the DySZPB coatings at 9.5% H_2O (v) changes from 27.1 +/- 2.6% for the as received to 25.4 +/- 2.9% for the 145 hour exposure. There is no significant change in the YSZP_ST overall porosity percentage in higher water vapor versus low at 145 hour exposure, but the DySZPB coatings show an increase in overall porosity percentage to 31.6 +/- 2.5% in high water vapor at 145 hours. This increase in porosity seen in DySZPB from low to high water vapor is due to the oxidation, volatilization reaction of BN being enhanced in a higher water vapor environment and overshadowing the reduction of porosity expected with sintering. The expected reactions of the BN would proceed according to the following reactions[3].

$$4\ BN\ (s) + 3\ O_2\ (g) \rightarrow 2\ B_2O_3\ (l) + 2\ N_2\ (g)$$

$$B_2O_3\ (l) + H_2O\ (g) \rightarrow BOOH\ (g),\ B(OH)_3\ (g),\ (BOOH)_3\ (g)$$

Figure 34 shows SEM images of fracture surfaces of the DySZPB coatings, which gives insight into the densification mechanism, before and after exposure. In the micrographs looking at the low versus high water vapor aging experiments for each material, similar extents of intrasplat boundary removal are seen with no significant differences between the two at the same exposure time seen with the aging times used in this study. This intrasplat boundary removal occurs first by surface diffusion coarsening the intercolumnar grains within a splat. These coarsened grains then act as bridges across the APS splats thereby filling in the open splat boundaries. Densification of APS TBC materials by this bridging mechanism enabled by surface diffusion and further bulk diffusion above ~1000˚C has been well documented in the literature[92,97].

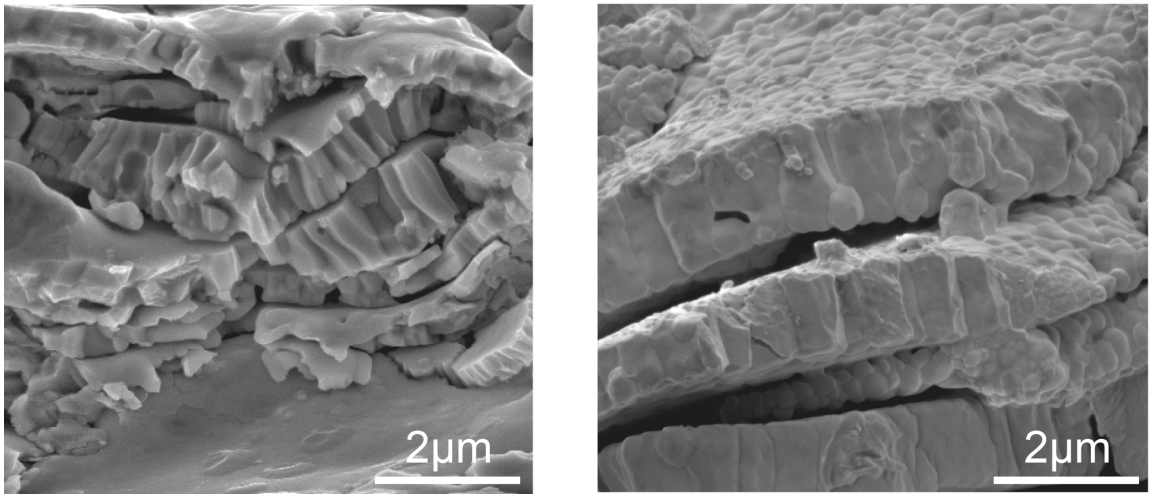

FIGURE 34. Fracture surface SEM images of as-processed and aged DySZPB (70 hrs. shown).

4.3.3 Mechanical Testing and Evaluation

4.3.3.1 Hardness

Bulk and APS coating materials were tested for hardness using Vicker's indentation with both as received and exposed coatings being tested. Figure 35 shows the hardness of bulk t YSZ, t' YSZ, and the YSZ-hBN composite. The hardness of the composite is significantly lower than that of the bulk YSZ samples due to the hBN phase. Figure 36 shows the hardness of the APS coatings as compared to a standard 7 wt. % YSZ TBC processed by APS for reference. With 145 hours of exposure to 1100˚C and 9.5% H_2O (v), the hardness of the DySZPB coatings increases to twice that of the as received coating while the YSZP abradable sees a negligible increase in hardness with aging.

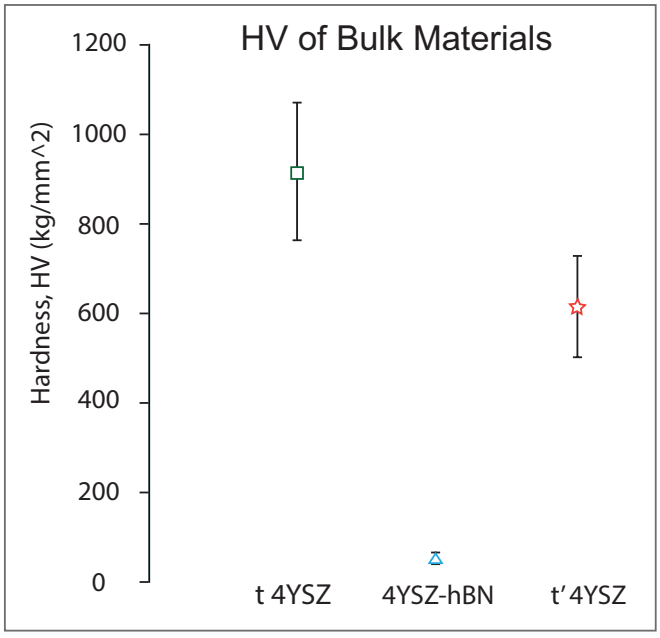

FIGURE 35. Vicker's hardness compared for the bulk t YSZ, t' YSZ, and YSZ-hBN composite.

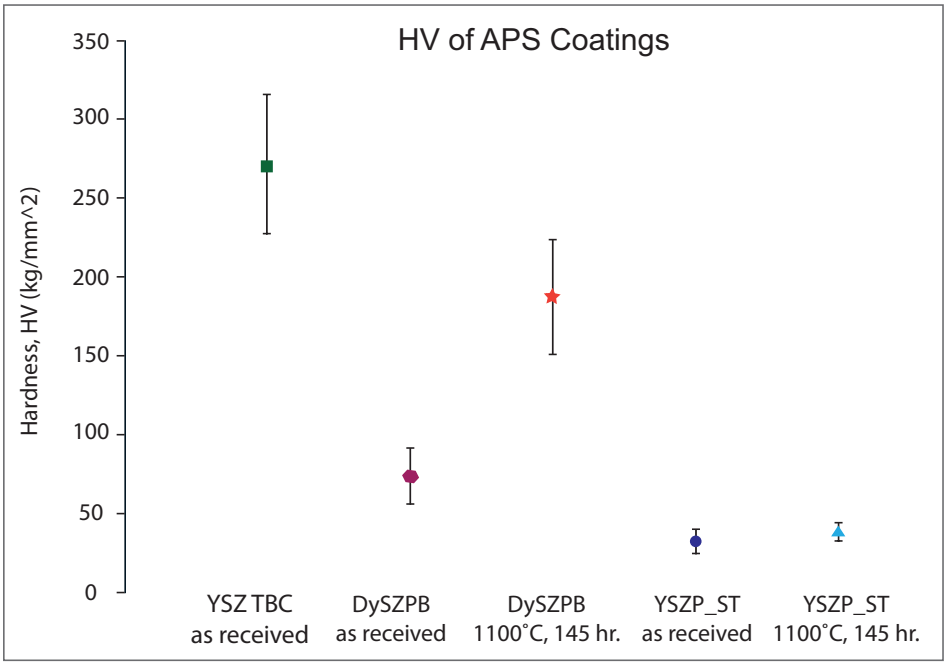

FIGURE 36. Vicker's hardness of as-processed and aged coatings as compared to a standard 4YSZ APS TBC.

4.3.3.2 Nanoindenter Scratch Tests

Figure 37 shows representative progressive load scratches of as received DySZPB and YSZP_ST coatings performed by the nanoindenter. With progressive loading, wear mechanism transitions were expected along the length with the changes going from plowing to powder formation to flake formation with increasing contact pressure[94]. Figure 38 illustrates the microcracking seen in the YSZP_ST scratch track where plowing has occurred. However, the characteristics along the length of the scratch tracks of both coating systems are variable, changing from plowing to extensive lateral fracture and flake formation then back to plowing. With SEM investigation, these multiple transitions did not correspond to any particular microstructural feature in the coating and was not consistent between several different scratches performed on the same material. The extent of indent depth and size variation in these regions along a scratch track is illustrated in Figure 39, and a 3D topography map from the optical

vibrometer is shown in Figure 39 illustrating the extent of piled up material along the edges of the scratch track.

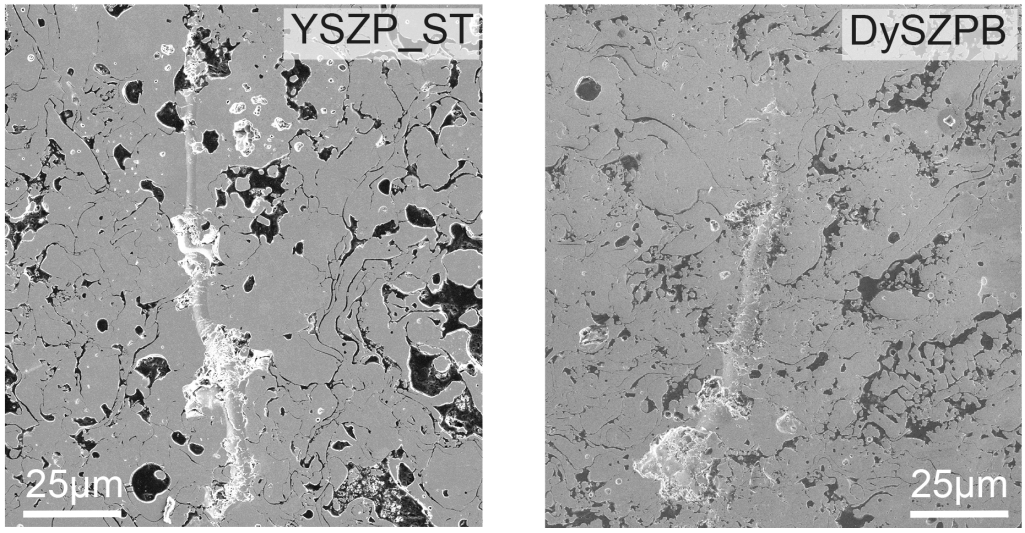

FIGURE 37. SEM images of the as-processed APS coatings scratched with the nanoindenter.

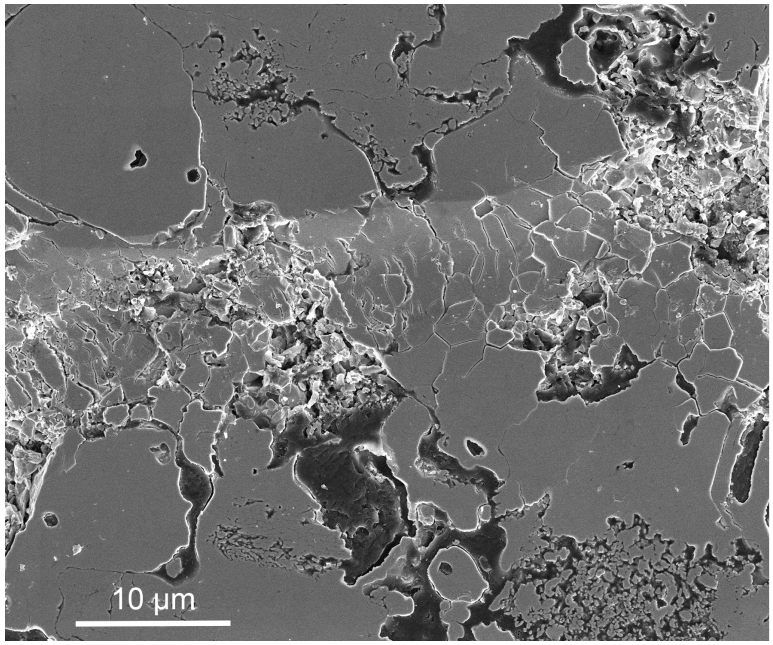

FIGURE 38. SEM image of the nanoindenter scratch track of the as-processed YSZP_ST1q showing surface and radial cracking.

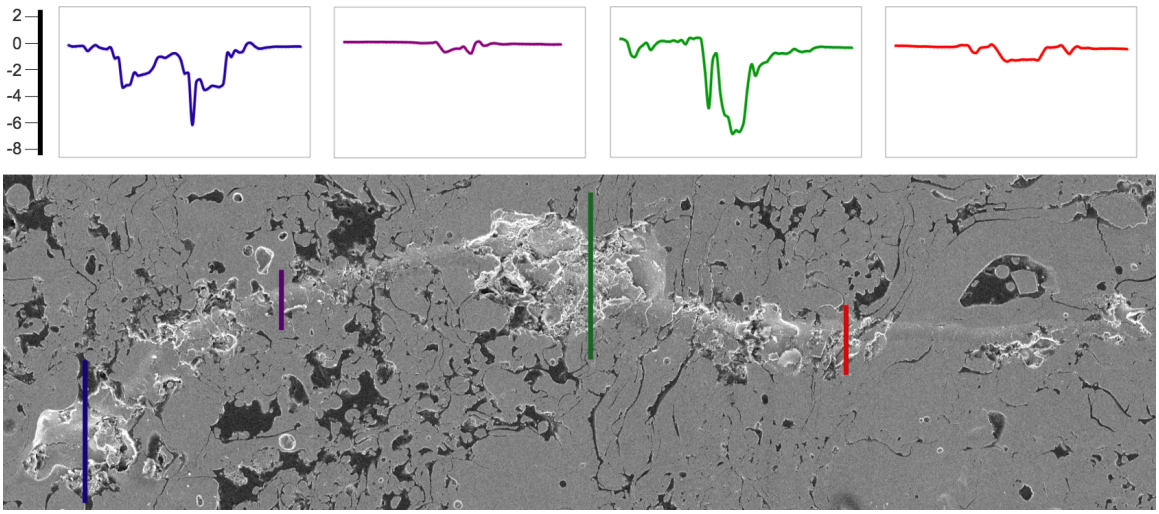

FIGURE 39. SEM image and measurements of the scratch track by optical vibrometer showing the as-processed nanoindenter scratched DySZPB coating.

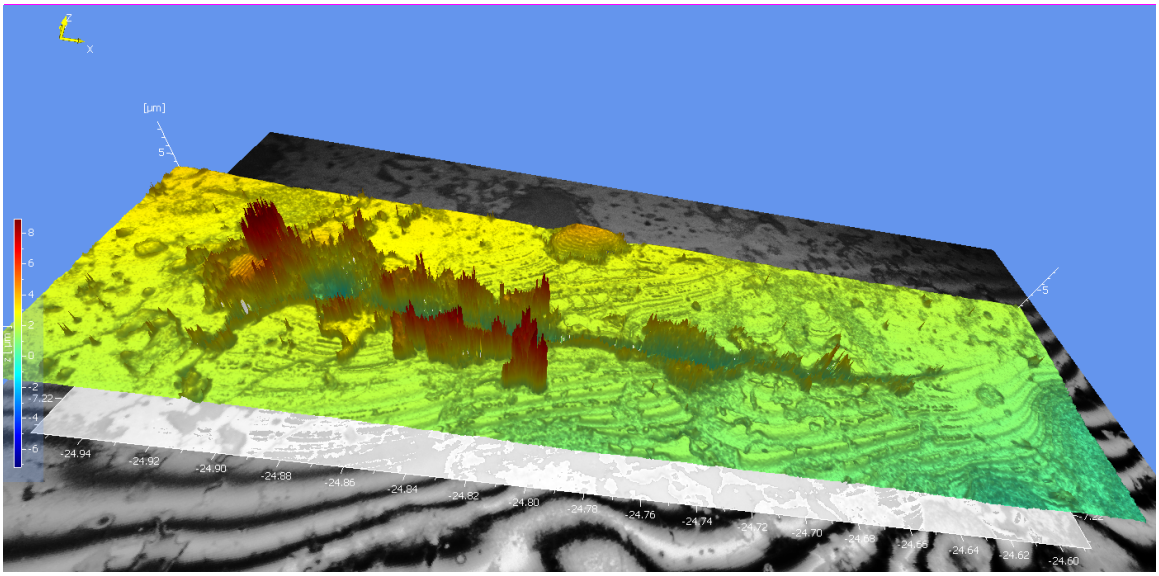

FIGURE 40. 3D optical vibrometer image of the YSZP_ST coating aged for 145 hrs. at 30% H_2O (v) showing material pileup along the edges of the scratch track made by progressive loading with the nanoindenter tip.

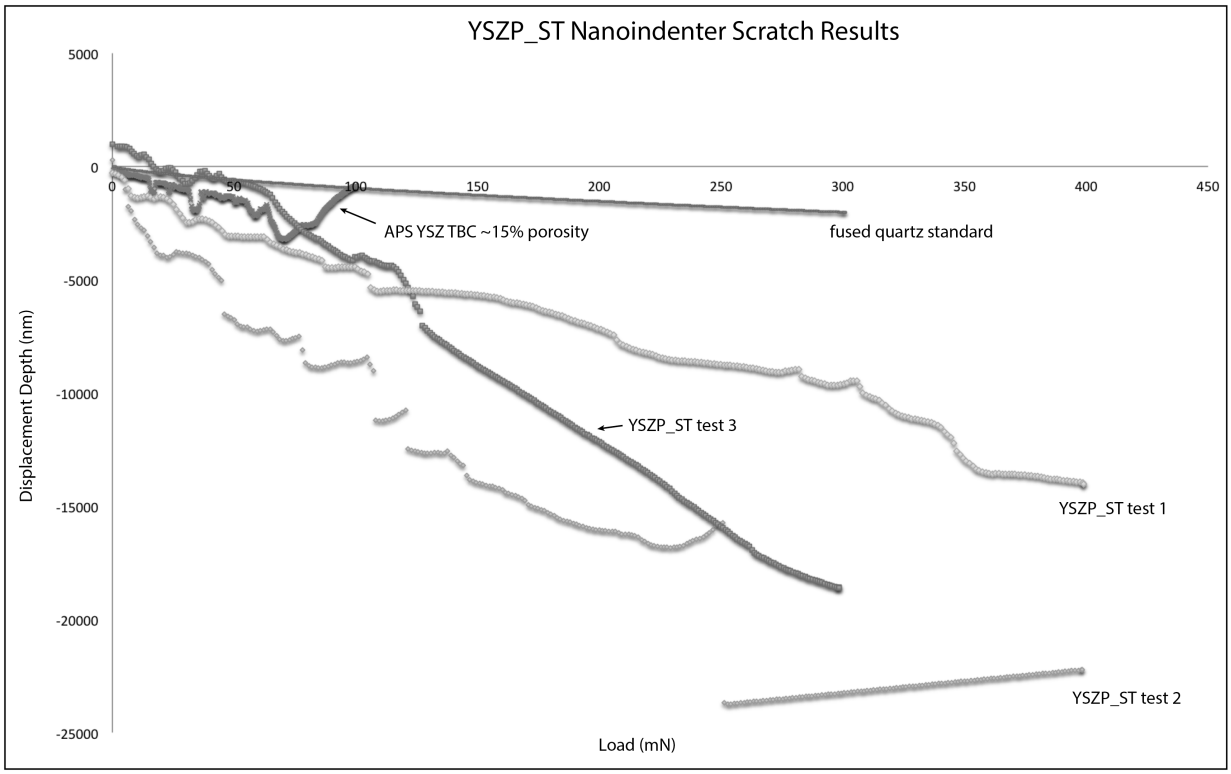

FIGURE 41. Raw data from the nanoindenter scratch test showing inconsistent measurements of the APS coatings.

Figure 41 shows data for several YSZ-based APS coatings with change in displacement of the indenter tip into the coating as load is increased. Three scratch tests are shown on the YSZP_ST coating with test2 appearing to have a sudden increase in displacement with loads > ~250mN. This behavior was seen in multiple other tests on YSZP_ST as well as DySZPB coatings. Upon further SEM investigation of the scratch tracks exhibiting this behavior, it was evident that the indenter tip did not follow a straight path as it was applying load to the sample. Figure 42 shows a scratch track representative of this behavior. It is expected that the stochastic nature of the APS coatings, the size of the indenter tip not being sufficiently larger than the APS microstructural features, as well as sensitivity of the instrument tip resulted in faulty scratch tests. There were no repeatable results in the coatings due to the fact that the scratch tracks were not straight and that the load was reduced by the machine as a safety mechanism when the

indenter tip saw too much resistance from the material or lateral deflection during testing. First using a larger size indenter tip was investigated, but the Agilent G200 system in use had a maximum load of 500mN, and the associated pressure applied with a larger indenter tip would not have been sufficient enough to probe a depth larger than 1-2 splat length scales in the coating material. Thus, further testing was explored to accurately test the behavior of the coating materials and is discussed in the next section.

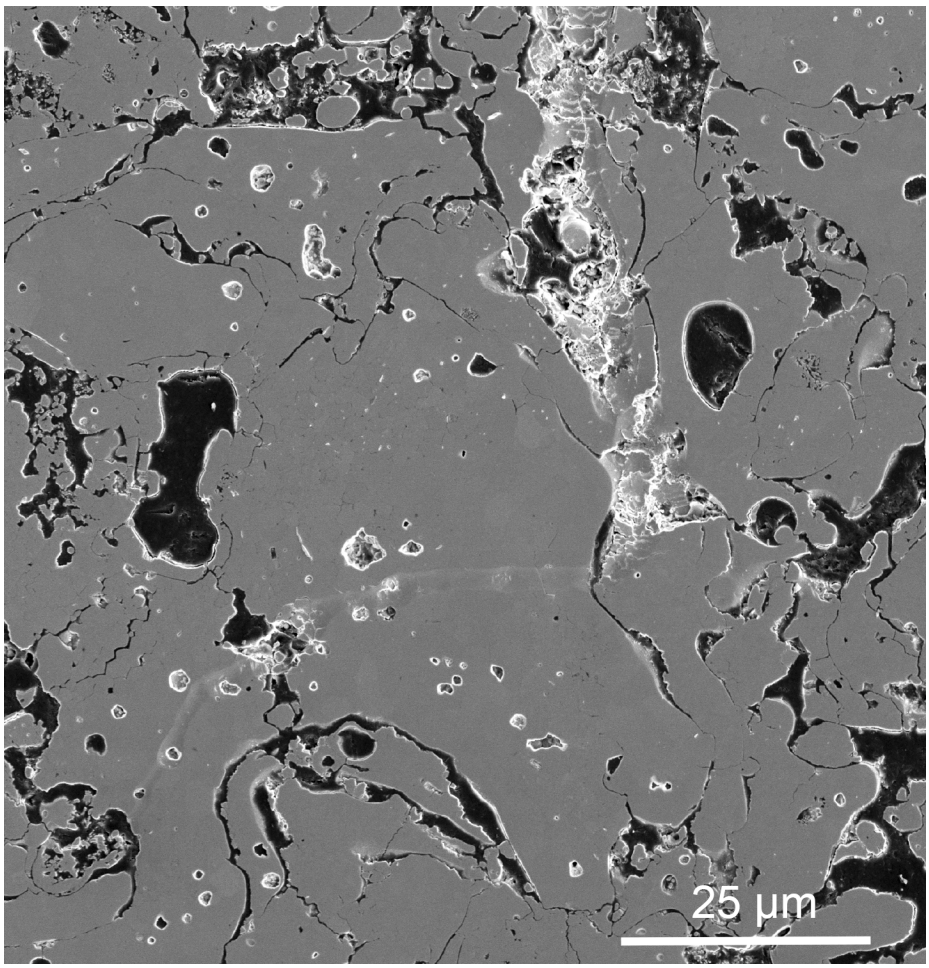

FIGURE 42. SEM image of the as-processed YSZP_ST coating showing a highly tortuous scratch track.

4.3.3.3 Macroscratch Investigation of Bulk Materials

Figure 43 shows representative cross sectional SEM images of the tracks made by macroscratch testing the bulk materials. The damage in the bulk t YSZ material is shown through median and radial cracking. The YSZ-hBN composite however, does not show the same crack extension into the material and has a much larger scratch track than YSZ.

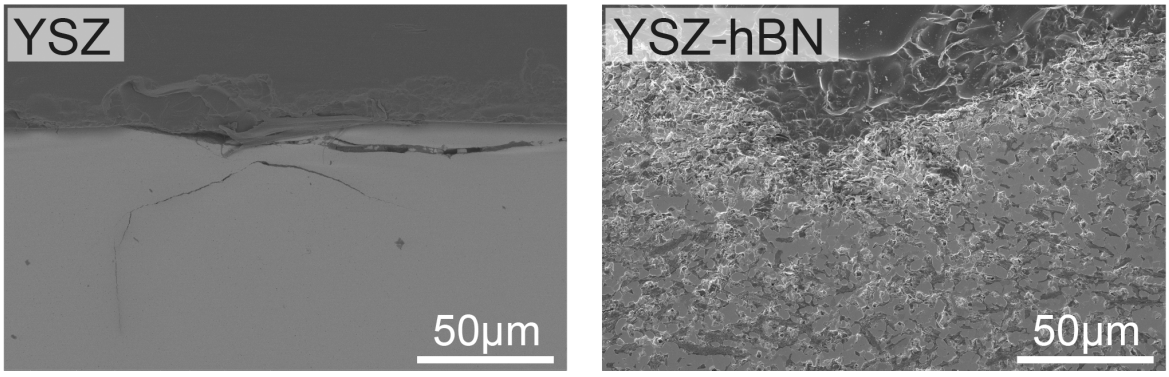

FIGURE 43. Cross sectional SEM images showing the damage zones of the bulk materials post macroscratch testing.

Figure 44 shows SEM images of the surfaces of the macroscratched t YSZ vs. t' YSZ bulk materials. It is evident in the t' YSZ that the scratch track was made by intergranular fracture, which is likely due to the SPS process at high temperatures and the corresponding large grain size. The same intergranular fracture was not observed in the t YSZ or YSZ-hBN bulk materials after macroscratch testing.

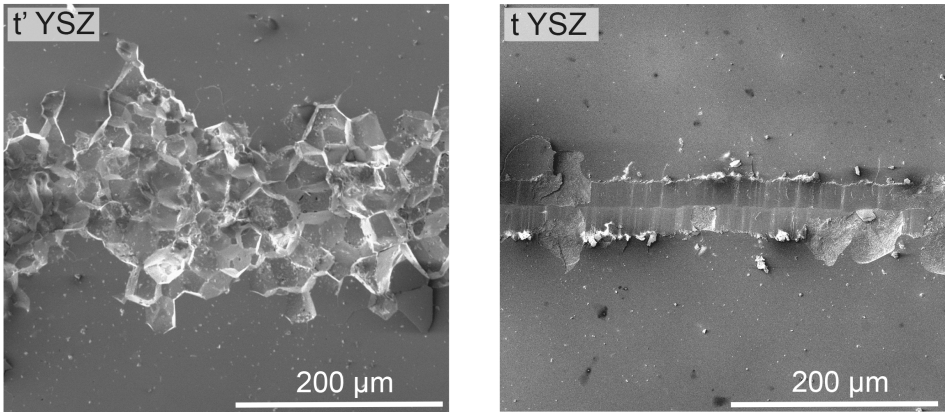

FIGURE 44. SEM image of the t and t' YSZ macroscratch tracks showing the highly transgranular fracture seen in the SPS processed t' YSZ.

Figures 45 and 46 show topographical maps of bulk YSZ and YSZ-hBN scratch surfaces measured by an optical vibrometer. Figure 45 shows the YSZ scratch track and dimensions of the track along the length. It is evident that along the scratch, there exists a main scratch trench as well as areas of chipping caused by the extension of lateral cracks to the surface. These chipped areas increase the area of the scratch track significantly, with the trenches being around 50µm in width and chipped areas over 200µm. The depth of the scratch track along the length also varies slightly but is mostly constant between 10-20µm.

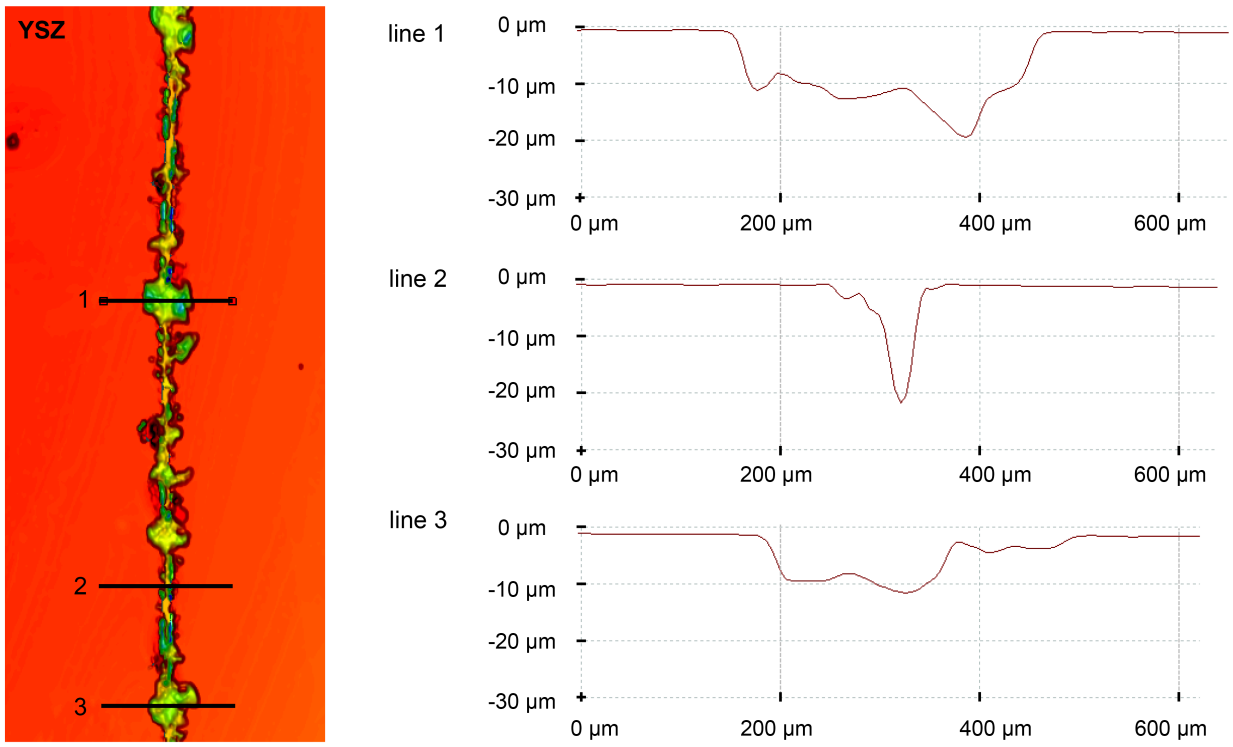

FIGURE 45. Optical vibrometer topography image and line scans for macroscratched bulk YSZ, taken with vibrometer preset surface parameter 'smooth with step'.

The scratch track for the bulk YSZ-hBN composite, shown in Figure 46, does not show chipping as seen in YSZ. The scratch maintains a width around 200µm and a depth of 35-45µm, larger than the YSZ due to the higher hardness of the bulk YSZ.

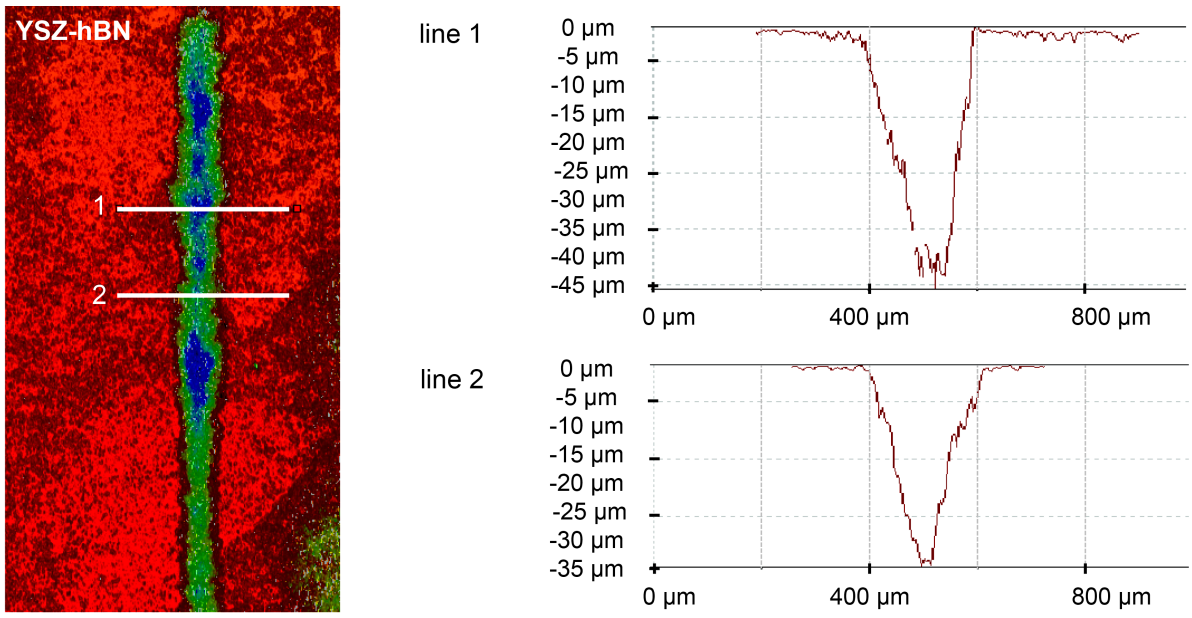

FIGURE 46. Optical vibrometer topography image and line scans for macroscratched bulk YSZ-hBN, taken with vibrometer preset surface parameter 'rough' due to the rougher surface in the composite from pullout during polishing.

4.3.3.4 Macroscratch Investigation of APS Coatings

Figures 47 and 48 show the optical vibrometer topographical maps of the scratch tracks for the as received YSZP and DySZPB abradable coatings. Both coating systems show similar trenches with chipping along the scratch track as seen in the bulk YSZ. Both systems also have significant changes in scratch track depths along the length likely due to the presence of coarse porosity in the coatings. The YSZP scratch depths vary from 50-120µm, while the DySZPB coatings vary in depth from around 15-70µm from the trench areas to the highly chipped sections. The YSZP scratch depths are larger than the DySZPB coatings due to the YSZP coatings having a lower hardness.

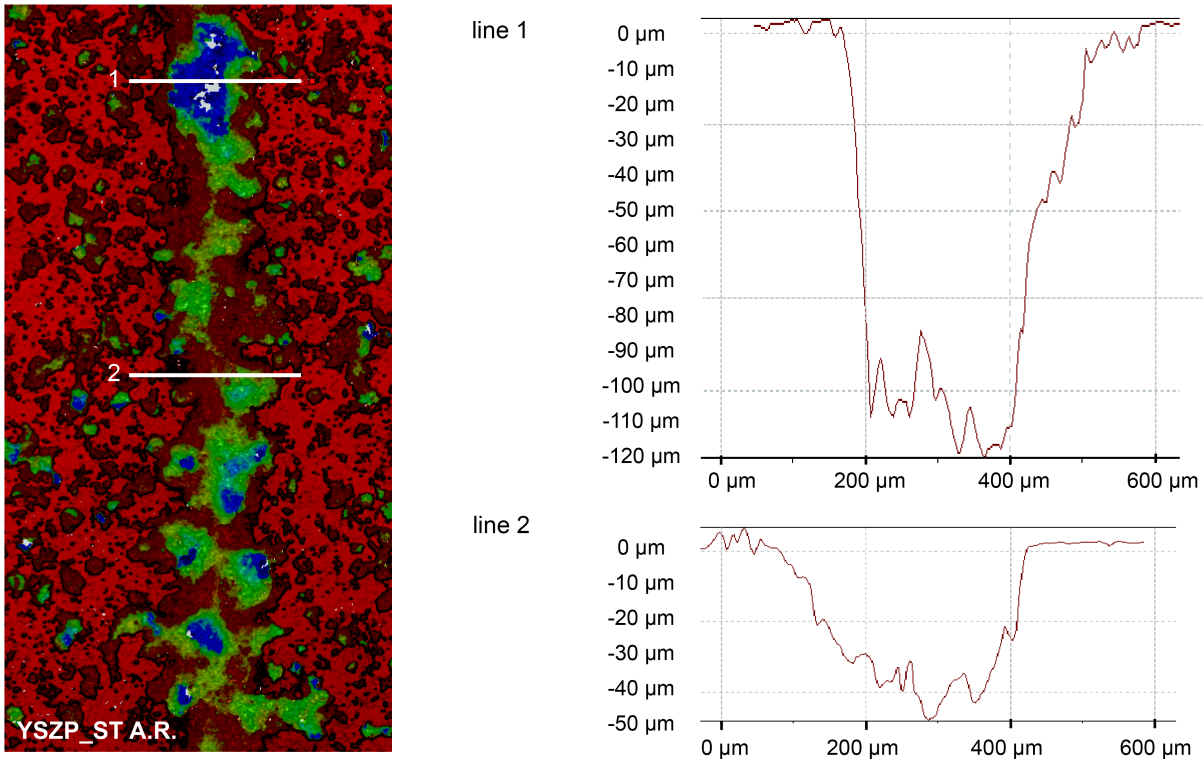

FIGURE 47. Optical vibrometer topography image and line scans for macroscratched YSZP.

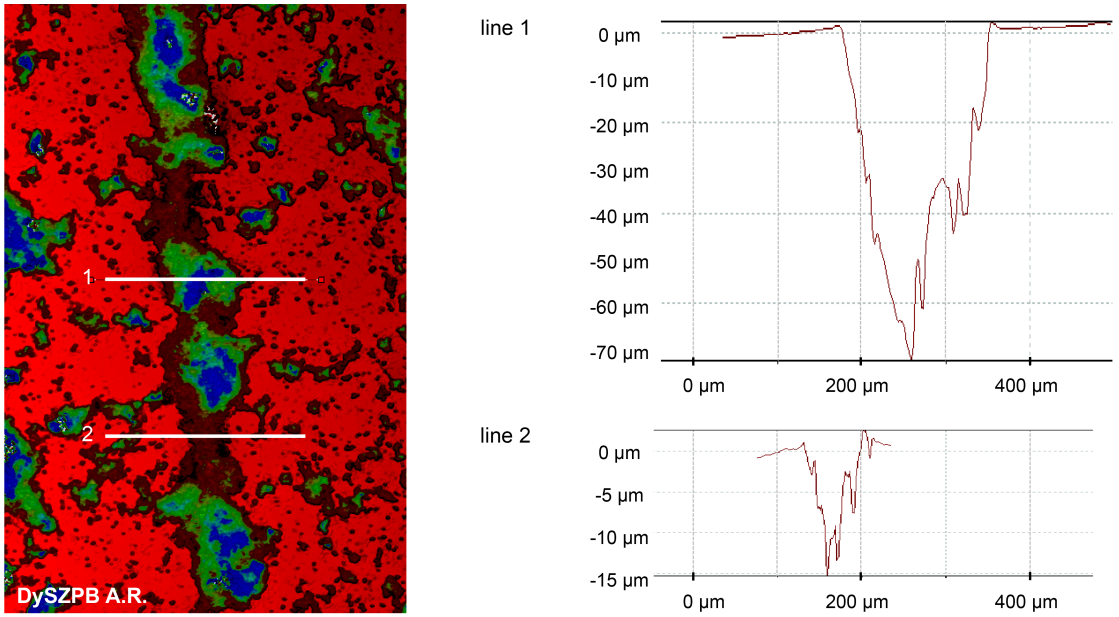

FIGURE 48. Optical vibrometer topography image and line scans for macroscratched DySZPB.

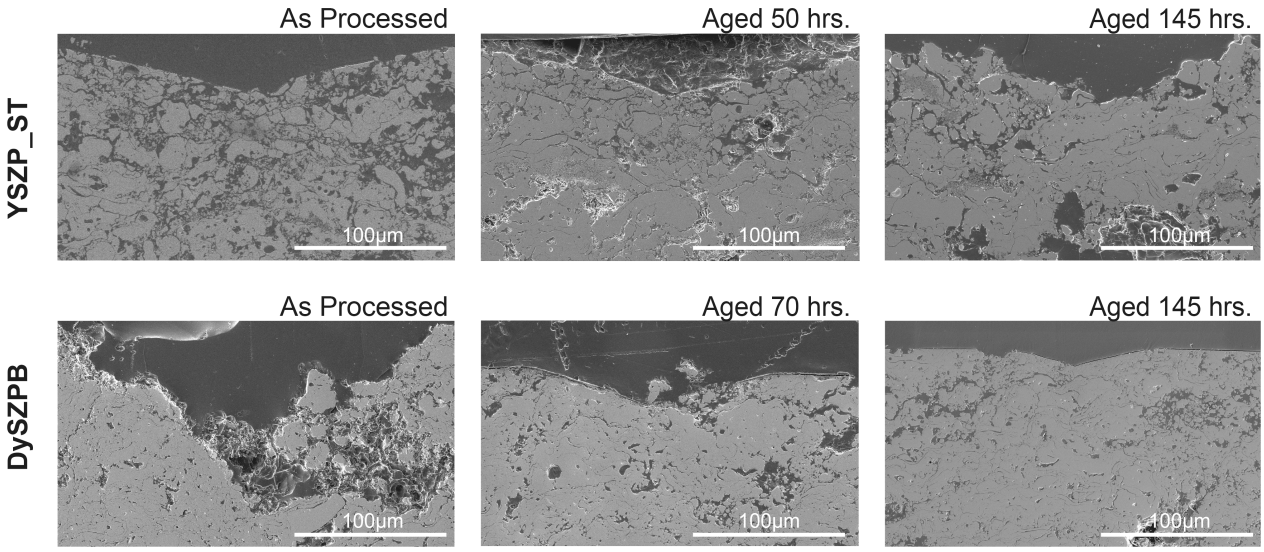

FIGURE 49. Cross sectional SEM images showing the damage zone evolution for macroscratched YSZP_ST and DySZPB coatings with aging.

Cross sectional SEM images of the as received as well as aged YSZP and DySZPB coatings are shown in Figure 49. The as received YSZP coating as well as YSZP aged for 50 hours show a distinct damage zone that penetrates deep within the coating. It is characterized by a particulate-like microstructure where microcracks have broken up the APS splat microstructure, which is shown at higher magnification in Figure 50 in comparison to the DySZPB coating. The YSZP coating aged for 145 hours, however, does not show the same damage zone microstructure and only shows the particulate-like structures near the surface. Multiple areas along the scratch were analyzed by polishing further into samples to ensure the behavior was representative. All DySZPB coatings also do not have the same microcrack penetration deep within the material. The progression of the DySZPB cross sections, however, does show a significant change in scratch track size with aging. The scratch track penetration depth and size becomes significantly smaller with longer aging times.

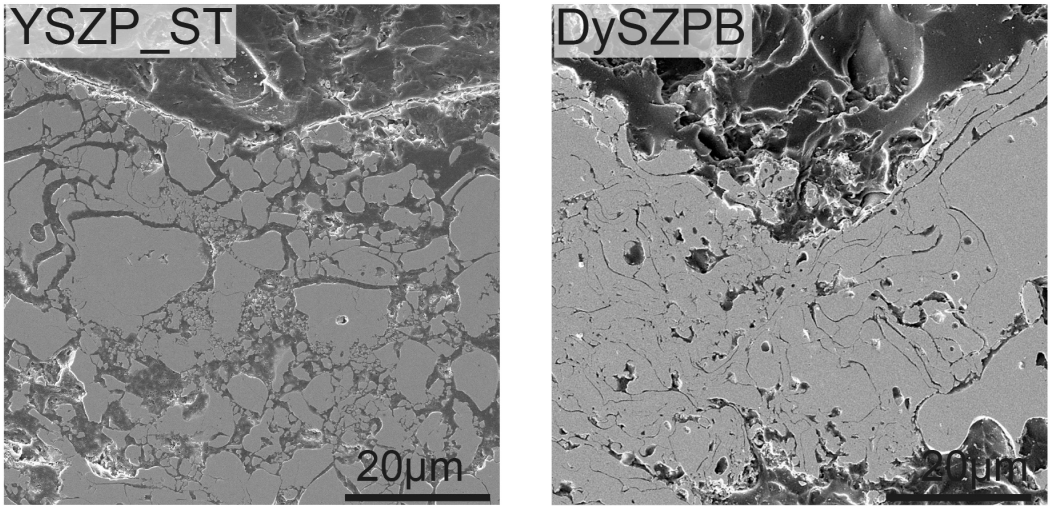

FIGURE 50. Higher magnification cross sectional SEM images showing the different damage zone characteristics in the YSZP_ST (aged, 50 hrs. shown for example) versus DySZPB (as-processed shown).

4.4 Discussion

A first result of this study shows the efficacy of two different lab scale test strategies attempted for use in evaluating the deformation behavior of abradable coating materials using a highly tangential force. The first testing strategy was a microscratch test using a conical diamond tip with a nanoindenter in sliding mode. This ~5 µm in radius tip could be representative of deformation seen when abradable coatings interact with turbine blades that have been tipped with abrasive materials. The attempted progressive load testing, however, did not show the expected wear transitions in the YSZP and DySZPB APS coatings. This is attributed to the combination of highly stochastic microstructural features present in the APS coatings and the sensitivity of the instrument being too high to maintain a straight scratch track at the desired load range of 0-500mN. Using a higher stiffness indenter head or a higher load could have enhanced the efficacy of this method. However, maximum load limitations and indenter head options excluded this as a viable option leading to the implementation of the second macroscratch test setup, which utilized a Vicker's diamond tip indenter to scratch the coatings at

a constant load. This setup employed a tip size significantly larger than the microstructural feature length scales present in the APS abradable coatings, which is more representative of the interaction of an abradable coating with an untipped turbine blade.

Aging studies of both coating materials at conditions representative of two different combustion atmospheres have been shown. It was found that at a current hot section abradable coating working temperature of 1100˚C, densification is the main microstructure evolution that would affect the deformation behavior of the APS abradable coatings. For both low and high water vapor atmospheres used in exposures, the removal of open splat boundaries was seen with no significant difference in sintering seen between high and low water vapor tests at times up to 145 hours.

In addition, this study shows the difference in damage accommodation behavior between two current technology hot section ceramic abradable coatings as well as an evolution of damage mechanism type occurring with aging in the YSZP coating in particular. The two coatings studied in this work are representative of design strategies employed to modify existing ceramic coatings based on TBCs to enable abradability. Both coatings contain defects inherent to the APS process, such as splat features, intrasplat boundaries, fine porosity, microcracking, and columnar grains within a splat, as well as coarse porosity made using pore formers. The two coatings, however, differ with nanozone features present in the YSZP coating, while DySZPB contains BN, as a dislocating phase, and dysprosia as opposed to yttria as the zirconia stabilizer.

In the YSZP coatings, the additional presence of nanozone features, shown in literature to enhance abradability under certain conditions or even introduce plastic-like behavior to the coating, do not show the expected damage accommodation mechanism[69]. The as-processed and

YSZP coating aged for 50 hours show a large damage zone beneath the macroscratch track that extends deep within the coating. It is characteristic of a brittle fracture in the coating with a microcrack network penetrating the weak intercolumnar grains within a splat, thereby breaking up the APS splat features. A similar behavior of crack formation and propagation into the material is seen in the dense, bulk 4YSZ macroscratch damage zone. The highly intergranular fracture seen in the t' 4YSZ bulk material is attributed to the use of the SPS process and fast cooling rate, which produced high residual stress in the coating making it unsuitable for comparison. However, with 145 hours of exposure at 1100˚C and 9.5% H_2O (v), the damage behavior in the YSZP changes to a more lateral fracture with little damage seen beneath the scratch track. Literature studies on APS YSZ have shown that aging increases the modulus and fracture toughness as well as reduces the amount of APS defects present in the coating[98]. From studies on the wear of ceramics, it is known that the extent of lateral and radial cracking is mainly controlled by hardness and fracture toughness with low hardness and fracture toughness resulting in more radial and lateral cracking[77,81]. It is expected that the extent of densification in the YSZP coating aged for 145 hours was sufficient to increase the coating modulus and fracture toughness, which changed the observed damage behavior.

The expected benefit of the difference in the DySZPB coating of using a Dy_2O_3 stabilizer as opposed to Y_2O_3 is to lower thermal conductivity, which has been shown in DySZ TBC materials, and is important for abradable coatings that also provide a thermal barrier for the shroud[75,99]. Performance based testing of DySZPB and YSZP coatings, however, has shown further improved thermal cycling behavior and erosion resistance of the DySZPB coatings in comparison with YSZP[40]. This is likely due to the smaller mole percentage of stabilizer used in the DySZPB (3.3 mol. % DySZ) compared to YSZP (4.2 mol. % YSZ) and corresponding higher

tetragonality of the unit cell, resulting in a more effective use of the t' ferroelastic toughening mechanism present in both DySZ and YSZ materials[100–102]. The enhanced properties reported in literature for DySZPB over YSZP coatings are thus not attributed to an enhanced toughness or different toughening mechanism present in the matrix phase of DySZ versus YSZ, but are instead attributed to using a lower mole fraction of stabilizer in DySZPB.

For the additional secondary phase addition in the DySZPB coating, it was expected that the BN with a hexagonal, graphitic structure would act as a dislocating agent. This dislocating agent promotes abradability with the introduction of its weak bonding between basal planes. However, that expected behavior is challenged by the result in this study that the hexagonal structure is not maintained in the BN phase after APS processing. Neither the amorphous form of BN present after processing nor its properties are known. Regardless, the lateral fracture dominated damage behavior in the DySZPB coatings with little extension through the coating thickness is more similar to the behavior seen in the damage zone of the bulk YSZ-hBN composite. This is seen in all the DySZPB coatings despite the increased hardness and extensive densification evident in microstructures with aging, which suggests this secondary phase plays a role in maintaining a constant damage accommodation mechanism.

A final significant finding shown in this work is that increased hardness does not always signify a decrease in abradability, which is the current understanding in literature to date. The DySZPB coatings showed the most extensive densification and a larger than two fold increase in hardness with aging yet maintained a constant behavior with little damage accommodation extending deep within the material. The extent of densification in YSZP, however, does not cause a significant increase in hardness of the aged coatings. Yet, the damage accommodation behavior of the YSZP coatings changes at higher aging times. This signifies that hardness alone

is not a good predictor of the ease of abradability because it is unable to give insight into the underlying damage accommodation mechanism for materials with a range of microstructural features.

4.5 Summary and Future Directions

Key insights into the effect of microstructural design in promoting desirable abradable behavior have been shown in this study through the use of a lab-scale macroscratch test. DySZPB coatings show a significant increase in hardness with aging due to a high extent of densification resulting in the removal of open splat boundaries. This increase in hardness was thought previously to degrade abradable performance. However, these coatings show predictable damage behavior with aging and little to no damage extension to the microstructure beneath the scratch track, which is attributed to the presence of the secondary BN phase. The YSZP coatings, on the other hand, exhibit highly brittle fracture changing only with longer aging times. Since interactions with the blade are expected upon first start up of the engine as well as with higher operating times, this brittle fracture could not only compromise the integrity of the remaining coating but also send debris to impact turbine components further downstream. Further work must be done to understand the significance of secondary phase additions in abradable coating behavior, as well as how these lab-scale tests compare to testing at higher strain rates and temperatures.

An important direction for future work is the development of a more controlled testing setup that can probe the different length scale interactions representative of the coating being abraded with both tipped and untipped turbine blades. Ideally a new setup should be developed that can test at a range of strain rates and loads in order to establish the change in damage accommodation behavior in the coatings as a function of scratch tip size as well as strain rate.

Establishing this new setup would allow the effective evaluation of current abradable coating behavior as well as provide an effective way of screening new coating designs in a more time and cost effective manner than the existing industry-scale high temperature rub rig tests.

CHAPTER 5: Summary and Future Outlook

5.1 Summary

Abradable coatings are used for clearance control in both aerospace and power generation turbines to improve gas flow utilization for producing mechanical energy. The use of abradable coatings in turbine hot sections requires the implementation of ceramic materials, which are inherently brittle, creating a unique combination of properties that must be met in the design of these coating systems. Until this study, that unique combination of properties was only known to the extent that a certain set of processing parameters were connected to enhanced performance when tested with mostly industrial-scale test rigs. The findings of this study give insight into the different mechanisms by which ceramic abradable coatings can accommodate damage, the key microstructural features that enable these accommodation mechanisms, and the evolution of behavior in the coatings under simulated working conditions. These insights can be used to guide design strategies for the next generation of ceramic abradable coatings that are able to withstand more harsh environments and higher temperatures.

A first finding is the establishment of potential blade and ceramic abradable coating interactions in the turbine hot section. Both favorable and unfavorable interactions were presented. The expected failure criteria and behavior for each interaction type have been evaluated using existing mechanics analysis frameworks for coating cracking and delamination as well as existing wear of ceramics behavior.

Next, experimental studies using two current technology ceramic hot section abradable systems were completed to:

- determine a lab-scale test setup able to probe the abradable wear mechanisms of ceramic abradable coatings;
- study the microstructural evolution in representative turbine hot section working conditions, in both low and high water vapor environments as well as at high temperature for extended times representative of higher operating times in the turbine;
- and investigate the effect of different microstructural features present in the coating systems and their evolution with aging on the damage accommodation behavior seen in the coatings when tested at the lab-scale.

Results from these experimental studies give insight into the different features present in the current technology coatings that are advantageous for abradability when tested at lab-scale. This lab-scale test could prove a valuable screening tool for the future design of hot section abradable coating systems. The summary of the detailed findings for each of these aspects is given below.

5.1.1 Potential Damage Mechanisms Analysis

This study has filled previously existing gaps in understanding of the underlying mechanisms and applicable fracture mechanics analysis that aid the design of these inherently brittle materials enabling them to accommodate damage in a controlled manner. The aim of this part of the work was to use relevant theories for fracture mechanics and wear mechanisms in ceramics to establish pathways for developing an understanding, analysis, and prediction of damage accommodation in existing ceramic abradable coating designs. Unfavorable coating and blade interactions have been established, which are blade wear when the abradable coating is

unable to absorb the energy of the rub impact because of high hardness or toughness, or coating rupture when the coating undergoes uncontrolled brittle fracture. Coating rupture can occur with external or internal drivers causing crack propagation to penetrate deep within the coating.

Furthermore, potential favorable interactions have been determined. The first relies on coating compaction enabled by pseudo-plastic deformation, which can occur through coating porosity allowing compaction or high temperature plasticity enabling material redistribution. One way porosity can enable pseudo-plastic deformation is when the material above the pore undergoes microcracking. This microcracked zone formation is dictated by indentation fracture behavior. On the other hand, the material may redistribute to the pore cavity through interface sliding, which is explained by plastic deformation of ceramics at high temperatures incorporating both creep and viscoplasticity.

A second favorable interaction in the coating is the controlled propagation of cracks through elastic fracture controlled by additional secondary weakening phases or by the existence of pre-existing flaws. For the case of secondary weakening phases, the behavior of the crack and effectiveness of the weakening phase at redirecting the crack is highly dependent on the orientation and the properties of the bulk material as compared to the secondary, weakening phase. In this case, the most effective use of the weakening phase is to deflect the impeding crack or crack network at horizontally oriented boundaries to deflect along that interface.

5.1.2 Determination of Lab-scale Test Method

Scratch testing with a nanoindenter under progressive loading was first attempted. With this test, wear mechanism transitions were expected along the length of the scratch. However, the characteristics along the length of the scratch tracks of both coating systems were

variable, changing from plowing to extensive lateral fracture and flake formation then back to plowing. These transitions did not correspond to any particular microstructural feature in the coating and was not consistent between several different scratches performed on the same material. The inconsistencies in nanoindentation scratch behavior was expectedly due to the stochastic nature of the APS coatings, the size of the indenter tip not being sufficiently larger than the APS microstructural features, and the sensitivity of the instrument tip resulting in failed scratch tests. Using a larger size indenter tip was investigated, but the system in use did not have high enough load capacity to probe a large enough depth. Thus, further testing was explored to accurately test the behavior of the coating materials.

The macroscratch test using a Vicker's indenter at constant load was then investigated. The larger indenter tip size and higher load capabilities of the instrument allowed an area of the material to be examined significantly larger than the microstructural features present in the coatings. The macroscratch tests, in addition, gave repeatable results that followed trends seen in the literature with hardness. It also allowed an easy comparison between hardness values and scratch track behavior since no size effects would need to be taken into account because both tests used a Vicker's indenter tip.

5.1.3 Evolution of Hot Section Abradable Coatings with Aging Studies

Both low and high water vapor environments, representative of natural gas fired and synthetic gas fired turbines, respectively, were used to study the evolution of the two current technology coatings at conditions simulating higher operating times in the turbine. The YSZ-polyester coating system showed no significant change in higher water vapor versus low at 1100˚C exposure temperature and times up to 145 hours. However, the DySZ-BN-polyester

coatings showed a larger increase in overall porosity percentage in higher water vapor exposure environment due to the oxidation, volatilization reaction of BN being enhanced in a higher water vapor environment.

The reduction of open APS splat boundaries in both coating systems, however, was the most prevalent evolution with aging in both environments. It was particularly evident in the DySZPB coatings with extensive closing of the open splat boundaries seen. When comparing the low versus high water vapor aging experiments for each material, similar extents of intrasplat boundary removal are seen with no significant differences between the two at the same exposure time seen with the aging times used in this study. Instead, the difference in the extent of splat boundary removal through the bridging mechanism is dominated by the higher extent of sintering seen with longer exposure times.

5.1.4 The Effect of Microstructural Features on Damage Behavior

Key insights into the effect of microstructural design in promoting desirable abradable behavior have been shown in this study through the use of a lab-scale macroscratch test. Both coating systems in the as-processed and aged states, as well as bulk materials, were tested. The YSZ bulk materials showed highly brittle behavior below the scratch track with median and lateral crack extension into the coating while the YSZ-hBN composite showed no evidence of crack extension. The as received coatings showed similar trends as the bulk materials with the YSZ-polyester coating having extensive cracking below the scratch track that broke up the individual APS splat features leaving particulate-like microstructural features and a defined damage zone. The DySZ-BN-polyester coating in the as-processed state showed some radial and surface cracking but no defined damage zone beneath the scratch track.

Testing of the aged coatings showed that the hardness of the DySZPB coatings increased with aging due to a high extent of densification resulting in the removal of open splat boundaries. This increase in hardness was thought previously to degrade abradable performance. However, these coatings exhibited predictable damage behavior with aging and little to no damage extension to the microstructure beneath the scratch track, which was attributed to the presence of the secondary BN phase. The YSZP coatings, on the other hand, exhibit highly brittle fracture and an extensive damage zone beneath the scratch track, which changes only with longer aging times. At 145 hours of aging, the YSZP coating showed no significant increase in hardness, and yet, the cracking behavior changed to more surface and radial cracking instead of the extensive crack network beneath the track as seen with shorter aging times. The YSZP coatings, with the additional presence of nanozone features, shown in literature to enhance abradability under certain conditions or even introduce plastic-like behavior to the coating, do not show the expected damage accommodation mechanism. Instead they show brittle failure with the mechanism changing at higher aging time despite little change in hardness, which was thought previously to signify a change in abradable behavior. Damage zone investigation suggests that the secondary BN phase plays a key role in allowing the coating to maintain a shallow damage zone without extension into the coating microstructure beneath, thus exhibiting more favorable abradable behavior. A key insight from this study suggests that abradable design utilizing a higher concentration of secondary, weakening phase is critical for consistent and predictable abradable behavior.

5.2 Future Outlook

Mechanisms by which ceramic hot section abradable coatings accommodate damage after interaction with turbine blades were presented. In service, the synergistic effect of

each potential deformation behavior can occur. Thus, it is imperative for future work to be done in conjunction with resultant deformation behavior observed from field hardware to build an understanding encompassing all relevant mechanisms. Since experimental studies showed that the secondary BN phase in the DySZPB coatings assisted in a more controlled damage behavior, important issues to address with future work are that of understanding the ability of interfacial weakening phases to deflect or absorb cracks. Future work can be done to understand the effect of different anisotropic secondary phases, and models should incorporate strain rate dependent behavior as well as the effect of different geometries and properties of the abrasive medium. The parameters of the deforming medium and different aspects of the microstructure of the coating that should be incorporated into future models are illustrated in Figure 51. The model would ideally incorporate each of the following:

- dimensions of the deforming body, such as the incursion depth (d), radius of curvature of the blade (r), and the width of blade contact (w).
- energy input, such as blade velocity and incursion rate.
- microstructural features present in the coating, such as percentage of splat bonding or concentration of open interfaces, concentration of weak interfaces, splat thickness, and porosity.
- coating properties, such as hardness, toughness, and modulus.
- volume of material removed.

Studies to understand the effect of the matrix material properties, such as toughness, on abradability are also important for future work. Preliminary studies on probing the

importance of the t' toughening mechanism in DySZ vs. YSZ are presented in Appendix C. It is reported in the literature that DySZ-based abradable coatings have higher erosion resistance and better thermal cycling life to YSZ-based coatings[20,27,40]. A major factor that could improve these properties is toughness, in particular the extent of the t' toughening mechanism occurring in the matrix materials. Work from Mercer, et al [15] has probed the extent of t' toughening mechanism in YSZ by mapping the extent of the transformation zone seen as distorted areas at the surface around indentation cracks. TEM was used to confirm the ferroelastic domain formation at the distorted areas. Preliminary work was done to first make bulk t' YSZ and DySZ materials using spark plasma sintering. Commercial Tosoh YSZ powders were used, but DySZ was not found to be available commercially. The methods for synthesizing DySZ powders are based on the procedure from Anithakumari, et al [103] and are outlined in the Appendix C. Images of the preliminary results for t' YSZ are also shown in Appendix C. However, even though the t' YSZ bulk material showed distortion around the indentation cracks, TEM did not show the formation of domain structures in those areas. This is likely due to the fact that the SPS in use had temperature limitations that restricted the resultant phases to approximately 60% t' phase because the maximum sintering temperatures were still in the two phase, cubic and tetragonal, region of the YSZ phase diagram. Thus, only the fraction of material that was cubic at the sintering temperature would result in the t' phase upon fast cooling. The fast cooling rate necessary to block diffusion of the material into its equilibrium tetragonal phase also produced high residual stresses in the SPS processed pellets further complicating the study. Therefore, future work can be done to improve the SPS parameters with optimally higher sintering temperatures to obtain higher fractions of t' phase in both the YSZ and DySZ materials. Once this has been completed, the extents of the transformation zones in both materials can be

compared to confirm whether DySZ has more effective toughening and what affect that has on abradability.

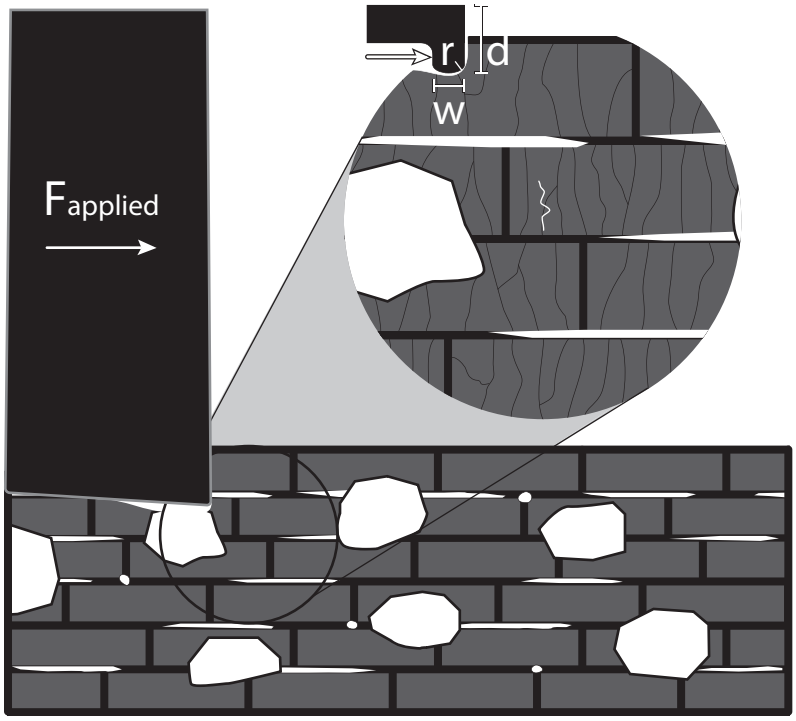

FIGURE 51. Schematic illustrating important parameters of the blade as well as coating material for future models.

Further work to understand the significance of bulk material properties as well as secondary phase additions in abradable coating behavior must incorporate how these lab-scale tests compare to testing at higher strain rates and temperatures. Directions for this future work would be to develop a more controlled testing setup that can probe the different length scale interactions representative of the coating being abraded with both tipped and untipped turbine blades. Ideally a new setup should be designed that can test at a range of strain rates and loads in order to establish the change in damage accommodation behavior in the coatings as a function of scratch tip size as well as strain rate. Preliminary design ideas for this future work are illustrated in Appendix D. Establishing this new setup would allow the effective evaluation of current abradable coating behavior as well as provide an effective way of screening new coating designs

in a more time and cost effective manner than the existing industry-scale high temperature rub rig tests.

REFERENCES

1. Birol, F. Key World Energy Statistics Report 2018. (2018).

2. White, B. M., Ames, R. W. & Burke, P. CONDITIONS IN ADVANCED TURBINES FOR IGCC POWER PLANTS WITH CARBON CAPTURE. in *PROCEEDINGS OF THE ASME TURBO EXPO: TURBINE TECHNICAL CONFERENCE AND EXPOSITION, 2013, VOL 2* (2013).

3. Meschter, P. J., Opila, E. J. & Jacobson, N. S. Water Vapor-Mediated Volatilization of High-Temperature Materials. in *ANNUAL REVIEW OF MATERIALS RESEARCH, VOL 43* (ed. Clarke, DR) **43,** 559–588 (2013).

4. Pint, B. A., Unocic, K. A. & Haynes, J. A. The Effect of Environment on Thermal Barrier Coating Lifetime. *J. Eng. GAS TURBINES POWER-Trans. ASME* **138,** (2016).

5. RollsRoyce, plc. Rolls Royce The Jet Engine.

6. Solar Turbines. Gas Compressor Packages: Titan 130. (2018).

7. Pratt and Whitney Corp. PW 6000 Engine. (2018).

8. DEMASIMARCIN, J. & GUPTA, D. PROTECTIVE COATINGS IN THE GAS-TURBINE ENGINE. *Surf. Coat. Technol.* **68,** 1–9 (1994).

9. Darolia, R. Thermal barrier coatings technology: critical review, progress update, remaining challenges and prospects. *Int. Mater. Rev.* **58,** 315–348 (2013).

10. Clarke, D. R., Oechsner, M. & Padture, N. P. Thermal-barrier coatings for more efficient gas-turbine engines. *MRS Bull.* **37,** 891–902 (2012).

11. Cao, X., Vassen, R. & Stoever, D. Ceramic materials for thermal barrier coatings. *J. Eur. Ceram. Soc.* **24,** 1–10 (2004).

12. Hardwicke, C. U. & Lau, Y.-C. Advances in Thermal Spray Coatings for Gas Turbines and Energy Generation: A Review. *J. Therm. SPRAY Technol.* **22,** 564–576 (2013).

13. VIRKAR, A. & MATSUMOTO, R. FERROELASTIC DOMAIN SWITCHING AS A TOUGHENING MECHANISM IN TETRAGONAL ZIRCONIA. *J. Am. Ceram. Soc.* **69,** C224–C226 (1986).

14. Lipkin, D. M. *et al.* Phase Evolution upon Aging of Air-Plasma Sprayed t'-Zirconia Coatings: ISynchrotron X-Ray Diffraction. *J. Am. Ceram. Soc.* **96,** 290–298 (2013).

15. Mercer, C., Williams, J. R., Clarke, D. R. & Evans, A. G. On a ferroelastic mechanism governing the toughness of metastable tetragonal-prime (t `) yttria-stabilized zirconia. *Proc. R. Soc. -Math. Phys. Eng. Sci.* **463,** 1393–1408 (2007).

16. Aygun, A., Vasiliev, A. L., Padture, N. P. & Ma, X. Novel thermal barrier coatings that are resistant to high-temperature attack by glassy deposits. *ACTA Mater.* **55,** 6734–6745 (2007).

17. Drexler, J. M. *et al.* Plasma sprayed gadolinium zirconate thermal barrier coatings that are resistant to damage by molten Ca-Mg-Al-silicate glass. *Surf. Coat. Technol.* **206,** 3911–3916 (2012).

18. Zhao, H., Levi, C. G. & Wadley, H. N. G. Molten silicate interactions with thermal barrier coatings. *Surf. Coat. Technol.* **251,** 74–86 (2014).

19. Irissou, E., Dadouche, A. & Lima, R. S. Tribological Characterization of Plasma-Sprayed CoNiCrAlY-BN Abradable Coatings. *J. Therm. SPRAY Technol.* **23,** 252–261 (2014).

20. Sporer, D. *et al.* New high-temperature seal system for increases efficiency of gas turbines. *Seal. Technol.* 9–11 (2008).

21. Batailly, A. & Legrand, M. Unilateral contact induced blade/casing vibratory interactions in impellers: Analysis for flexible casings with friction and abradable coating. *J. SOUND Vib.* **348,** 344–364 (2015).

22. Sulzer, M. Improve Efficiency and Reduce Emissions with High Pressure Turbine Abradable Coatings for Industrial Gas Turbines. (2012).

23. Delebarre, C. *et al.* An experimental study of the high speed interaction between a labyrinth seal and an abradable coating in a turbo-engine application. *WEAR* **316,** 109–118 (2014).

24. Scrinzi, E., Giovannetti, L., Sheng, N. & Leblanc, L. DEVELOPMENT OF NEW ABRADABLE/ABRASIVE SEALING SYSTEMS FOR CLEARANCE CONTROL IN GAS TURBINES. in *PROCEEDINGS OF THE ASME TURBINE BLADE TIP TECHNICAL SYMPOSIUM, 2013* (2014).

25. Steinke, T. *et al.* Process Design and Monitoring for Plasma Sprayed Abradable Coatings. *J. Therm. SPRAY Technol.* **19,** 756–764 (2010).

26. Foroushani, M. H., Shamanian, M., Salehi, M. & Davar, F. Porosity analysis and oxidation behavior of plasma sprayed YSZ and YSZ/LaPO4 abradable thermal barrier coatings. *Ceram. Int.* **42,** 15868–15875 (2016).

27. Sporer, D., Wilson, S., Giovannetti, I., Arno, R. & Giannozzi, M. On the Potential of Metal and Ceramic Based Abradables in Turbine Seal Applications. *Turbomach. Pump Symp.* 79–86 (2007).

28. D. B. Allen. Process of Producing an Abradable Thermal Barrier Coating with Solid Lubricant. 2010

29. Bucci, D. V., Kottilingam, S. C. & Singh, P. Method for 3D Printing a pattern for the surface of a turbine shroud. (2013).

30. Nicoll, A. & Wilson, S. Ceramic Abradable Material with Alumina Dopant.

31. Bill, R. C. & Wisander, D. W. Friction and wear of several compressor gas-path seal materials. (1978).

32. Chupp, R., Hendricks, R., Lattime, S. & Steinetz, B. Sealing in turbomachinery. *J. Propuls. POWER* **22,** 313–349 (2006).

33. MARSCHER, W. PHENOMENOLOGICAL MODEL OF ABRADABLE WEAR IN HIGH-PERFORMANCE TURBOMACHINERY. *WEAR* **59,** 191–211 (1980).

34. Lamuta, C., Di Girolamo, G. & Pagnotta, L. Microstructural, mechanical and tribological properties of nanostructured YSZ coatings produced with different APS process parameters. *Ceram. Int.* **41,** 8904–8914 (2015).

35. Ma, X. & Matthews, A. Evaluation of abradable seal coating mechanical properties. *WEAR* **267,** 1501–1510 (2009).

36. VAC, A. Abradable Coatings used for Gas Path Seals in Turbine Engines. (2014).

37. Wilson, S. Thermally sprayed abradable coating technology for sealing in gas turbines. in *Thermally Sprayed Abradable Coatings 2012* (Oerlikon Metco, 2012).

38. Lugscheider, E., Zwick, J., Hertter, M. & Sporer, D. Coating Properties of Abradable Seals by Online Process Diagnostics. in *Proceedings* 610–614 (2005).

39. Oerlikon Metco. An Introduction to Thermal Spray. (2016).

40. Sporer, D. *et al.* Dysprosia stabilized zirconia abradable. (2007).

41. Ilavsky, J. & Stalick, J. Phase composition and its changes during annealing of plasma-sprayed YSZ. *Surf. Coat. Technol.* **127,** 120–129 (2000).

42. Wang, C., Zinkevich, M. & Aldinger, F. Phase diagrams and thermodynamics of rare-earth-doped zirconia ceramics. *PURE Appl. Chem.* **79,** 1731–1753 (2007).

43. Witz, G., Shklover, V., Steurer, W., Bachegowda, S. & Bossmann, H.-P. Phase evolution in yttria-stabilized zirconia thermal barrier coatings studied by rietveld refinement of X-ray powder diffraction patterns. *J. Am. Ceram. Soc.* **90,** 2935–2940 (2007).

44. Viazzi, C., Bonino, J.-P., Ansart, F. & Barnabe, A. Structural study of metastable tetragonal YSZ powders produced via a sol-gel route. *J. ALLOYS Compd.* **452,** 377–383 (2008).

45. Scheu, C. & Kaplan, W. D. *In situ electrom microscopy: applications in physics, chemistry, ad materials science*. (Wiley, 2012).

46. Goldsteiin, J. I., Newbury, D. E., Michael, J. R., Ritchie, N. W. M. & Joy, D. C. *Scanning electron microscopy and x-ray microanalysis*. (Springer, 2017).

47. Hammond, C. *The Basics of Crystallography and Diffraction*. (Oxford Science Publications, 2009).

48. Carter, C. B. & Norton, M. G. *Ceramic Materials Science and Engineering*. (Springer, 2013).

49. Saha, S. *et al.* Comparative high pressure Raman study of boron nitride nanotubes and hexagonal boron nitride. *Chem. Phys. Lett.* **421,** 86–90 (2006).

50. Agilent Technologies Inc. *Agilent Technologies Nano Indenter G200 User's Guide*. (2013).

51. Polytec. MSA-500 Micro System Analyzer.

52. Malacara, D. *Optical Shop Testing*. (John Wiley & Sons, 2007).

53. Schmit, J. An introduction to non contact metrology. *Bruker Corp. Online Doc.* 2–46 (2013).

54. Hendricks, R. C., Dimofte, F., Chupp, R. E. & Steinetz, B. M. Interfaces - Weak Links, Yet Great Opportunities. in (International Journal of Rotating Machinery, 2011).

55. LAWN, B., PADTURE, N., CAI, H. & GUIBERTEAU, F. MAKING CERAMICS DUCTILE. *SCIENCE* **263,** 1114–1116 (1994).

56. Ritchie, R. O. & Launey, M. O. *Crack Growth in Brittle and Ductile Solids*. (Springer, 2013).

57. Pro, J. W., Lim, R. K., Petzold, L. R., Utz, M. & Begley, M. R. The impact of stochastic microstructures on the macroscopic fracture properties of brick and mortar composites. *EXTREME Mech. Lett.* **5,** 1–9 (2015).

58. He, M., Mumm, D. & Evans, A. Criteria for the delamination of thermal barrier coatings: with application to thermal gradients. *Surf. Coat. Technol.* **185,** 184–193 (2004).

59. BECHER, P. MICROSTRUCTURAL DESIGN OF TOUGHENED CERAMICS. *J. Am. Ceram. Soc.* **74,** 255–269 (1991).

60. Choi, S., Hutchinson, J. & Evans, A. Delamination of multilayer thermal barrier coatings. *Mech. Mater.* **31,** 431–447 (1999).

61. Evans, A., Mumm, D., Hutchinson, J., Meier, G. & Pettit, F. Mechanisms controlling the durability of thermal barrier coatings. *Prog. Mater. Sci.* **46,** 505–553 (2001).

62. Mumm, D. & Evans, A. On the role of imperfections in the failure of a thermal barrier coating made by electron beam deposition. *ACTA Mater.* **48,** 1815–1827 (2000).

63. Faraoun, H. *et al.* Modelling route for abradable coatings. *Surf. Coat. Technol.* **200,** 6578–6582 (2006).

64. Saouma, V. E. Fracture Mechanics. (2017).

65. Hendricks, R. C., Chupp, R. E., Lattime, S. B. & Steinetz, B. M. Turbomachine Interface Sliding. in *AVS Science and Technology* (NASA, 2005).

66. Steinetz, B. M. Overview of NASA Glenn Seal Program. in **1,** (NASA, 2002).

67. Aussavy, D. *et al.* YSZ-Polyester Abradable Coatings Manufactured by APS. *J. Therm. SPRAY Technol.* **25,** 252–263 (2016).

68. Strock, C. W. & Reynolds, G. H. Lubricated Abradable Coating.

69. Lima, R. S. & Marple, B. R. Thermal spray coatings engineered from nanostructured ceramic agglomerated powders for structural, thermal barrier and biomedical applications: A review. *J. Therm. SPRAY Technol.* **16,** 40–63 (2007).

70. Ebert, S. *et al.* Failure mechanisms of magnesia alumina spinel abradable coatings under thermal cyclic loading. *J. Eur. Ceram. Soc.* **33,** 3335–3343 (2013).

71. Sulzer. Thermal Spray Materials Guide. (2012).

72. NOVINSKI, E., HARRINGTON, J. & KLEIN, J. MODIFIED ZIRCONIA ABRADABLE SEAL COATING FOR HIGH-TEMPERATURE GAS-TURBINE APPLICATIONS. *THIN SOLID FILMS* **95,** 255–263 (1982).

73. Guo, H., Vassen, R. & Stover, D. Atmospheric plasma sprayed thick thermal barrier coatings with high segmentation crack density. *Surf. Coat. Technol.* **186,** 353–363 (2004).

74. Karger, M., Vassen, R. & Stoever, D. Atmospheric plasma sprayed thermal barrier coatings with high segmentation crack densities: Spraying process, microstructure and thermal cycling behavior. *Surf. Coat. Technol.* **206,** 16–23 (2011).

75. STRANGMAN, T. THERMAL STRAIN-TOLERANT ABRADABLE THERMAL BARRIER COATINGS. *J. Eng. GAS TURBINES POWER-Trans. ASME* **114,** 264–267 (1992).

76. Smarsly, W. *et al.* Advanced high temperatrue turbine seals materials and designs. (2005).

77. KATO, K. TRIBOLOGY OF CERAMICS. *WEAR* **136,** 117–133 (1990).

78. EVANS, A., CHESNUTT, J. & NADLER, H. QUASI-STATIC SOLID PARTICLE IN DAMAGE IN BRITTLE SOLIDS .2. INDENTATION FRICTION. *ACTA Metall.* **24,** 867–870 (1976).

79. EVANS, A. ABRASIVE WEAR OF CERAMICS. *Am. Ceram. Soc. Bull.* **56,** 292 (1977).

80. Hwang, T. & Malkin, S. Grinding mechanisms and energy balance for ceramics. *J. Manuf. Sci. Eng.-Trans. ASME* **121,** 623–631 (1999).

81. Evans, A. G. & Marshall, D. B. Wear Mechanisms in Ceramics. *Fundam. Frict. Wear Mater.* 439–451 (1981).

82. He, M.-Y. & Hutchinson, J. W. Kinking of a Crack Out of an Interface. *J. Appl. Mech.-Trans. ASME* **56,** 270–278 (1989).

83. Davis, J., Kristoffersson, A., Carlstrom, E. & Clegg, W. Fabrication and crack deflection in ceramic laminates with porous interlayers. *J. Am. Ceram. Soc.* **83,** 2369–2374 (2000).

84. Messerschmidt, U., Baither, D., Baufeld, B. & Bartsch, M. Plastic deformation of zirconia single crystals: a review. *Mater. Sci. Eng. -Struct. Mater. Prop. Microstruct. Process.* **233,** 61–74 (1997).

85. NIEH, T. & WADSWORTH, J. DYNAMIC GRAIN-GROWTH DURING SUPERPLASTIC DEFORMATION OF YTTRIA-STABILIZED TETRAGONAL ZIRCONIA POLYCRYSTALS. *J. Am. Ceram. Soc.* **72,** 1469–1472 (1989).

86. Kim, B. N., Hiraga, K., Morita, K. & Sakka, Y. A high-strain-rate superplastic ceramic. *Nature* **413,** 288–291 (2001).

87. He, R., Qu, Z., Pei, Y. & Fang, D. High temperature indentation tests of YSZ coatings in air up to 1200 degrees C. *Mater. Lett.* **209,** 5–7 (2017).

88. Xu, H. & Guo, H. *Thermal Barrier Coatings*. (Woodhead Publishing Limited, 2011).

89. HE, M. & HUTCHINSON, J. CRACK DEFLECTION AT AN INTERFACE BETWEEN DISSIMILAR ELASTIC-MATERIALS. *Int. J. SOLIDS Struct.* **25,** 1053–1067 (1989).

90. Lee, G., Dharan, C. & Ritchie, R. A physically-based abrasive wear model for composite materials. *WEAR* **252,** 322–331 (2002).

91. Bardi, U. *et al.* Development and Investigation on New Composite and Ceramic Coatings as Possible Abradable Seals. *J. Therm. SPRAY Technol.* **17,** 805–811 (2008).

92. Erk, K., Deschaseaux, C. & Trice, R. Grain-boundary grooving of plasma-sprayed yttria-stabilized zirconia thermal barrier coatings. *J. Am. Ceram. Soc.* **89,** 1673–1678 (2006).

93. Curry, N., Janikowski, W., Pala, Z., Vilemova, M. & Markocsan, N. Impact of Impurity Content on the Sintering Resistance and Phase Stability of Dysprosia- and Yttria-Stabilized Zirconia Thermal Barrier Coatings. *J. Therm. SPRAY Technol.* **23,** 160–169 (2014).

94. HOKKIRIGAWA, K. WEAR MODE MAP OF CERAMICS. *WEAR* **151,** 219–228 (1991).

95. Xu, Z. *et al.* Large-scale fabrication of porous YBO3 hollow microspheres with tunable photoluminescence. *R. Soc. OPEN Sci.* **5,** (2018).

96. Knyrim, J. S. & Huppertz, H. High-pressure synthesis, crystal structure, and properties of the first ternary zirconium borate beta-ZrB2O5. *Z. NATURFORSCHUNG Sect. B- J. Chem. Sci.* **63,** 707–712 (2008).

97. Cipitria, A., Golosnoy, I. O. & Clyne, T. W. A sintering model for plasma-sprayed zirconia TBCs. Part I: Free-standing coatings. *ACTA Mater.* **57,** 980–992 (2009).

98. Dwivedi, G., Viswanathan, V., Sampath, S., Shyam, A. & Lara-Curzio, E. Fracture Toughness of Plasma-Sprayed Thermal Barrier Ceramics: Influence of Processing, Microstructure, and Thermal Aging. *J. Am. Ceram. Soc.* **97,** 2736–2744 (2014).

99. Munawar, A. U., Schulz, U., Cerri, G. & Lau, H. Microstructure and cyclic lifetime of Gd and Dy-containing EB-PVD TBCs deposited as single and double-layer on various bond coats (vol 245C, pg 92, 2014). *Surf. Coat. Technol.* **279,** 53 (2015).

100. Schaedler, T. A., Leckie, R. M., Kraemer, S., Evans, A. G. & Levi, C. G. Toughening of nontransformable t `-YSZ by addition of titania. *J. Am. Ceram. Soc.* **90,** 3896–3901 (2007).

101. Tsipas, S. A. Effect of dopants on the phase stability of zirconia-based plasma sprayed thermal barrier coatings. *J. Eur. Ceram. Soc.* **30,** 61–72 (2010).

102. LOG, T., CUTLER, R., JUE, J. & VIRKAR, A. POLYCRYSTALLINE T'-ZRO2(LN2O3) FORMED BY DISPLACIVE TRANSFORMATIONS. *J. Mater. Sci.* **28,** 4503–4509 (1993).

103. Anithakumari, P., Grover, V. & Tyagi, A. K. Structure-modulated ionic transport behavior in zirconia-dysprosia mixed oxides. *J. Mater. Sci.* **51,** 6711–6721 (2016).

APPENDIX A: Tube Furnace Fixtures

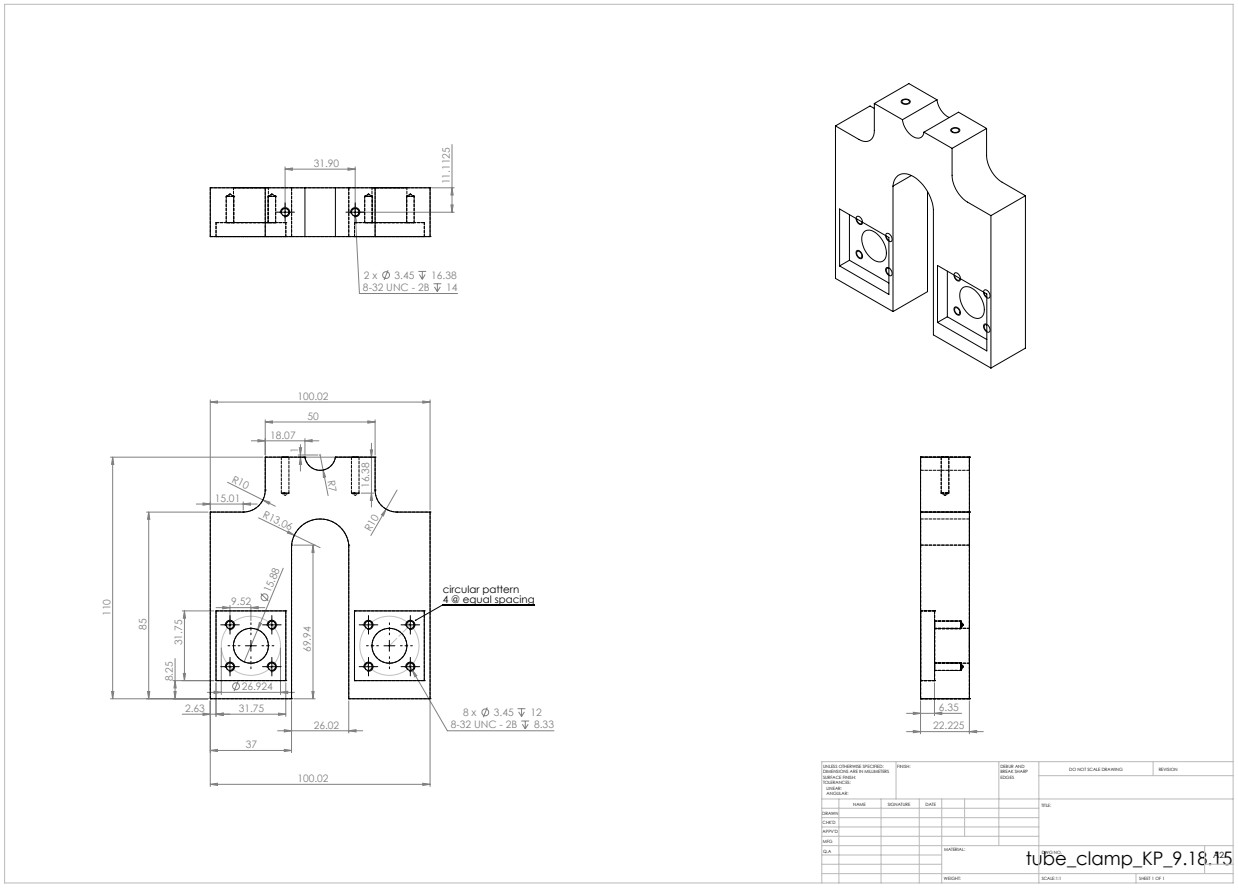

FIGURE A1. Drawing for tube furnace flange support that is guided by two linear rail systems.

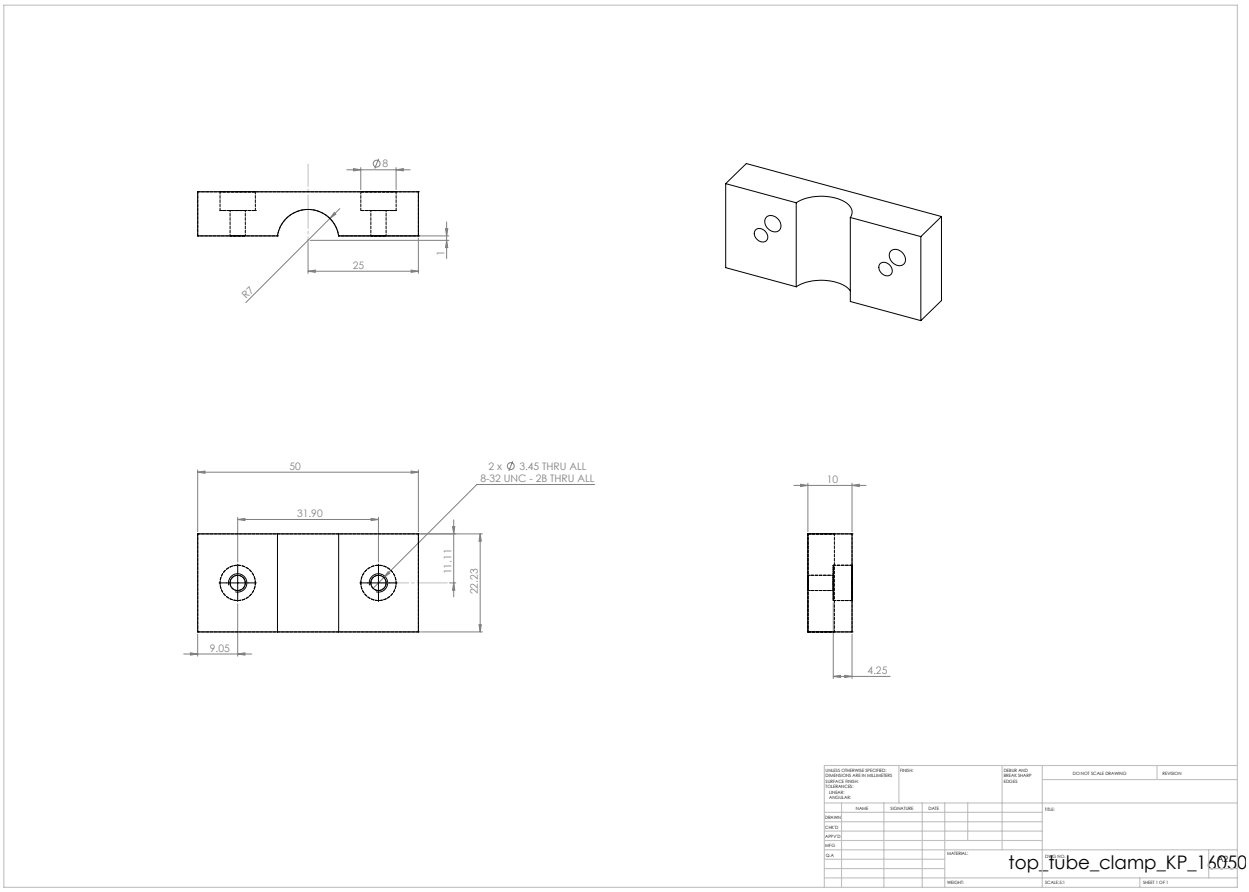

FIGURE A2. Drawing for flange support that attaches to part shown in Fig. A1.

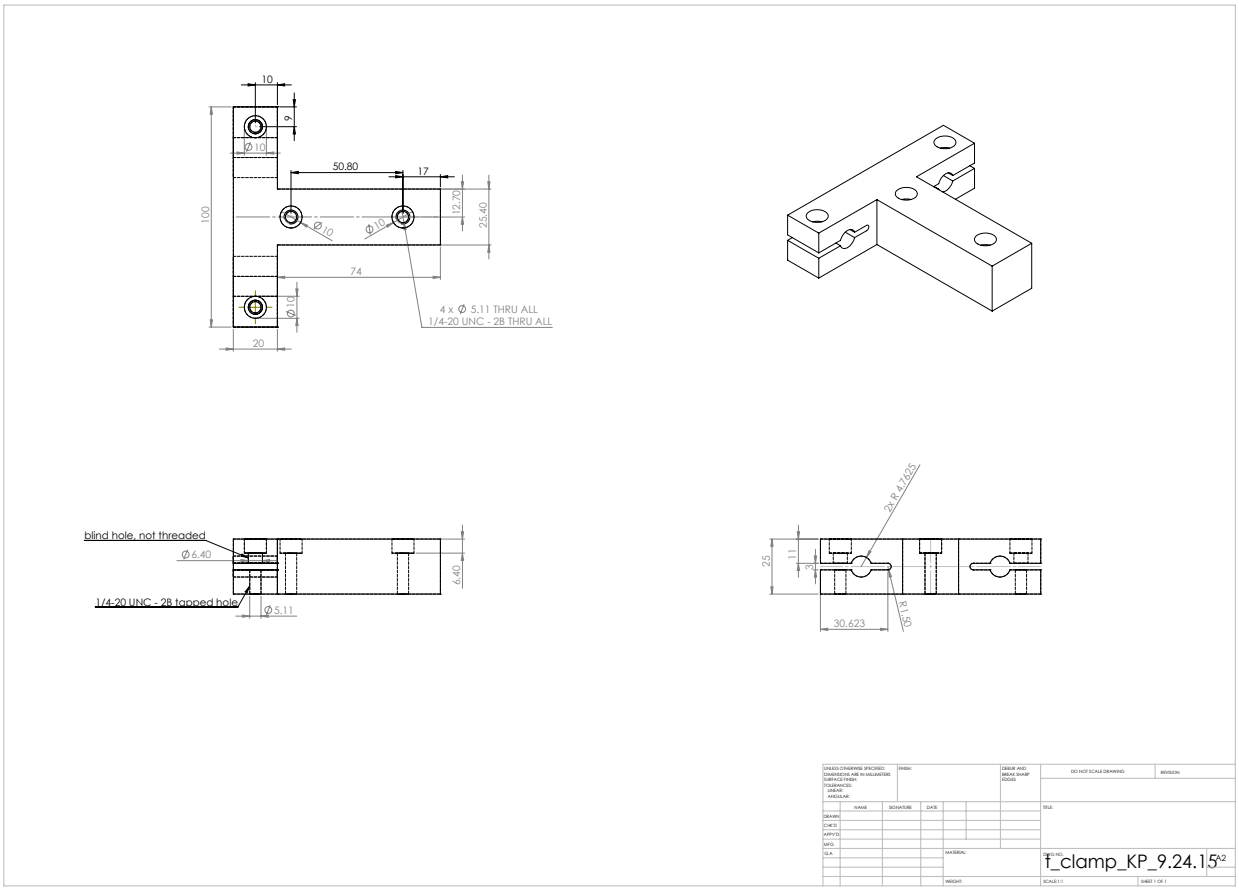

FIGURE A3. Drawing for t-clamp that holds the linear rails and connects to table stand.

APPENDIX B: X-ray Photoelectron Spectroscopy of BN Phase

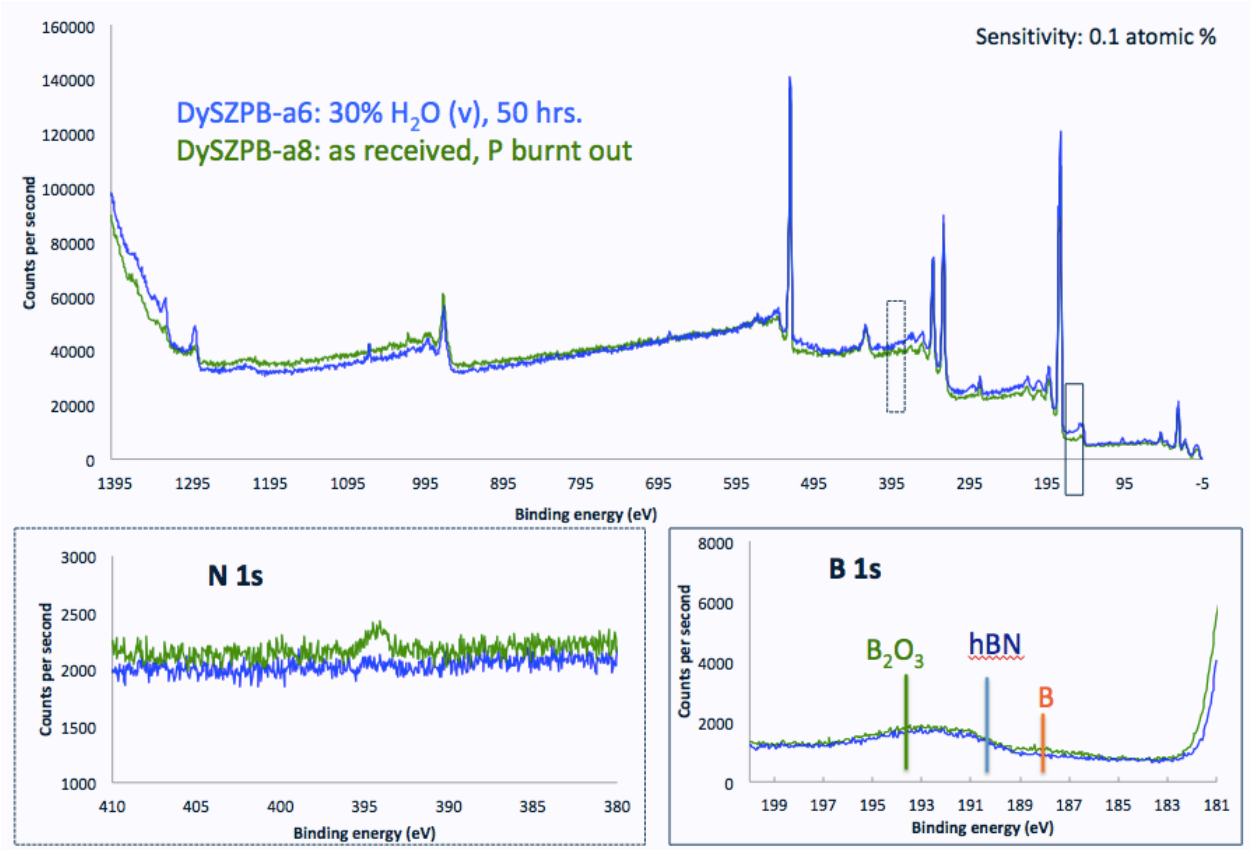

FIGURE B1. X-ray photoelectron spectroscopy maps for both the as received and exposed DySZPB coatings. The regions for N 1s and B 1s binding energies are blown up showing the complication of the analysis of hBN versus B_2O_3 due to the presence of those peaks being close with signal overlap complicating the deconvulution of the hBN versus B_2O_3 peak signals.

APPENDIX C: Preliminary Work on the Effect of Toughness

1. 

2. 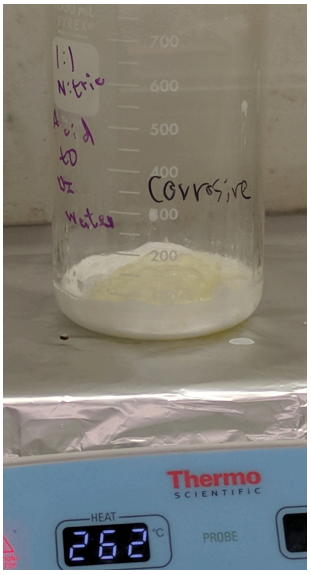

3. 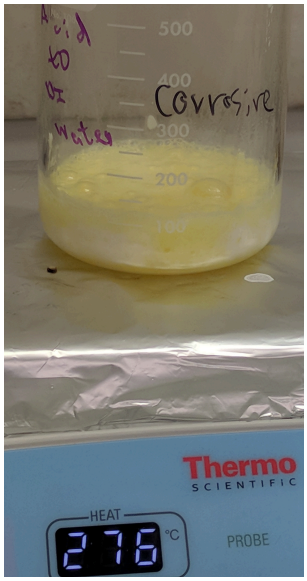

4. 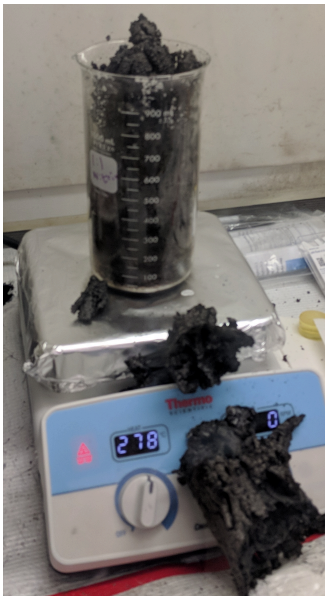

5. 

6. 

FIGURE C1. Images showing the glycine nitrate process used to synthesize DySZ powders. A solution of dysprosia, zirconium nitrate, and glycine in diluted nitric acid was heated to 80˚C to form a viscous gel (image 1). The gel was then heated to above 250˚C to start the autoignition process (images 2 and 3). Powders were then formed, ground with a mortar and pestle, and calcined at 900˚C to remove any residual carbon (images 4, 5, and 6). The structure was confirmed by XRD.

FIGURE C2. Image of the assembly of powders into the SPS graphite die; graphite foil was used between the die and powders. 4YSZ powders were sintered in a Fuji SPS 825-S with parameters of 100˚C/minute heating rate, 65 MPa pressure, 1600˚C sintering temperature, 10 minute hold time, and 200-300˚C cooling rate.

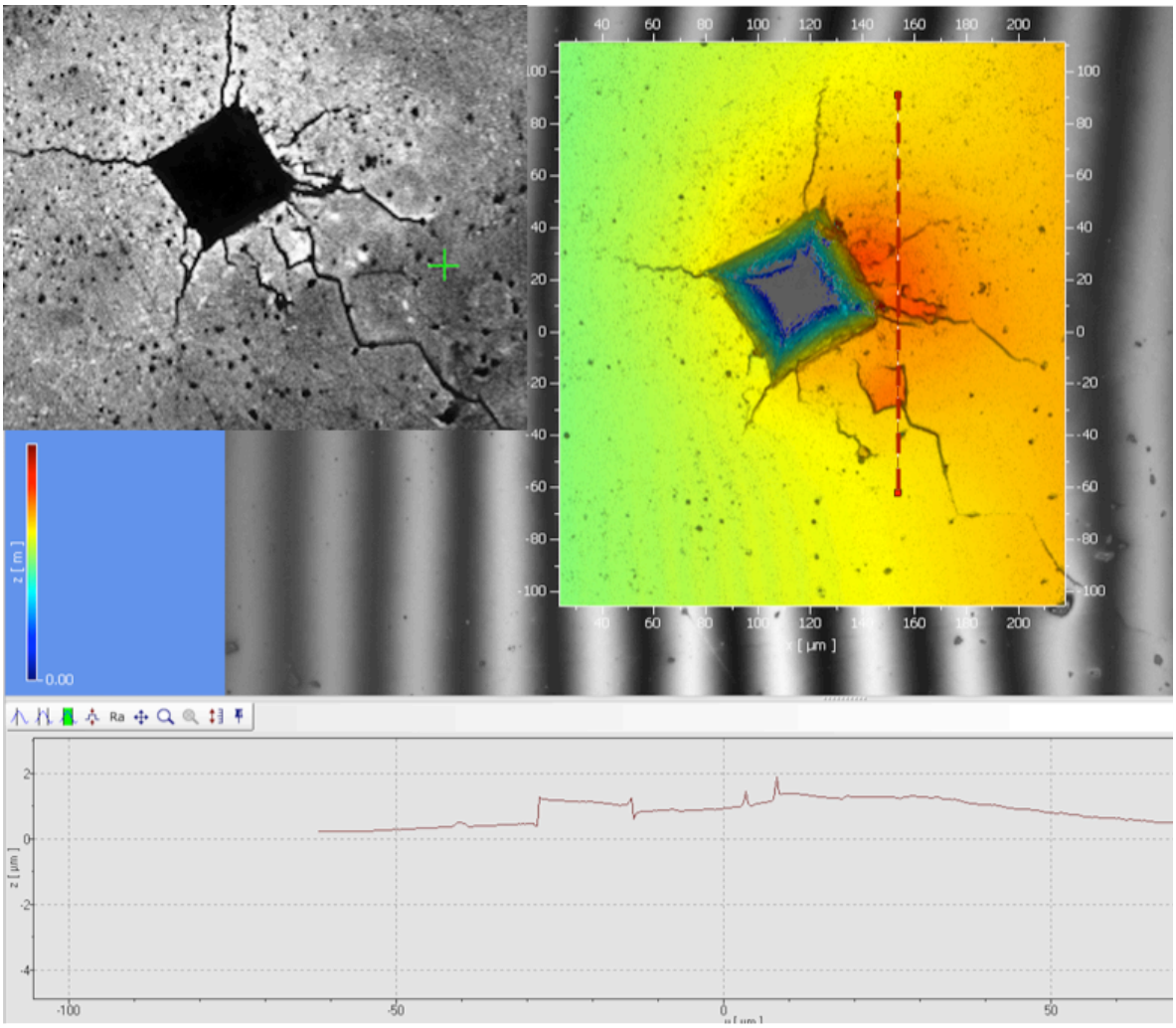

FIGURE C3. Optical vibrometer image and topography map of a Vicker's indent on the 4YSZ SPS pellet. The measurement of the surface topography is shown in the bottom line scan indicating a distortion around the cracked region on the right indentation crack.

APPENDIX D: Future Lab Test Preliminary Designs

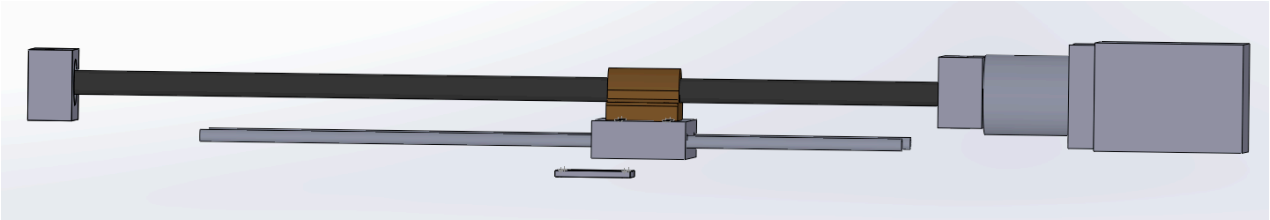

FIGURE D1. Schematic showing potential setup for future instrumentation. The sample holder plate will be fixed and the tangential load can be applied across the sample surface using a motor driven on an acme screw that is stabilized by linear rails.

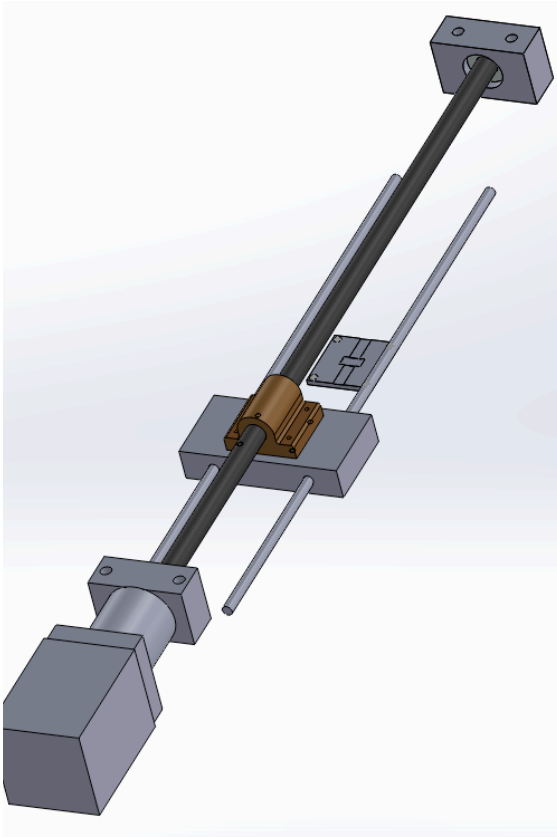

FIGURE D2. Illustration showing alternative view of Fig. B1 with better view of sample holder plate.